

**THE UNIVERSITY OF CALGARY**

**Acquisition, Processing, and Interpretation  
of P-P and P-S 3-D Seismic Data**

by

**Glenn Allen Larson**

**A THESIS**

**SUBMITTED TO THE FACULTY OF GRADUATE STUDIES  
IN PARTIAL FULFILMENT OF THE REQUIREMENTS FOR THE  
DEGREE OF MASTER OF SCIENCE**

**DEPARTMENT OF GEOLOGY AND GEOPHYSICS**

**CALGARY, ALBERTA**

**December, 1996**

**© Glenn Allen Larson 1996**



**National Library  
of Canada**

**Acquisitions and  
Bibliographic Services**

**395 Wellington Street  
Ottawa ON K1A 0N4  
Canada**

**Bibliothèque nationale  
du Canada**

**Acquisitions et  
services bibliographiques**

**395, rue Wellington  
Ottawa ON K1A 0N4  
Canada**

*Your file Votre référence*

*Our file Notre référence*

**The author has granted a non-exclusive licence allowing the National Library of Canada to reproduce, loan, distribute or sell copies of his/her thesis by any means and in any form or format, making this thesis available to interested persons.**

**The author retains ownership of the copyright in his/her thesis. Neither the thesis nor substantial extracts from it may be printed or otherwise reproduced with the author's permission.**

**L'auteur a accordé une licence non exclusive permettant à la Bibliothèque nationale du Canada de reproduire, prêter, distribuer ou vendre des copies de sa thèse de quelque manière et sous quelque forme que ce soit pour mettre des exemplaires de cette thèse à la disposition des personnes intéressées.**

**L'auteur conserve la propriété du droit d'auteur qui protège sa thèse. Ni la thèse ni des extraits substantiels de celle-ci ne doivent être imprimés ou autrement reproduits sans son autorisation.**

0-612-20834-6

## **Abstract**

**Three-dimensional (3-D) seismic images have become an essential tool in seismic exploration. The interpretation tools and practices for conventional (acoustic) 3-D developed over the past 20 years have become established techniques in oil and gas exploration.**

**Converted-wave 3-D (3C-3D) seismic images can accompany a conventional acoustic survey and provide a powerful adjunct toward a more complete interpretation. Proper design schemes are considered here to account for the nature of 3-D converted-wave recording without compromising either the acoustic or elastic data.**

**3-D converted-wave surveys are acquired over a carbonate and clastic numerical model. Extra elastic-wave information (e.g.  $V_p/V_s$  values, P-P and P-S amplitude maps) allows further characterization of the clastic and carbonate anomaly.**

**A 3C-3D seismic survey acquired in central Alberta is analyzed. The inclusion of the P-S data allow the construction of  $V_p/V_s$  and delay-time maps for the slow and fast shear-wave polarization.  $V_p/V_s$  mapping displays an anomaly in the Viking interval which suggests a higher percentage of sand.**

## **Acknowledgments**

I have been fortunate to have completed this work with many fine colleagues and friends at the Department of Geology and Geophysics at the University of Calgary. It is the knowledge and friendships that I have gained during my tenure here that will always remain with me.

I would like to thank Dr. Rob Stewart, my advisor, for his continued support throughout my time here. He was the person who raised my interest in multicomponent seismology and provided me with the will to finish this thesis. Dr. Don Lawton was gracious in allowing use of his CCP field design program. I had many useful and productive conversations with Shaowu Wang regarding the converted-wave processing.

This interpretation could not have occurred without the processing expertise of Dr. Peter Cary of Pulsonic Geophysical Ltd. Eric Howell of Norcen provided the geological map of Figure 5.1. The software donations of SeisWorks 3-D and ProMax 3-D from Landmark Graphics Corporation are acknowledged. I gratefully appreciate the continued support of the CREWES Project Sponsors.

Finally, I am indebted to the CREWES Project Staff, Henry Bland, Darren Foltinek, Louise Forgues, Eric Gallant, Mark Lane, and Sue Miller. This thesis could not have been completed in anywhere near a timely manner without their support.

## Table of Contents

Abstract .....	iii
Acknowledgments .....	iv
Table of Contents .....	v
List of Tables .....	viii
List of Figures .....	ix
<b>Chapter 1 - Introduction .....</b>	<b>1</b>
1.1 Background .....	1
1.2 Thesis objectives .....	4
1.3 Data set used .....	4
1.3.1 Numerical model .....	4
1.3.2 Field data .....	4
1.4 Hardware and software used .....	5
<b>Chapter 2 - Processing of 3-D converted-wave seismic data .....</b>	<b>6</b>
2.1 Introduction .....	6
2.2 Rotation into transverse and radial components .....	6
2.3 Rotation into S1 and S2 polarizations .....	8
2.4 Converted-wave NMO correction .....	9
2.5 Common-conversion-point gathering .....	11
2.6 Receiver statics .....	14
2.7 3-D P-S DMO .....	17
2.8 3-D P-S Processing Flow .....	17
2.9 Chapter Summary .....	19
<b>Chapter 3 - Acquisition design of 3-D converted-wave surveys .....</b>	<b>20</b>
3.1 Introduction .....	20
3.2 3-D CMP design strategies .....	21
3.2.1 Design calculations.....	21
3.3 Common 3-D CMP designs .....	26
3.3.1 3-D marine surveys .....	26
3.3.2 3-D land surveys .....	27
3.3.3.1 Straight line .....	27

3.3.3.2 Swath .....	28
3.3.3.3 Brick pattern .....	29
3.3.3.4 Button pattern .....	30
3.3.3.5 Zigzag.....	31
3.3.3.6 Bin fractionization.....	32
3.4 3-D P-S acquisition issues.....	33
3.4.1 CCP fold patterns .....	33
3.4.2 Optimal bin size for CCP 3-D recording .....	35
3.4.3 Channel capability .....	37
3.4.4 Field procedures .....	37
3.4.5 P-S Fresnel zones .....	38
3.4.6 Marine 3-D CCP surveys .....	38
3.5 Design integration .....	39
3.6 3C-3D design example .....	40
3.7 Chapter summary .....	44
<b>Chapter 4 - Interpretation of 3-D converted-wave data: Numerical model .....</b>	<b>45</b>
4.1 Model description .....	45
4.1.1 Clastic model .....	45
4.1.2 Carbonate model .....	48
4.2 Data acquisition .....	49
4.2.1 Acquisition design .....	50
4.2.2 Steps in acquisition .....	54
4.2.2.1 Raytracing .....	55
4.2.2.2 Reformatting and convolution .....	56
4.3 Processing .....	57
4.3.1 Pre-processing .....	57
4.3.2 3-D P-P processing .....	58
4.3.3 3-D P-S processing .....	59
4.4 Interpretation .....	62
4.4.1 Clastic model interpretation .....	63
4.2.2 Carbonate model interpretation .....	67
4.5 Tuning effects upon Vp/Vs ratio calculations.....	71
4.6 Chapter summary .....	76

<b>Chapter 5 - Analysis of 3C-3D field data</b> .....	77
5.1 Introduction .....	77
5.2 Geological background .....	79
5.3 Acquisition and processing .....	81
5.4 Interpretation techniques .....	88
5.5 Results .....	96
5.6 3C-3D Interpretation flow .....	104
5.7 Chapter Summary.....	106
<b>Chapter 6 - Discussion and Conclusions</b> .....	107
<b>References</b> .....	110

## **List of Tables**

<b>TABLE 3.1. Final design parameters for example 3C-3D survey. ....</b>	<b>44</b>
<b>TABLE 4.1. Clastic model layer velocities and thicknesses. ....</b>	<b>47</b>
<b>TABLE 4.2. Carbonate model layer velocities and thicknesses. ....</b>	<b>49</b>
<b>TABLE 4.3. 3C-3D Recording parameters: Numerical mode. ....</b>	<b>51</b>
<b>TABLE 4.4. <math>V_p/V_s</math>, <math>I_p</math>, and <math>I_s</math> values for the Viking to Mannville interval for decreasing values of the dominant frequency. ....</b>	<b>74</b>
<b>TABLE 4.5. <math>V_p/V_s</math>, <math>I_p</math>, and <math>I_s</math> values for the Viking to Mannville interval for decreasing P-S dominant frequency. P-P dominant frequency = 40 Hz. ....</b>	<b>75</b>
<b>TABLE 5.1. Survey design parameters: Joffre survey. ....</b>	<b>82</b>

## List of Figures

FIG. 2.1.	Schematic plan view of a 2-D-3-C survey. The horizontal channels of the 3-component geophones are aligned so the H1 channel is parallel to the direction of the survey acquisition (the x-axis) and H2 is perpendicular to the survey direction (the y - axis). The H1 and H2 are therefore parallel and perpendicular, respectively, to the radial and transverse component of the incident shear wave. This field standard follows the convention put forth by Stewart and Lawton (1994). .....	7
FIG. 2.2.	Coordinate transformations required for data recorded in the (X,I) coordinate frame (the H1 and H2 channels of the 3-C geophone) to the (R,T) coordinate frame (the radial and transverse components) for each source-receiver pair in a 3-D survey. $\beta$ usually remains constant throughout the survey. A positive rotation is defined as clockwise about the origin. (Modified from Lane and Lawton, 1993). .....	8
FIG. 2.3.	Polarization angles with depth .....	9
FIG. 2.4.	P-S travelttime estimation error for a raytraced isotropic single-layer model. ....	11
FIG. 2.5.	Schematic diagram of the lateral shift of the CCP points with depth. (Modified from Schaffer, 1992). .....	12
FIG. 2.6.	Asymptotic CCP vs. exact CCP position error. ....	13
FIG. 2.7.	Schematic diagram of fast 3-D CCP binning. For each bin (numbered 1 to 6), the samples within a bin are grouped together and assigned that bin number. (Modified from Wang et al., 1994a). .....	14
FIG. 2.8.	Comparison of P-wave and S-wave statics for a 3C-2D line in Cold Lake, Alberta. ..	15
FIG. 2.9.	Example reciever stacks a) before, b) after alignment of the high amplitude event at 1.2 seconds, and c) the final receiver gather after static correction. ....	16
FIG. 2.10.	A 3-D P-S processing flow. Three products result from the processing. (Modified from Cary, 1994b). .....	18
FIG. 3.1.	Steps in 3-D P-P survey design. The design is for orthogonal source and receiver line, which is most the most common geometry for land 3-D surveys. (Modified from Galbraith, 1994; and Stone, 1994). .....	22
FIG. 3.2.	The largest minimum offset (Xmin) is defined as the hypotenuse between the furthest shot and receiver pair within the rectangle formed by adjacent shot and receiver lines. It is common for the shot and receiver lines to cross between the source and receiver stations. ....	24

FIG. 3.3. Receiver template consisting of 3 receiver lines and 8 groups per line. The maximum offset ( $X_{max}$ ), as defined by the hypotenuse of the receiver template, should exceed the maximum depth of target. The template can also be extended in one dimension to allow for the migration aperture. ....	26
FIG. 3.4. Straight line 3-D survey geometry. Dark and grey solid squares outline successive live receiver patches for the shots (circled). ....	28
FIG. 3.5. Swath 3-D survey geometry. ....	29
FIG. 3.6. The Brick pattern. ....	30
FIG. 3.7. The Button pattern. The receivers are grouped into buttons with the shots fired outside the patch template. ....	31
FIG. 3.8. Zigzag pattern. ....	32
FIG. 3.9. Bin fractionation. ....	33
FIG. 3.10. Survey geometry for the Joffre survey. The shot lines lie at a 45 degree angle to the receiver lines. This is a variation of the zigzag survey. ....	34
FIG. 3.11. CMP fold distribution for the original survey at Joffre. Offset ranges used for the calculation : 0-2000m. ....	35
FIG. 3.12. CCP Optimized Fold Map. ....	36
FIG. 3.13. Amended 3-D design flow for the integration of CMP and CCP design parameters. ....	42
FIG. 3.14. Design flow for the 3C-3D survey example. ....	43
FIG. 4.1. Plan view of clastic model. The thicknesses of the bodies range, from northwest to southeast: 15m, 25m, and 20m, respectively. The A-A' cross-section marker refers to Figure 4.2. ....	46
FIG. 4.2. Cross-section of the clastic model. ....	47
FIG. 4.3. Plan view of the carbonate model. The B-B' cross-section refers to Figure 4.4. ....	48
FIG. 4.4. Cross-section of carbonate model.....	49
FIG. 4.5. P-P model fold map. Offset range: 0 to 2600m. ....	52
FIG. 4.6. P-S numerical fold map. Offset range: 0 to 2600m. Bin size = 50m x 50m. ....	53
FIG. 4.7. P-S Fold map for a Shot Line spacing of 600m (even integer of the receiver spacing). Note the fold gaps with this increment of line spacing. ....	54
FIG. 4.8. Acquisition steps of a 3-D numerical model for Sierra ratyracing software. ....	55
FIG. 4.9. Vector magnitude of the incoming shear-wave ray path upon the Sierra system. This amplitude is recorded and convolved with the wavelet.....	56
FIG. 4.10. 3-D P-P processing flow. ....	58
FIG. 4.11. Shot record 47 of the P-P clastic model. ....	59
FIG. 4.12. 3-D P-S processing flow. ....	60

FIG. 4.13. Record of shot 47 of 3-D P-S numerical model survey. ....	60
FIG. 4.14. Inline 54 of the clastic model: P-P migrated volume. ....	63
FIG. 4.15. Inline 54 of the clastic model: P-S migrated volume ....	64
FIG. 4.16. Vp/Vs map: Clastic model. Base of Fish Scales to Mannville interval. ....	65
FIG. 4.17. Viking shear amplitude map: Clastic model. ....	65
FIG. 4.18. Mannville shear amplitude map: Clastic model. ....	66
FIG. 4.19. Viking P-P amplitude map: Clastic model. ....	66
FIG. 4.20. Inline 44 of the carbonate model: P-P migrated volume. ....	68
FIG. 4.21. Inline 44 of the carbonate model: P-S migrated volume. ....	68
FIG. 4.22. P-P carbonate amplitude map: Carbonate model. ....	69
FIG. 4.23. P-S carbonate amplitude map: Carbonate model. ....	69
FIG. 4.24. P-S Ireton amplitude map: Carbonate model. ....	70
FIG. 4.25. Vp/Vs (Wabamun to Ireton isochron) map. Carbonate model. ....	70
FIG. 4.26. 2-D P-S migrated section of the clastic model. Dominant frequency = 50 Hz. .....	72
FIG. 4.27. 2-D P-P migrated section of the clastic model. Dominant frequency = 60 Hz. ....	73
FIG. 4.28. Vp/Vs versus P-P and P-S section dominant frequency. Clastic numerical model. ..	74
FIG. 4.29. Vp/Vs versus P-S frequency. P-P frequency = 40 Hz. Clastic numerical model. ....	75
FIG. 5.1. Vp/Vs map centred about the Glauconitic formation: Blackfoot 3C-3D .....	78
FIG. 5.2. Location of the Joffre 3C-3D survey surperimposed upon Leduc and Nisku formation outlines. The Joffre Viking field lies 2 miles southwest of the survey. ....	80
FIG. 5.3. Survey grid of the Joffre multicomponent survey. The source lines run at a 45 degree angle to the north-south receiver lines. Units are in metres. ....	83
FIG. 5.4. CMP fold of the Joffre 3-D multicomponent survey. From Lawton, 1993. ....	84
FIG. 5.5. CCP optimized fold of the Joffre 3-D multicomponent survey. Note the fold gaps and the high periodicity of the fold in the east-west direction. From Lawton, 1993. ....	85
FIG. 5.6. 3-D P-P Processing Flow. From Cary, 1994b. ....	86
FIG. 5.7. 3-D P-S Processing Flow. From Cary, 1994. ....	87
FIG. 5.8. Geometry of the 3-D data. There are 107 crosslines (east-west direction) and 141 inlines (north-south direction). ....	88
FIG. 5.9. Event correlation of Crossline 67 between P-P and P-S1. The time scale of the P-P section has been expanded by 1.5 times to match the scale of the P-S section. ....	89
FIG. 5.10. Tie between Crossline 70 (S1) and Inline 40 (S2). ....	91
FIG. 5.11. S1 amplitude map of the Second White Speckled Shale. The striped pattern follows the survey geometry. ....	92
FIG. 5.12. Time slices of P-P (a) and P-S (b) at times 1280 and 1820ms, respectively. ....	94

**FIG. 5.13. Delay time mistie calculation for horizons A and B between the S1 and S2 volumes. For a 3-D volume, the misties for each horizon are mapped throughout the entire survey. .... 95**

**FIG. 5.14. Time delay maps between the S1 and S2 data volumes for the Colorado event 2 (a) and the Colorado event 1 (b). .... 97**

**FIG. 5.15. Time delay map between the S1 and S2 data volumes for the Second White Speckled Shale (a) and the peak one cycle below it (b). .... 98**

**FIG. 5.16. Time delay map between the S1 and S2 data volumes for the Base of Fish Scales (a) and the Viking (b). .... 99**

**FIG. 5.17. Time delay map between the S1 and S2 data volumes for the Mannville Coal (a) and the Wabamun (b). .... 100**

**FIG. 5.18. Time delay maps between the S1 and S2 data volumes for the Nisku (a) and the Leduc (b). .... 101**

**FIG. 5.19.  $V_p/V_{s1}$  ratio (x100) maps of the Viking calculated between two intervals: a) The Base of Fish Scales to the Mannville and b) Colorado event 1 and the Mannville. .. 102**

**FIG. 5.20.  $V_p/V_{s2}$  ratio (x100) maps of the Viking calculated between two intervals: a) The Base of Fish Scales to the Mannville and b) Colorado event 1 and the Mannville. .. 103**

**FIG. 5.21. 3C-3D Interpretation flow..... 105**

## Chapter 1: Introduction

### 1.1 Background

Three-dimensional (3-D) seismic acquisition has become an essential tool in seismic exploration as a way to optimize investment and minimize risk (Buchanan, 1992). The 3-D seismic survey is a fairly recent development in seismic history. An early 3-D survey was conducted by Exxon in the late 1960's (Robertson, 1992). French (1974) conducted physical models which displayed the imaging prowess of 3-D versus 2-D acquisition. 3-D surveys over productive reservoirs began in New Mexico in 1973 by a six company consortium, while marine 3-D surveys began in the Gulf of Mexico in 1975. The first public 3-D seismic survey in Canada was acquired in 1981. Since then, the number of 3-D surveys acquired worldwide has increased rapidly each year (Oosterbaan, 1990). Today they are an established practice in exploration and development.

Shear-wave acquisition also has had a long history (Tatham and Stewart, 1993), although its usefulness has not been as quickly exploited as conventional P-wave acquisition. Tatham and McCormack (1991) have established 2-D interpretational techniques for multicomponent seismic data. A key interpretative tool with multicomponent seismic data is the calculation of the ratio between the velocity of the P-wave versus the velocity of the S-wave (the  $V_p/V_s$  ratio). The conventional and shear-wave sections both generally respond to structural changes in the subsurface (Tatham and McCormack, 1991). Time interval isochron differences between the stacked sections of the P-P and P-S data can sometimes be related to changes in the bulk properties of the rocks within the interval. If the bulk property variables can be constrained, then robust, but perhaps low resolution lithologic, porosity, or fracture density inferences are possible. Sensitivities of  $V_p/V_s$  to gas saturation, lithology, porosity, and fracturing within a time interval can be exploited.

For converted waves,  $V_p/V_s$  can be calculated from stacked data sets of P-P and P-S using the following equation (Harrison, 1992):

$$\frac{V_p}{V_s} = \frac{2 I_s}{I_p} - 1, \quad (1.1)$$

where  $I_s$  = time interval between two P-S reflections,

$I_p$  = time interval between two P-P reflections the same reflectors.

The calculation of  $V_p/V_s$  combines time structural information from acoustic and elastic data. Unlike exclusive P-P surveys, multicomponent seismic allows comparisons between the two datasets that provide an independent assessment of the earth's subsurface, providing additional information not otherwise available directly.

Converted-wave surveys in two dimensions have been acquired to infer lithology using  $V_p/V_s$  values (Garrota et al., 1985; Miller et al., 1994). Ensley (1985) uses comparative amplitude analysis between acoustic and elastic-wave seismic data to identify gas-bearing clastic reservoirs in the Myrnam Field, Alberta. Shear-waves have been used in anisotropic studies and fracture detection (Yardley et al., 1991) by comparing the post-stack amplitudes between the fast shear-wave polarization (S1) and the slow shear-wave polarization (S2). Mueller (1991) has inferred areas of faulting within the Austin Chalk reservoir in Texas from dimming of the S2 amplitude on 2-D multicomponent lines. Al-Bastaki et al. (1994) use a pure shear (S-S) 3-D multicomponent survey as part of an integrated characterization of a Nisku reservoir in central Alberta, Canada. Yang et al. (1996) have analyzed a 3C-3D dataset in the Blackfoot area of southern Alberta to infer the presence of a channel in the Glauconitic Formation of the Lower Cretaceous.

An extension of converted-wave surveys is to combine the interpretive techniques of 2-D converted-waves with 3-D P-S information to construct multicomponent 3-D data sets. This combination will provide a more detailed description of the rock volume. Once

each volume is interpreted, equation (1.1) can be used to easily calculate  $V_p/V_s$  for a series of interpreted horizons throughout the survey area. The power of 3-D surveys lies in the ability of  $V_p/V_s$  to be *mapped* over a series of intervals throughout the sedimentary column. The orientation of the fast shear-wave polarization (S1) and the slow shear-wave polarization (S2) can be determined in processing using techniques developed by Garotta and Granger (1988) and Harrison (1992). The two shear polarizations can be processed separately, tripling the amount of interpretable data; each providing an independent image of the subsurface. The variations of the S1 and S2 isochrons between horizons can also be mapped over intervals throughout the sedimentary column, providing inferences on the relative stress patterns in the area, extending into 3-D the 2-D techniques of Mueller (1991) and Yardley (1991).

The benefit of recording 3-C data is acquiring three times as much seismic data at about a 40% higher cost than a conventional (P-P) survey. Only a P-wave source is required with three-component geophones. A 3-D survey using pure S-wave sources requires two orthogonal source polarizations for the detection of azimuthal anisotropy. Shear-sources are expensive, and the survey must be acquired three times to record all three components. These factors impair its cost-effectiveness. Also, shear vibrators, a popular shear-wave source, have limited access in certain environments such as muskeg, rough terrain and environmentally sensitive areas, and hence are not used in these areas. Pure shear-wave surveys are lacking in the marine case. Garotta et al. (1990) have found that the converted-wave 3-D data is faster and easier to acquire, and its data quality is comparable to pure shear 3-D surveys.

Interpretive techniques for acoustic 3-D surveys have been well-established (Brown, 1991). Multicomponent 3-D surveys provide an additional challenge for the interpreter: There are more than three times as many interpretable products. Based upon 2-D multicomponent interpretive techniques, there are also interpretive products to be

generated from the *comparison* of the acoustic and elastic data. The tripling of the data volumes will increase the amount of data to be assimilated by the interpreter. A more detailed description of the rock volume will result which promises to mitigate exploration risk and provide a more detailed and integrated interpretation.

## **1.2 Thesis objectives**

This thesis concentrates upon the establishment of interpretational methods for 3-D converted-wave data by extending conventional 2-D multicomponent interpretational techniques and 3-D P-wave methods using existing workstation technology. Aspects of survey design for converted-wave 3-D are described, and the interpretation flow is presented. This thesis attempts to provide insights into the power and usefulness of jointly interpreting a shear volume with an existing compressional volume to provide a more detailed interpretation.

## **1.3 Data sets used**

### **1.3.1 Numerical model**

Two numerical models are constructed with the Sierra raytracing software package. The models consist of a shallow sand model and a deeper reef to basin transition, respectively. The layer velocities and depths follow the geology of the central Alberta region of the Western Canadian Sedimentary Basin.

### **1.3.2 Field Data**

In April of 1992, a 9C-3D survey was acquired in central Alberta, Canada. The data were acquired by Solid State Geophysical Ltd. for the Colorado School of Mines.

## **1.4 Hardware and software**

The numerical models are constructed and acquired using Sierra's MIMIC, QUIKSHOT and SLIPR packages. Data processing was completed using the ProMax3D package, an interactive processing software package from Advance Geophysical Corporation, a division of Landmark Graphics Corporation. The software ran upon an Open Storage Solutions' Sparc10 clone. The 3D interpretation was completed using SeisWorks3D which was provided to the CREWES Project by Landmark Graphics Corporation. The software ran upon a Sun Microsystems Sparc2. All figures presented in this thesis were created on the Canvas® graphics software package using Macintosh computers. All the interpretation figures were rendered directly from the screen using XGRAB® and sent to Canvas and Adobe Photoshop® for further image processing. Acquisition design was completed with Design3C - a program developed by Don Lawton and Darren Foltinek. The text was processed using Microsoft Word® and Expressionist® using a Macintosh computer.

## **Chapter 2: Processing 3-D converted-wave seismic data**

### **2.1 Introduction**

Many researchers have developed 2-D algorithms and procedures for handling converted-wave seismic data. Fromme et al. (1985) develop the concept of asymptotic converted-wave binning, a first order approximation to the depth-variant movement of the conversion point. Eaton et al. (1990) describe a sample-by-sample translation for depth-variant P-S binning. Slotboom (1990) develops a higher order NMO correction for P-S data with high offset-to-depth ratios. Harrison (1992) develops processes for 2-D anisotropic rotations, migration, and DMO. This chapter reviews and extends the key 2-D converted-wave concepts previously developed and proposes a 3-D converted-wave processing flow. Some of the processes introduced here are used for the numerical and field data sets in later chapters.

### **2.2 Rotation into transverse and radial components**

For a 2-D, 3-component (3-C) line, the H1 and H2 channels of the 3-component geophone are usually placed parallel (radial component) and perpendicular (transverse component) to the direction of acquisition, respectively (Figure 2.1). This is consistent with the recording convention proposed by Stewart and Lawton (1994).

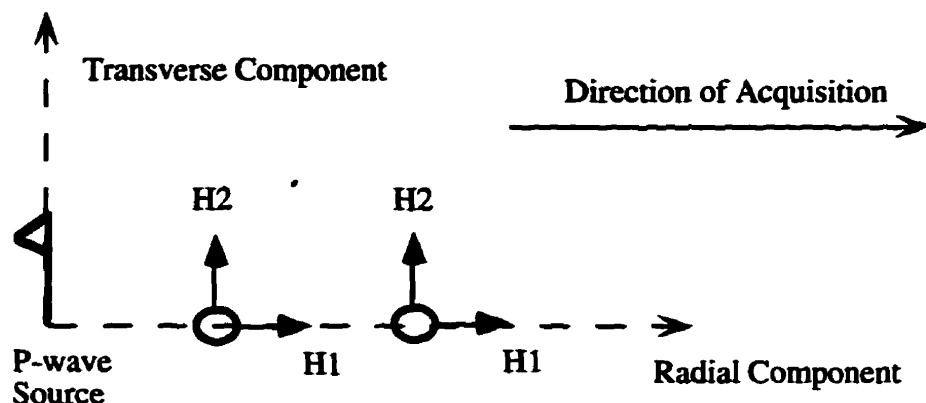


Figure 2.1: Schematic plan view of a 2-D-3-C survey. The horizontal channels of the 3-component geophones are aligned so the H1 channel is parallel to the direction of the survey acquisition (the x-axis) and H2 is perpendicular to the survey direction (the y-axis). The H1 and H2 are therefore parallel and perpendicular, respectively, to the radial and transverse component of the incident shear wave. This field standard follows the convention proposed by Stewart and Lawton (1994).

For a 3-D geometry, the radial and transverse components are no longer in the same orientation as the H1 and H2 channels of the geophone. The H1 and H2 channels measure components of the shear waves over a range of source-receiver azimuths. To separate the data into radial and transverse components, a coordinate transformation in the form of a rotation must take place: The geophone coordinate frame are rotated into the radial-transverse coordinate frame (Figure 2.2). The rotation follows the convention proposed by Stewart and Lawton (1994). This rotation is in the same form as the tool rotation in 3-C VSP processing (DiSiena et al., 1984). Lane and Lawton (1993) and Lane (1994) develop an algorithm to accomplish this rotation.

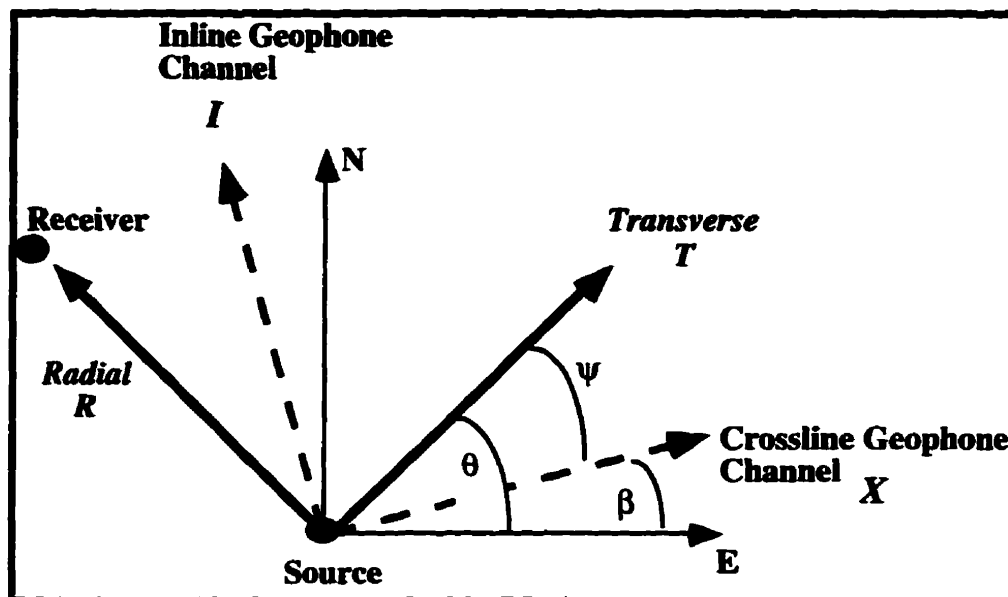


Figure 2.2: Coordinate transformations required for data recorded in the (X,I) coordinate frame (the H1 and H2 channels of the 3-C geophone) to the (R,T) coordinate frame (the radial and transverse components) for each source-receiver pair in a 3-D survey.  $\beta$  usually remains constant throughout the survey. A positive rotation is defined as clockwise about the origin. (Modified from Lane and Lawton, 1993).

### 2.3 Rotation into S1 and S2 polarizations

Surface seismic shear measurements indicate anisotropy at depth (Lynn and Thomsen, 1986; Mueller, 1992; Ata et al., 1994). Winterstein and Meadows (1991) have found instances where the shear polarization orientation varies with depth (Figure 2.3). To make these inferences with surface seismic measurements, the shear data must be rotated further into the S1 (fast) and S2 (slow) shear-wave polarizations.

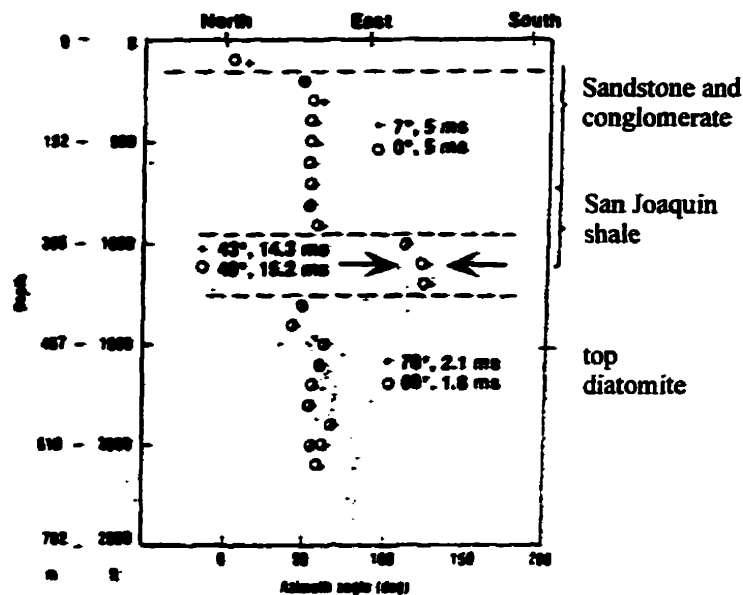


Figure 2.3: Polarization angles with depth for two independent layer stripping analyses from VSP data in California. Note the polarization angle shift within the middle layer at the base of the San Joaquin shale (modified from Winterstein and Meadows, 1991).

Alford (1986) develops a technique to complete the rotation into the S1 and S2 polarizations. Although used successfully for two orthogonal shear sources, the Alford rotation does not work for converted-wave (P-wave source) data. Harrison (1992) develops a rotation into the slow and fast shear wave polarization for converted-waves. Garrota and Granger (1988) develop the same rotation using limited azimuth stacks and radial-to-transverse energy ratios to determine the S1 and S2 polarization. Both methods can be applied to pre- and post-stack data. Cary (1994) extends their work into the 3-D realm. The result of the analysis gives two datasets that are processed separately.

## 2.4 Converted-wave NMO correction

Converted-wave data are non-hyperbolic at large offset-to-depth ratios. The conventional normal-moveout (NMO) correction, commonly a two term truncation of the series developed by Taner and Koehler (1969), has been used extensively for P-P and S-S

data. However, this correction will not properly flatten the P-S events at far offsets, if the offset-to-depth ratio is high. Slotboom (1990) develops a higher order approximation:

$$T_x = \frac{T_{0(ps)}}{2} + \sqrt{\frac{T_0^2}{2} + \frac{X^2}{2 \cdot V_{rms(ps)}^2}}, \quad (2.1)$$

where  $T_x$  = offset travel time

$T_{0(ps)}$  = zero offset converted-wave travel time

$X$  = source-receiver offset

$V_{rms(ps)}$  = converted-wave RMS velocity

This equation is successful in flattening the P-S reflections at a higher offset (Figure 2.4). It is also more efficient than other more computationally intensive equations such as those developed by Castle (1988) and Tessmer and Behle (1988).

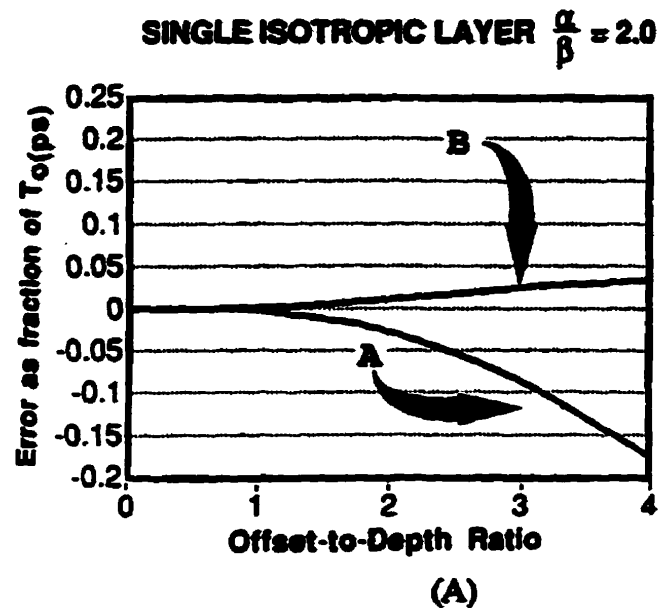


Figure 2.4: P-S travelttime estimation error for a raytraced isotropic single layer model. Curve A is the standard NMO equation. Curve B is the improved P-S formula (equation 2.1) (from Slotboom et al., 1990).

## 2.5 Common-conversion-point gathering

Common-conversion-point (CCP) gathering for binning and stacking is different than the common-mid-point (CMP) concept of P-P or S-S acquisition (Eaton and Stewart, 1989). Due to the asymmetry of the upgoing and downgoing portions of the ray path, the CCP trace gathering is different than the CMP gather. The CCP does not lie midway between the source and receiver for all depths, but lies closer to the receiver at shallow depths. This movement of the CCP has resulted in new binning concepts for 2-D and 3-D.

Fromm et al. (1985) develop a first-order asymptotic approximation to gather the traces. The asymptotic approximation gathers the traces at a position between the source and receiver (Figure 2.5) defined by the following equation:

$$X_{\text{ccp}} = \frac{X_{\text{S-R}}}{1 + \frac{V_s}{V_p}}, \quad (2.2)$$

where  $X_{\text{ccp}}$  = distance of CCP point relative to the source location,

$X_{\text{S-R}}$  = source-receiver offset,

$V_s$  = shear wave velocity,

$V_p$  = compressional wave velocity,

This approximation is adequate for depths greater than the maximum offset (Eaton et al., 1990) (Figure 2.6). It is also computationally efficient and has been extended to the 3-D case by Lane (1994).

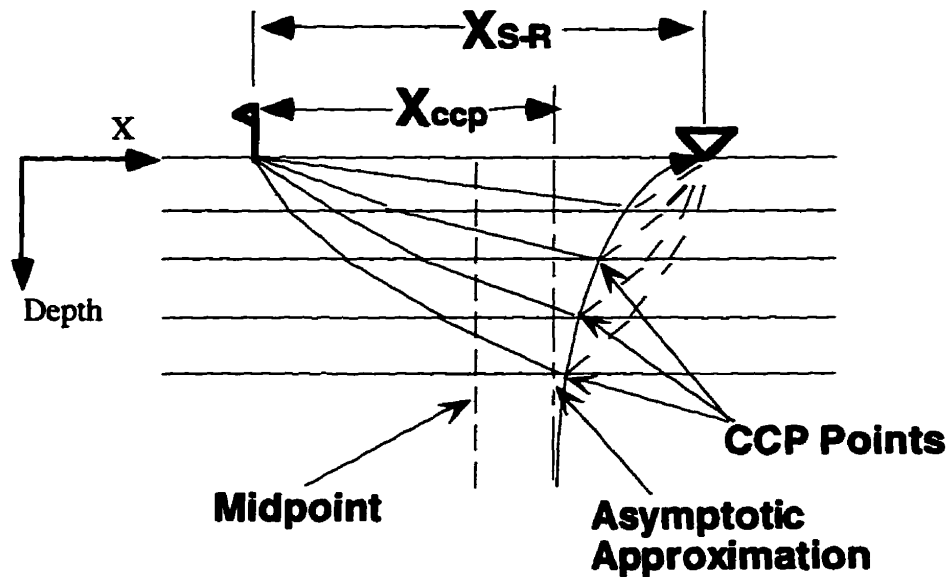


Figure 2.5: Schematic diagram of the lateral shift of the CCP points with depth. (Modified from Schaffer, 1992).

## Maximum CCP Error

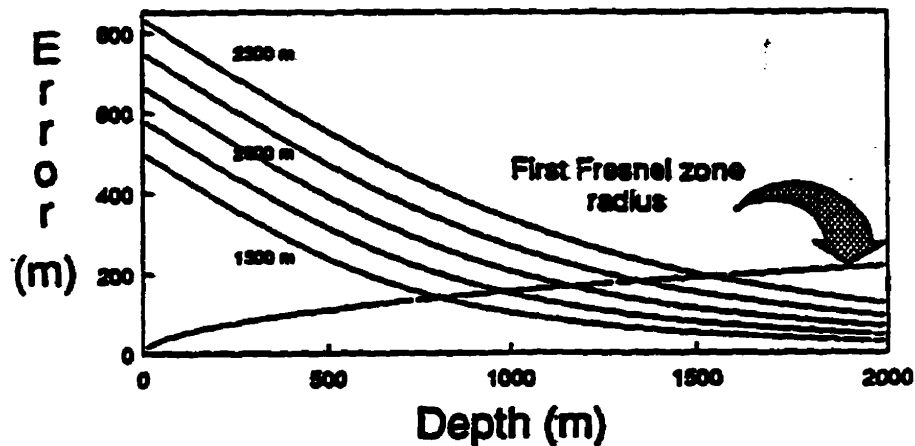


Figure 2.6: Asymptotic CCP vs. exact CCP position error for offsets between 1500 and 2500 metres. Note at 1500m offset, the CCP error for 1500m offsets is small. The first Fresnel zone radius for P-S reflections is also shown (from Eaton and Stewart, 1989).

A more complicated but accurate method uses depth-variant binning. Tessmer and Behle (1988) develop a depth-variant technique for a horizontally layered medium, but it is computationally intensive. Eaton et al. (1990) propose a simpler sample-by-sample mapping of the depth points for 2-D data. To alleviate the computational intensity of depth-conversion mapping, Wang et al. (1994a) propose a fast 3-D P-S depth-variant CCP binning algorithm. Their technique groups individual samples together in larger blocks based upon the bin size and mapping them on a less-refined scale rather than the more computationally intensive sample-by-sample basis (Figure 2.7).

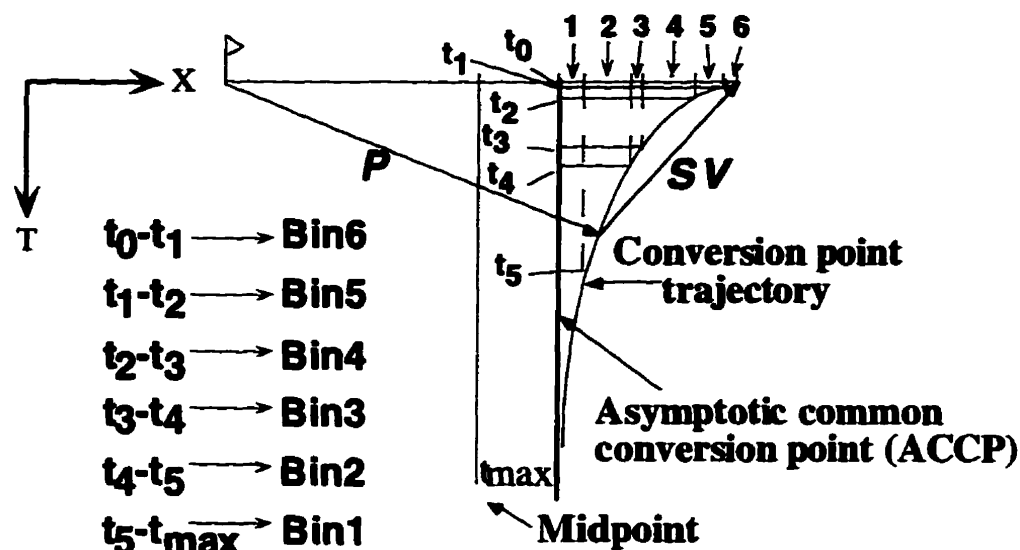


Figure 2.7: Schematic diagram of fast 3-D CCP binning. For each bin (numbered 1 to 6), the time samples within a bin are grouped together and assigned a bin number. (Modified from Wang et al., 1994a).

## 2.6 Receiver statics

The static solution for converted-waves is partially solved because the source static from the conventional P-P survey can be used (Garrotta and Granger, 1988; Cary, 1994b). The challenge lies in solving the receiver static. S-wave receiver statics are often ten times larger than the corresponding source static (Tatham and McCormack, 1991). Because the shear wave is largely unaffected in the near surface by the water table, which is a major factor for the P-wave, the shear and P-static are usually unrelated: That is, the shear static is not a scalar multiple of the P-static (Cary and Eaton, 1993) (Figure 2.8).

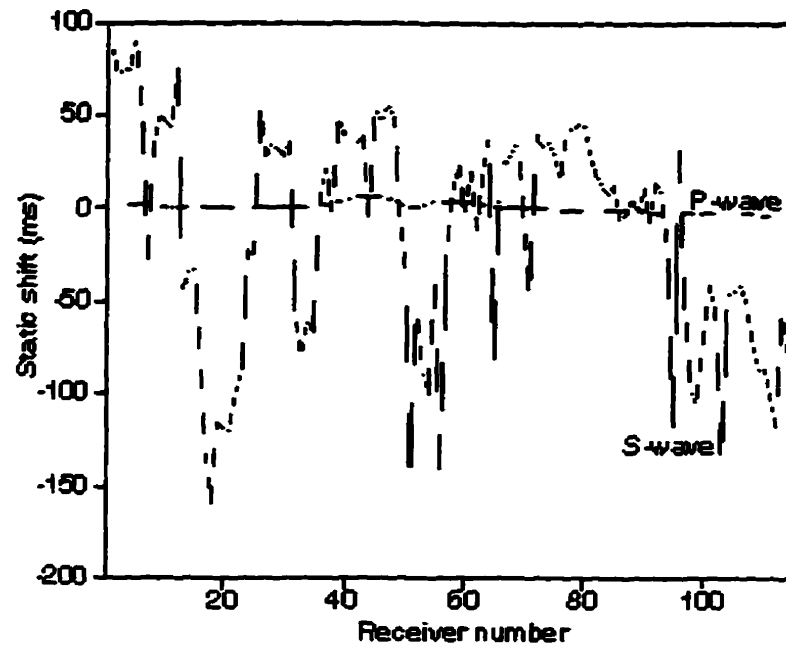


Figure 2.8: Comparison of P-wave and S-wave statics for 3C-2D data from Cold Lake, Alberta. Note the large S-wave static (from Isaac, 1996).

Common receiver stacks (Cary and Eaton, 1992) provide an initial residual receiver correction. The data are sorted into receiver gathers. An initial velocity provided by the P-P data, and scaled by a  $V_p/V_s$  ratio initially flattens the data in the gather, which is then stacked on the receiver stack section. Statics along a horizon are hand-picked or picked by correlation. These statics are applied to flatten the horizon (Figure 2.9). Flattening the horizon will correct for the short-wavelength and longer wavelength receiver statics. A finer residual correction can then be completed using more conventional residual statics corrections (Wiggins et al., 1976). Examples of this technique are shown by Harrison (1992) and Schaffer (1993).

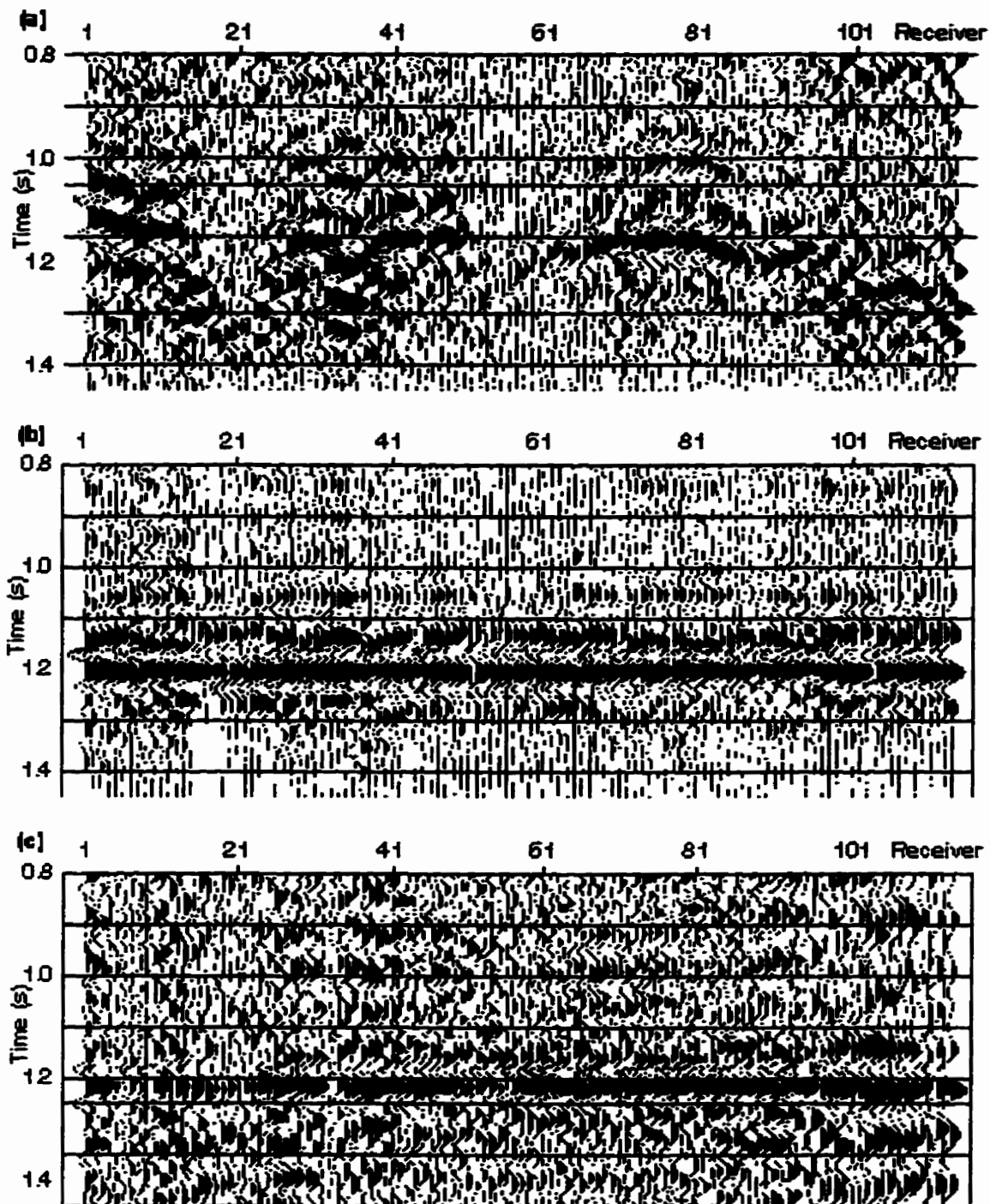


Figure 2.9: Receiver stack data from Cold Lake, Alberta: a) before, b) after alignment of the high amplitude event at 1.2 seconds, and c) the final receiver gather after the static correction. This method of statics is valid for relatively flat geology (from Isaac, 1996).

## **2.7 3-D P-S DMO**

Dip Moveout (DMO), which removes reflection point dispersal along dipping events, has been well established in a constant velocity medium for P-waves (Deregowski, 1982; Hale, 1984). Harrison (1992) develops DMO processes for 2-D converted-waves for a constant velocity. Wang et al. (1994b) extend Harrison's work and propose an approximate DMO operator for a linear velocity gradient medium in 2-D.

Cary (1994b) approximates a 3-D P-S DMO operator for a variable  $V_p$  and  $V_s$  by approximating a 2-D operator along the shot-receiver direction. By averaging the P- and S-wave velocities within Harrison's (1992) constant-DMO, a 2-D variable-velocity approximation is applied along each line of the 3-D. This approximation is suitable for flat geologic structure.

## **2.8 3-D P-S processing flow**

Figure 2.10 displays the proposed processing flow for 3-D converted-wave data. The first step is to process the conventional P-P survey. This will familiarize the processor with the data quality and geometry of the survey. The P-P survey will also provide the shot statics, the initial P-S velocities (scaled by a  $V_p/V_s$  ratio), and the migration velocities, which are 6 to 11% less than the P-S migration velocities (Harrison and Stewart, 1993). After the S1 and S2 separation, the shear-wave volumes are processed separately with different velocity analysis, migration velocities, and residual statics solutions.

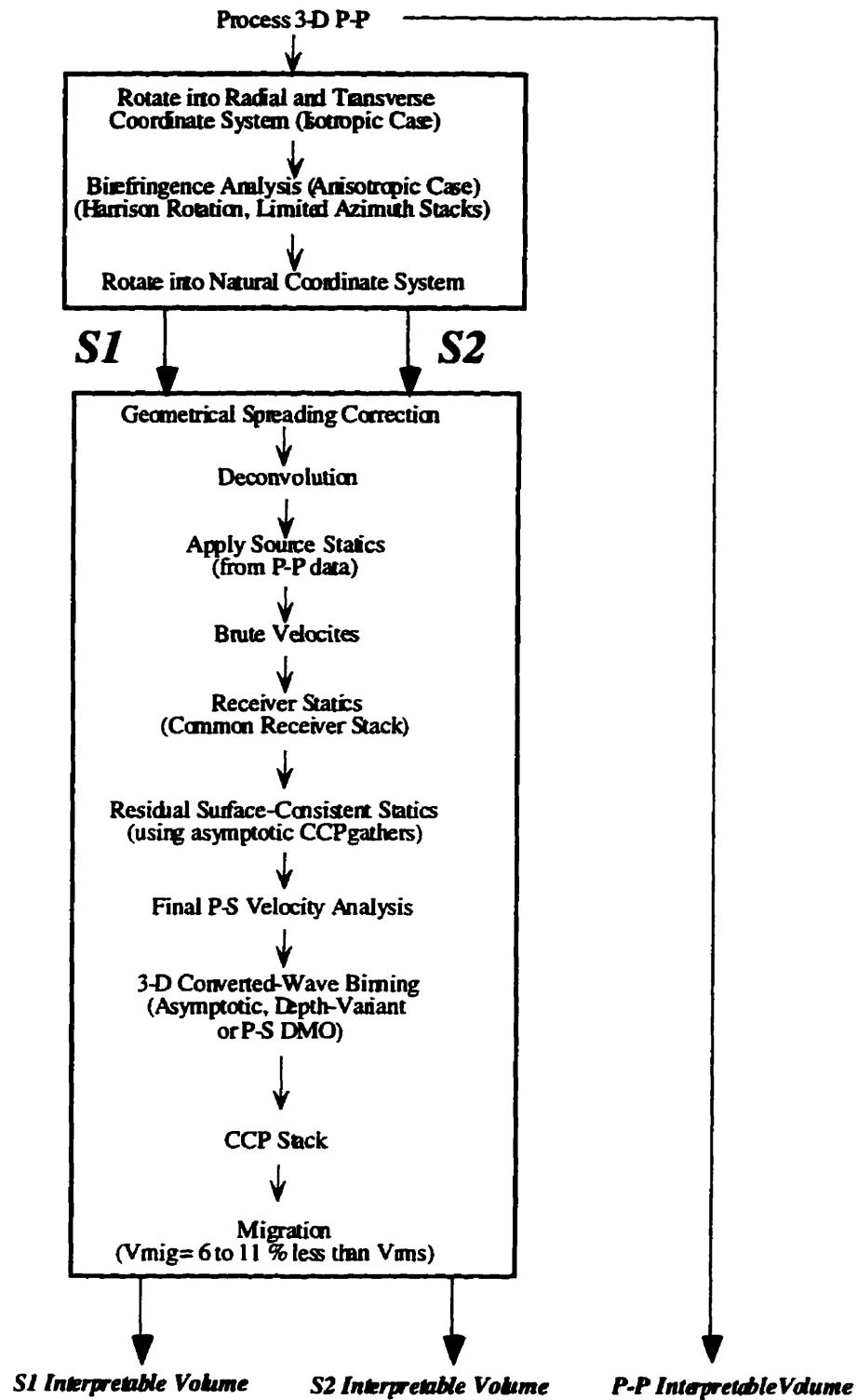


Figure 2.10: A 3-D P-S processing flow. Three products result from the processing. (Modified from Cary, 1994b).

## **2.9 Chapter Summary**

A 3-D P-S processing flow is built upon 2-D P-S processes developed previously. The key steps in processing are two coordinate rotations that rotate the data recorded on the H1 and H2 channels into two separate shear-wave polarizations of S1 and S2. After the separation, the shear-wave volumes are processed separately. This provides three times the amount of data for the interpreter.

A P-S NMO correction will flatten non-hyperbolic P-S reflections at high offset-to-depth ratios. P-S receiver statics, using common receiver stacks (Cary and Eaton, 1993), remove the short and long-wavelength receiver statics. Gathering can use the asymptotic or depth-variant technique, although the computationally efficient asymptotic method is commonly used. 3-D P-S DMO algorithms have been developed for a linear velocity gradient and constant gradient media (Wang et al., 1994).

The important results of 3-D P-S processing are the three independent data volumes. When the three are interpreted concurrently, they provide valuable information for the interpreter.

## **Chapter 3: Acquisition design of 3-D converted-wave surveys**

### **3.1 Introduction**

Acquisition is the first, and some would say, the most important step in achieving an interpretable seismic dataset. Acquisition design is an optimization problem (Musser et al., 1989) that consolidates, at minimal cost, the requirements of fold coverage, azimuth, and offset for a particular geologic target. The realities of access and terrain in the field are also factors in the design. As many variables as possible are included to make an informed decision as to which acquisition design is optimal for a particular area and subsurface target. The basis of the design is to achieve a reasonable areal distribution of subsurface reflection points, without any gaps, that have a nominal fold and have been sampled over a wide range of source-receiver offsets and azimuths (Galbraith, 1994). 3-D design has become a vibrant topic because it is seen as the weak link in the acquisition, processing, and interpretation process (Stone, 1994). The imposition of CCP design considerations make 3-D survey design even more complicated.

An advantage of converted-wave recording offers the simultaneous acquisition of shear and compressional waves by using the same source effort and receiver array. This makes it a considerably cheaper and faster method of acquiring and processing P- and S-waves than a pure-S 3-D survey (Garotta et al., 1990). Because of this duality in acquisition, the P-P and P-S surveys are not designed independently of each other: Optimal design attributes for both must be combined to achieve P-P and P-S migrated datasets for an integrated interpretation.

The basis of the design can follow the P-P (or CMP) survey using existing CMP design criteria because the compressional data will continue to provide the basis of the interpretation. For P-S elastic wave information to complement the acoustic interpretation,

CCP criteria must be included in the design without disrupting the acoustic data quality.

An inadequate survey design can severely compromise the converted-wave data, and minimize its contribution to the overall interpretation. The acquisition parameters for both surveys will be reviewed, and a design integration will be proposed.

## 3.2 3-D CMP design strategies

### 3.2.1 Design calculations

The steps in survey design for a standard orthogonal source and receiver line geometry are summarized in Figure 3.1 (Galbraith, 1994; Stone, 1994). The initial step in 3-D or 2-D design is to determine the basic parameters of bin dimension, the depth of target, the fold required, the record time, the survey size, and the maximum and minimum offsets required to image the shallowest and deepest targets. These parameters are compiled by geological modelling or previous surveys in the area.

The most important calculation is the number of shots per km<sup>2</sup> (Stone, 1994) which is determined by:

$$NS = \frac{F}{C \cdot b_x \cdot b_y} \quad , \quad (3.1)$$

where NS = the number of shots per km<sup>2</sup>

F= the nominal fold

C= the number of recording channels available

b<sub>x</sub>= bin dimension in the x direction (km)

b<sub>y</sub>= bin dimension in the y direction (km)

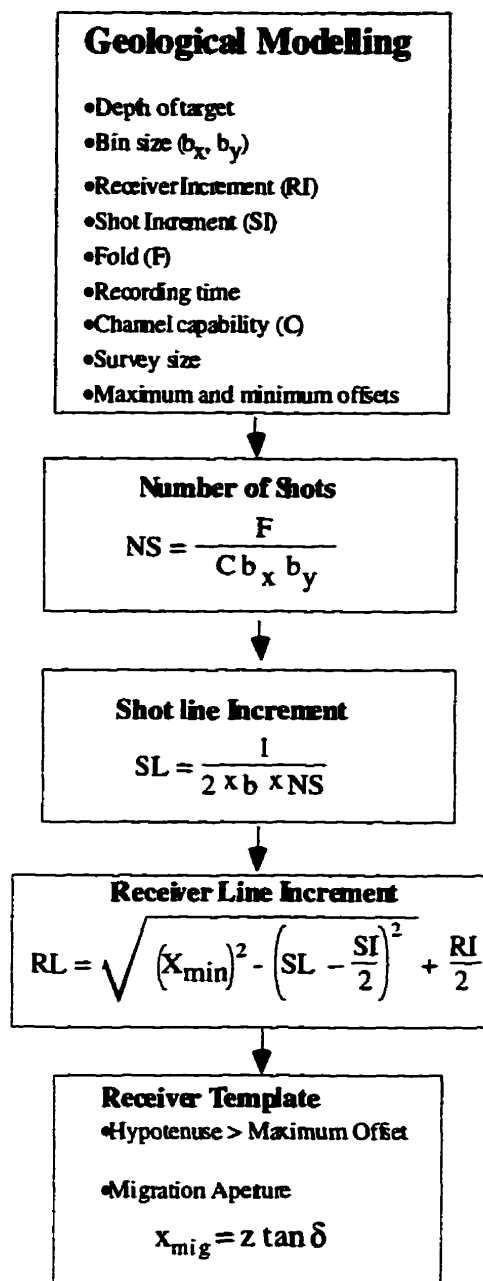


Figure 3.1: Steps in 3-D P-P survey design. The design is for orthogonal source and receiver lines, which is the most common geometry for land 3-D surveys. (Modified from Galbraith, 1994; and Stone, 1994).

The NS parameter is the basis for all the other parameters that follow. The next parameter is the shot line increment (SL). The SL value allows the minimum fold to be produced with the desired bin size and channel capability (Stone, 1994):

$$SL = \frac{l}{2 \cdot b \cdot NS} \quad , \quad (3.2)$$

where SL = the shot line increment  
 b = the bin dimension perpendicular to the shot line orientation  
 NS= number of shots/km<sup>2</sup>.

The largest minimum offset ( $X_{\min}$ ) within a bin controls the receiver line increment (RL). The  $X_{\min}$  should be less than the depth of the shallowest reflector that needs to be recorded (Galbraith, 1994). This ensures adequate imaging of the shallowest reflector. From Figure 3.2, the RL is related to the SL and X by the Pythagorean relation of:

$$RL = \sqrt{(X_{\min})^2 - \left(SL - \frac{RI}{2}\right)^2} + \frac{SI}{2} \quad , \quad (3.3)$$

, where RL = receiver line increment  
 SL = shot line increment  
 $X_{\min}$  = the largest minimum offset  
 SI = shot spacing  
 RI = receiver spacing.

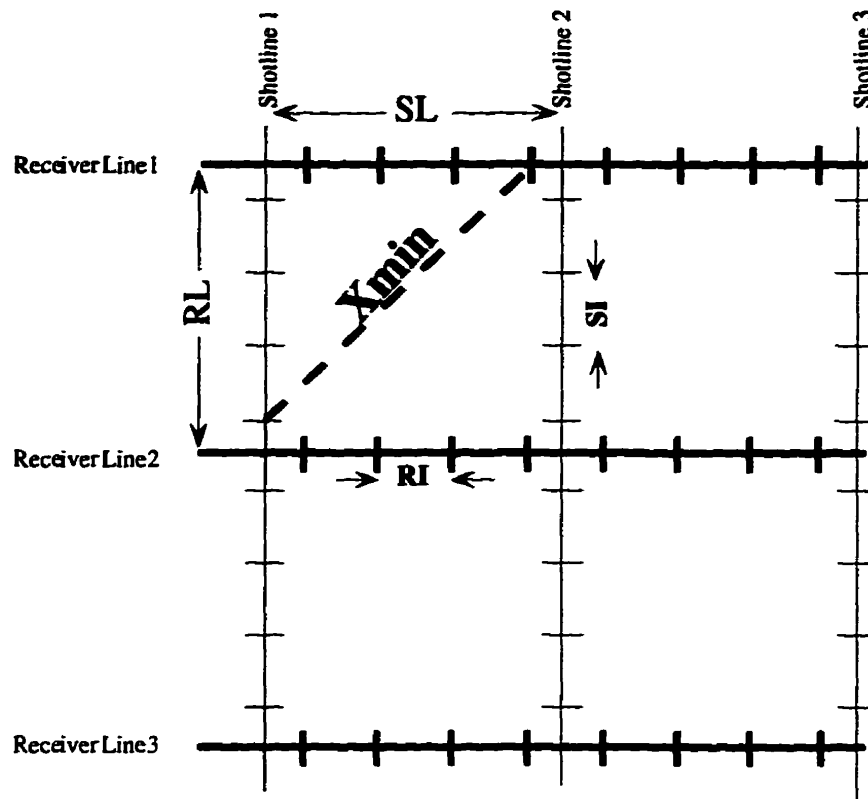


Figure 3.2: The largest minimum offset ( $X_{min}$ ) is defined as the hypotenuse between the furthest shot and receiver pair within the rectangle formed by adjacent shot and receiver lines. It is common for the shot and receiver lines to cross between the source and receiver stations.

The area covered by the live receivers, known as the receiver template or recording patch, is determined by RL and SL as well as the number of channels in the recording system. As a rule of thumb, the dimensions of the template need to be shaped in such a way as to exceed the maximum depth of the target (Stone, 1994). The hypotenuse of the receiver template (Figure 3.3) must exceed the maximum depth to target. In the case of dipping structure, an additional offset must be computed: The migration aperture (Yilmaz, 1989) is the additional recording offset that must be included for dipping structure to be imaged. One of the dimensions of the template can be extended to record the additional migration aperture. The extension of a recording template in a preferential direction will

narrow the azimuth distribution, provided the same number of recording channels are used (Lansley, 1994).

The additional offset that must be included is:

$$x_{\text{mig}} = z \tan \delta, \quad (3.4)$$

where  $x_{\text{mig}}$  = migration aperture

$z$  = depth to the dipping target

$\delta$  = dip of the target structure.

The shape of the template and the position of the source within it determine the source-receiver azimuths within each bin. A wide range of azimuths ensure good statics coupling. They are also required for 3-D AVO analysis, the detection of azimuthal anisotropy, and noise removal (Lansley, 1994). A wide distribution of offsets prevents aliasing and ensures a robust velocity analysis (Galbraith, 1994).

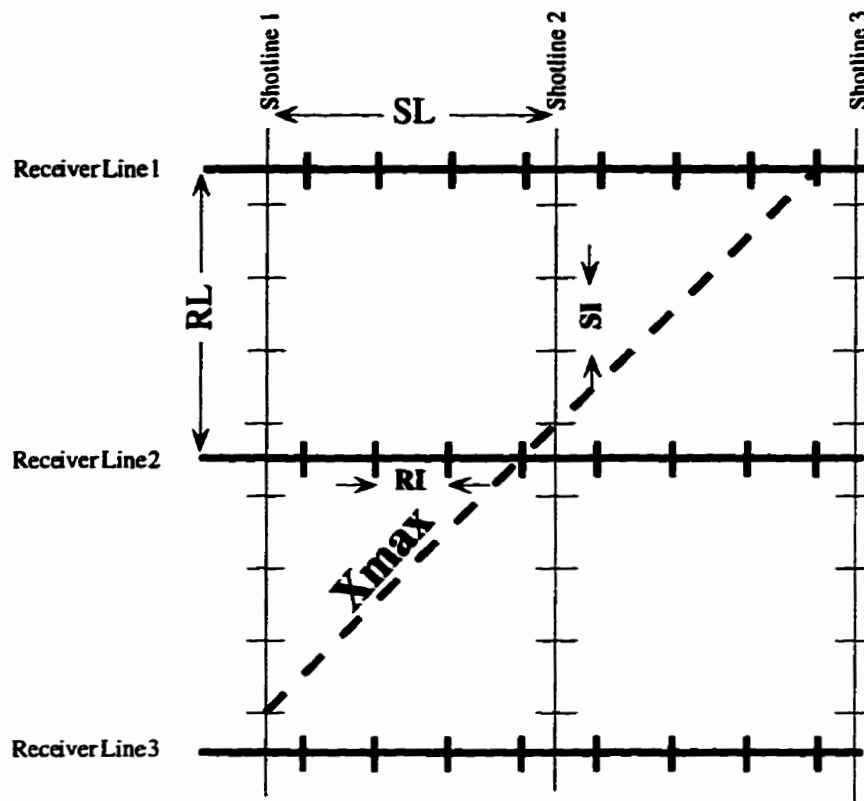


Figure 3.3: Receiver template consisting of 3 receiver lines and 8 groups per line. The maximum offset ( $X_{max}$ ), as defined by the hypotenuse of the receiver template, should exceed the maximum depth of target. The template can also be extended in one dimension to allow for the migration aperture.

### 3.3 Common 3-D CMP designs

#### 3.3.1 3-D marine surveys

Flexibility in marine 3-D geometries is limited. By nature of its acquisition, marine surveys have narrow azimuths. Boat and streamer arrangements limit the acquisition to recording with a series of tightly-spaced receiver lines that result in a narrow receiver patch. This characteristic can pose problems especially in areas involving structural geology (Lansley, 1994). It can also limit the velocity analysis to one preferential direction. Marine

surveys are commonly acquired in the dip direction to prevent aliasing along strike. Other surveys have acquired dual surveys with perpendicular recording directions to better image salt dome structures (O'Connell et al., 1993).

### **3.3.2 3-D land surveys**

Galbraith (1994) describes receiver and source geometries in use for land common-midpoint (CMP) surveys. Each 3-D layout geometry has its advantages and disadvantages in logistics, data quality; and distribution of fold, azimuth, and offset. Acquisition geometries are continually modified to achieve the goal of properly imaging the subsurface target at a reasonable cost. The following are some common land 3-D surveys that have evolved (Galbraith, 1994; Stone, 1994) in response to achieving an optimally designed CMP survey.

#### **3.3.2.1 Straight line**

The straight line geometry has a grid pattern of shots and receivers (Figure 3.4). Shots on one source line between two receiver lines (shown as an ellipse) are fired sequentially into a receiver patch of live receivers (black rectangle). The patch is then rolled along (shown in grey), and the process is repeated. The advantage to this design is that it allows for simple equipment moves and logistics.

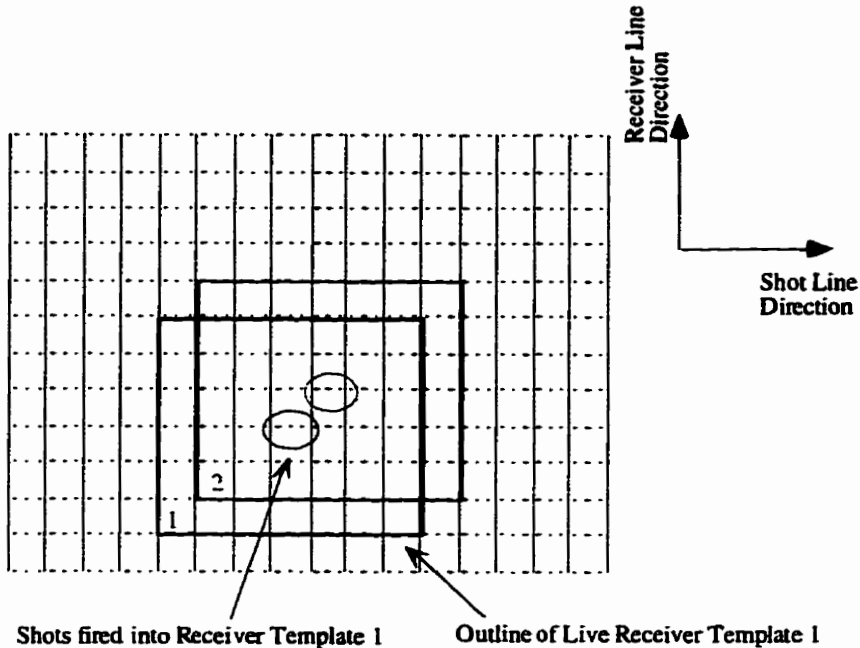


Figure 3.4: Straight line 3-D survey geometry. Dark and grey solid squares outline successive live receiver patches for the shots (circled).

**3.3.2.2 Swath**

In a swath survey, shots between several receiver lines are fired into a stationary patch (Figure 3.5). The patch then rolls along for the process to be continued. The advantage of this stretch version of the straight line method is its faster acquisition time because of reduced equipment moves. The disadvantages are poor offset and azimuth distributions.

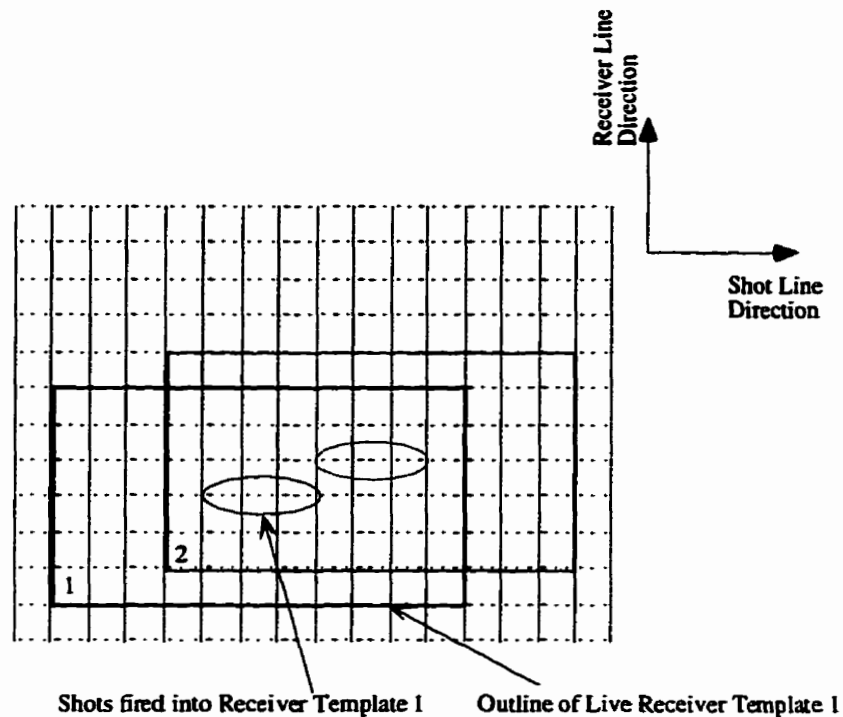


Figure 3.5: Swath 3-D survey geometry.

### 3.3.2.3 Brick pattern

Shot lines between adjacent receivers are staggered, resulting in the brick-like pattern (Figure 3.6.). This geometry reduces the largest minimum offset. In a regular grid pattern, the shortest near offset, the closest distance between a shot and a receiver in the grid, occurs at the diagonal of the box formed by adjacent shot and receiver lines.

Having a low value for the largest minimum offset means that the shallow events above the target have a better chance in being imaged. It does however, require a greater ease of access and placement, which is not always possible in wooded or mountainous areas.

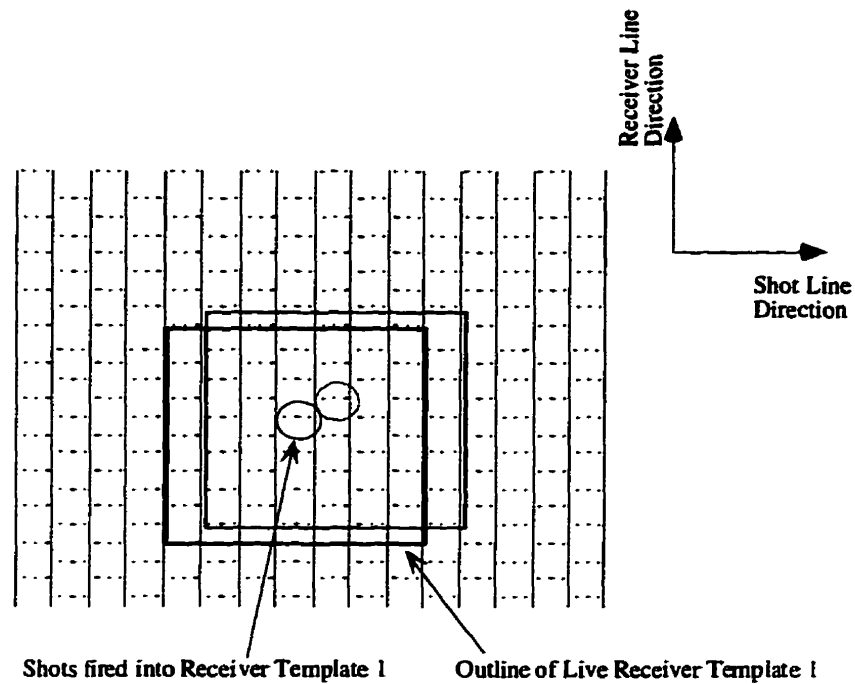


Figure 3.6: The Brick pattern.

#### 3.3.2.4 Button pattern

The unique feature of the button pattern is that the shots are fired outside the recording patch (Figure 3.7). Geometries with shots fired within the patch are weighted toward the long offsets (Cooper, 1993). The button pattern provides excellent offset and azimuth distribution, which is essential for residual and refraction statics. This type of survey has a high channel demand and requires a large number of shots per patch.

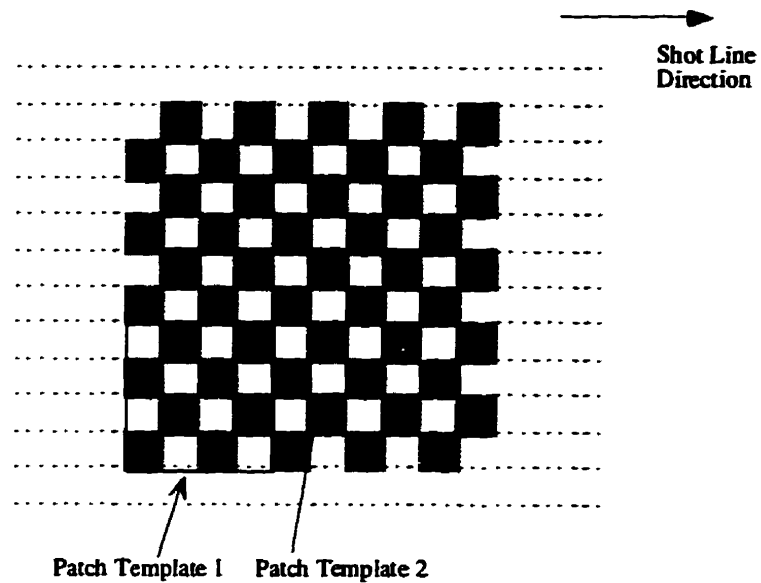


Figure 3.7: The Button pattern. The receivers are grouped into buttons (grey shaded areas). All shots lying outside the receiver button (within a given radius) are fired into it.

### 3.3.2.5 Zigzag

The zigzag pattern is a variation of the Brick pattern. The individual shots are staggered between receiver lines, resulting in angled shot patterns (Figure 3.8). Like the straight-line, this pattern allows for efficient equipment moves, yet it requires a recording area with clear access; that is areas where the equipment can be moved easily in any direction.

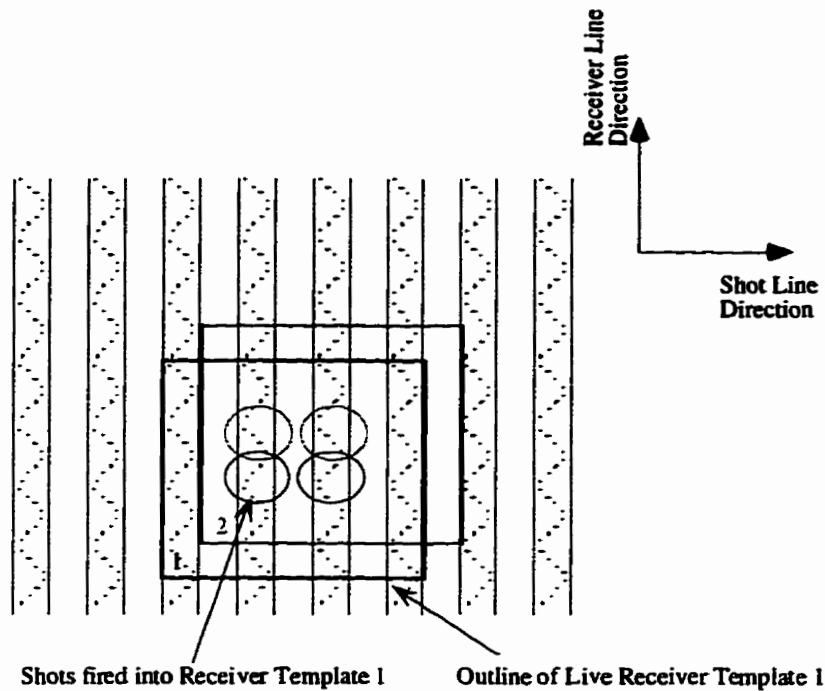


Figure 3.8. Zigzag Pattern.

### 3.3.2.6 Bin Fractionation (Flexi-Bin®)

In this pattern type, non-integral spacing of sources and receivers are set up to spread the midpoints out within a bin (Figure 3.9). The result is a finer subsurface sampling increment without having to decrease the source and receiver interval. One obtains higher resolution with little or no extra effort. Because the midpoints are distributed, this technique suffers from lower fold. To overcome this limitation, a high signal to noise ratio is required. The technique of bin balancing, that is borrowing offsets from other bins, is in effect a form of trace mixing, which may reduce the after-stack resolution. This technique has been applied in the design of the Blackfoot 3C-3D survey (Lawton et al., 1995).

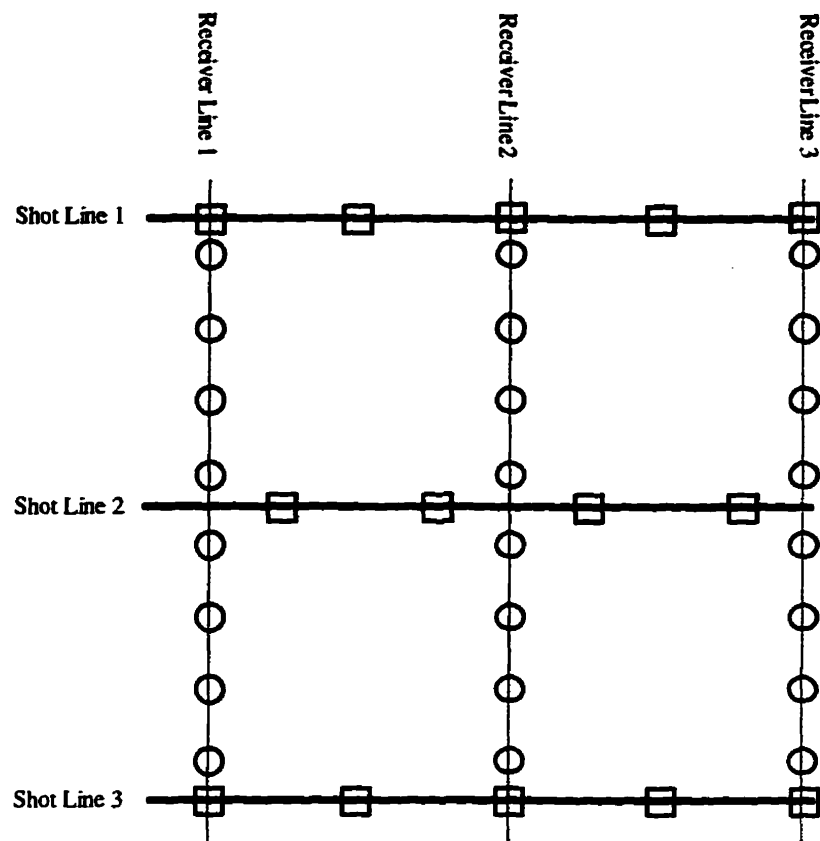


Figure 3.9: Bin fractionation. In this example, the shot positions are staggered by one-half the source interval on alternating shot lines. The receiver points can also be staggered. This method spreads out the midpoints throughout the bin.

### 3.4 3-D P-S acquisition issues

#### 3.4.1 CCP fold patterns

CMP surveys are designed assuming source-receiver raypath symmetry. With converted-wave surveys, however, the common conversion point (CCP) does not lie at the midpoint between the source and receiver (Figure 2.5). This lack of symmetry, when applied to a CMP acquisition design, alters the CCP fold pattern (Lawton, 1993) and can

result in a periodic distribution of low-fold zones. Rapid variations in fold have a detrimental effect in processing (Cary, 1994a), and can seriously compromise the converted-wave 3-D interpretation.

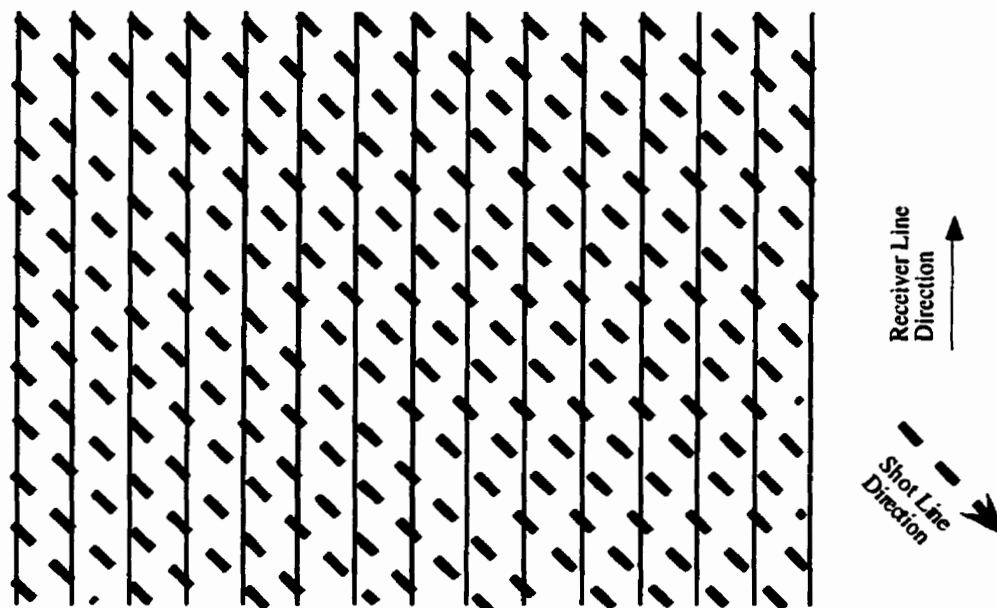


Figure 3.10: Survey geometry for the Joffre survey. The shot lines lie at a 45 degree angle to the receiver lines. This is a variation of the zigzag survey.

The Joffre 3-D design (Al-Bastaki et al., 1994) is a version of the zigzag pattern (Figure 3.10). It is based upon CMP considerations. The resulting evenly spaced CMP fold is shown in Figure 3.11. However, the resulting asymptotic CCP fold map (Figure 3.12) consists of systematic fold gaps with rapidly varying periodicity. The two north-south lines of zero fold seriously compromises the usefulness of the P-S data. These problems can be avoided if CCP considerations are included in the design (Lawton, 1994).

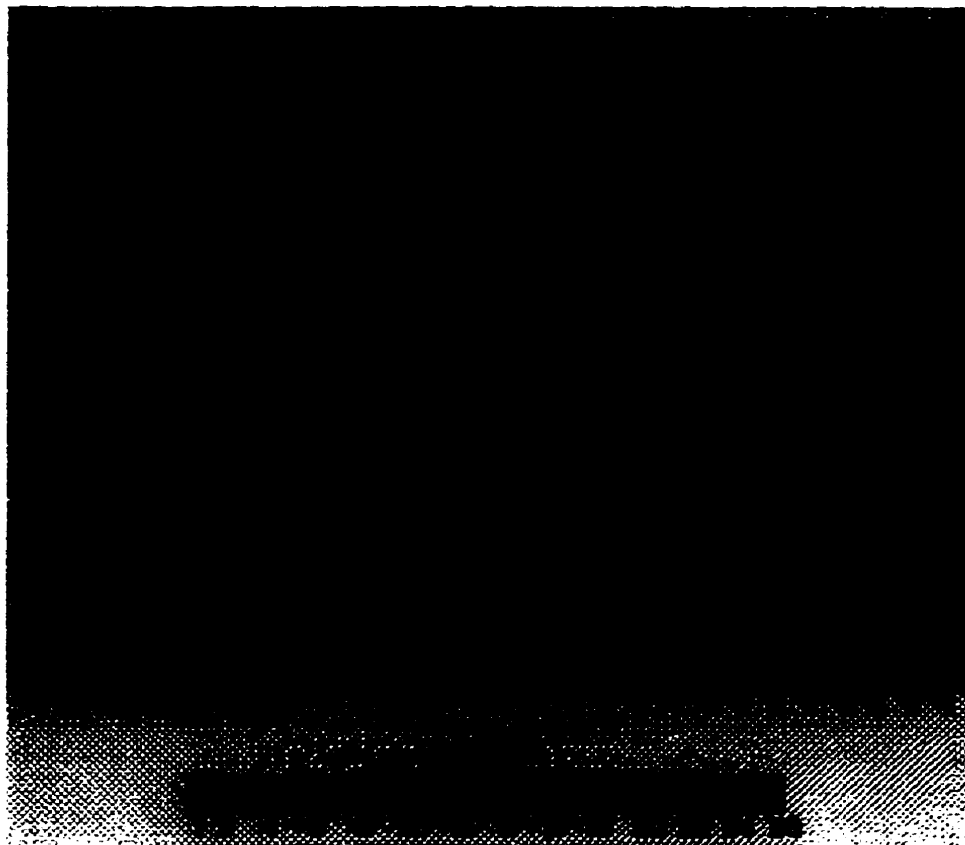


Figure 3.11: CMP fold distribution for the original survey at Joffre. Offset ranges used for the calculation: 0-2000m. From Lawton, 1993.

### 3.4.2 Optimal bin size for CCP 3-D recording

Lawton (1993) has developed an optimal bin size for converted-wave 3-D surveys. High frequency CCP fold patterns, that occur with CMP design criteria, are smoothed with a larger bin dimension. In processing, the bin dimensions are enlarged by the following formulae:

$$b_x = \frac{RI}{1 + \frac{V_s}{V_p}}, \quad (3.5)$$

and

$$b_y = \frac{SI}{1 + \frac{V_s}{V_p}}, \quad (3.6)$$

where  $b_x$  = inline bin dimension  
 $b_y$  = crossline bin dimension  
 RI = receiver spacing in the inline direction  
 SI = shot spacing in the crossline direction  
 $V_p$  = P-wave velocity  
 $V_s$  = S-wave velocity.

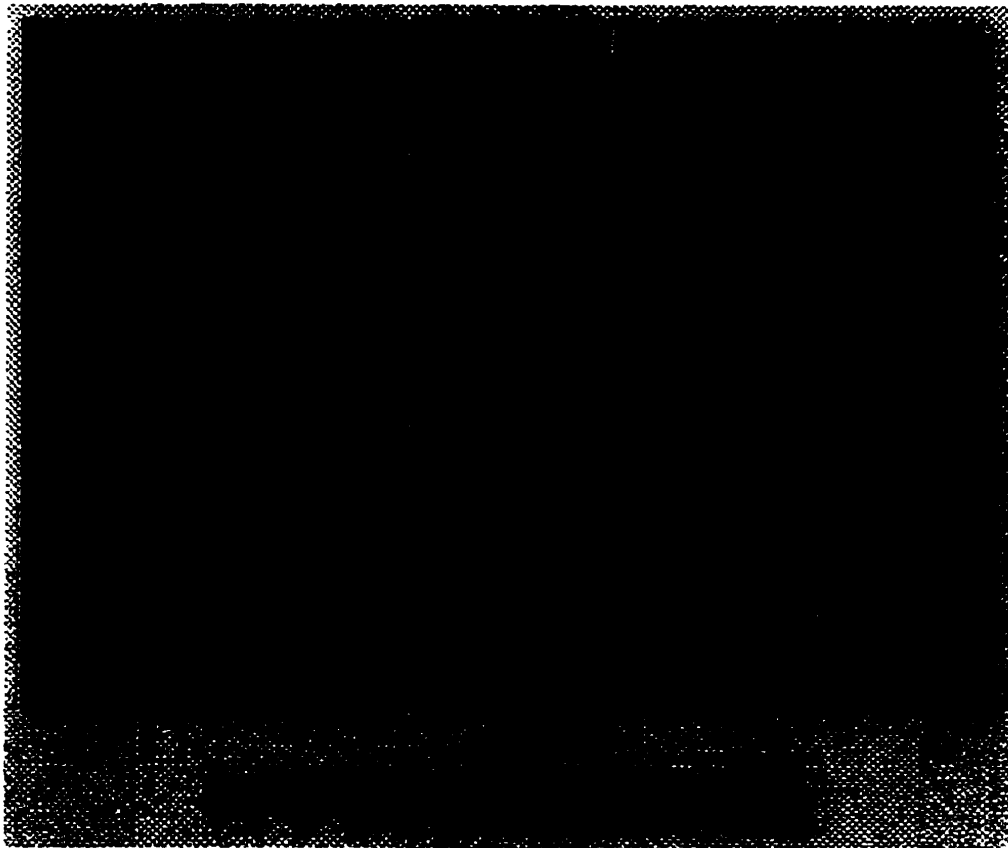


Figure 3.12: CCP optimized fold map, using an asymptotic binning approximation with  $V_p/V_s=2.0$ . Note the gaps of zero fold. This underlies the problem of attempting to CCP bin the seismic data over a survey geometry designed only for CMP recording (from Lawton, 1993).

### **3.4.3 Channel capability**

CMP 3-D surveys are well-established in industry. The trend is towards larger surveys with correspondingly higher channel demands: Common marine and land P-P surveys can approach up to 3000 live channels (Stone, 1994). However, the use of 3-C geophones in converted-wave and pure shear 3-D acquisition places high demand on the channel availability; requiring three times the number of channels versus a CMP 3-D survey. As multicomponent 3-D surveys become more popular, the demand for 3-C geophones will increase. Until the channel capability is raised and the availability of 3-C geophones becomes more common, the size of the receiver template will be somewhat smaller for multicomponent 3-D surveys.

### **3.4.4 Field procedures**

Most 3-C geophones are not placed in arrays, because of the channel demand and geophone scarcity. To compensate for the lack of receiver arrays, source arrays can be employed (Cooper, 1993). Group intervals should be smaller to reduce the chance of spatial aliasing. Applying polarization filters with 3-C geophones can suppress ground roll (Zheng and Stewart, 1993).

Each 3-C geophone must be leveled in the field to record effectively. Extra time is needed to accurately level each geophone, thereby increasing acquisition costs. To record converted-waves, the listen time must also be increased to at least 1.5 times of the P-P survey. Due to the additional setup time, the layout of the geophones should occur as early as possible. Wind noise, which can contaminate the horizontal channels is also a concern. To mitigate this noise problem, the geophones should be placed in an augured hole about 12 inches deep.

### 3.4.5 P-S Fresnel zones

Fresnel zones are used to estimate the lateral resolution of unmigrated stacked seismic data. The concept of Fresnel zones for P-S waves has been developed by Eaton et al. (1991). For surface seismic, the P-S Fresnel radius has been derived as:

$$R_{F_{p-s}} = \frac{V_m}{2} \sqrt{t_{0_{p-s}} * T}, \quad (3.7)$$

where  $R_{F_{p-s}}$  = the P-S Fresnel radius  
 $V_m$  = zero-offset P-S migration velocity  
 $T_{0_{p-s}}$  = vertical P-S raypath travel time  
 $T$  = the dominant period.

For the same depth and frequency having a  $V_p/V_s$  ratio of 2, the P-S Fresnel radius is about 80% smaller than the P-P Fresnel radius..

### 3.4.6 Marine 3-D CCP surveys

Most of the exploitation of recording converted waves has taken place on land (Tatham and McCormack, 1991). Because shear-waves are not supported within a fluid (Sheriff and Geldart, 1982) the direct recording of shear-waves cannot be recorded at the ocean surface, unlike their marine P-P counterparts. Tatham and Goolsbee (1984) recorded shear information with conventional pressure hydrophones at the surface of the ocean by recording S-P conversions from the ocean bottom. A direct measurement of marine converted-waves has been presented by Berg et al. (1994) using conventional air gun sources at the ocean surface with ocean-bottom 3-C geophones. This SUMIC®

technique has yet to be applied in 3-D, but its future appears promising. It also opens up another 70% of the world to converted-wave seismic exploration.

### **3.5 Design integration**

The acoustic survey, being the major contributor to the interpretation, should not be severely compromised by the complementary acquisition of P-S data. With minor adjustments to survey parameters, both the acoustic and elastic surveys can be recorded together to provide a value-added interpretation.

In CCP design, compensating for the periodic fold distribution that can occur under an exclusive CMP design becomes the major concern. The CCP tracing gathering option of bin optimization (Lawton, 1993) has two detrimental effects:

- 1) Lateral resolution is reduced with the larger bin size.
- 2) The bin dimensions of the P-P and P-S datasets will not match. This prevents a direct comparison and integration of the volume attributes; such as the calculation of  $V_p/V_s$  ratios and comparison of event amplitudes.

Rather than imposing a CMP design upon the CCP portion of the survey, the design parameters for both surveys need to be altered to allow a full integration of their respective interpretive products.

Ensuring shot line intervals (SL) are an odd integer multiple of the receiver spacing (RI) (Lawton, 1994) offers the simplest and most effective way to integrate the datasets. P-S fold periodicity will be minimized, in addition to the removal of CCP fold gaps. Shear volumes will also have the same bin dimension as P-wave volumes, allowing for direct

attribute comparison and integration between the P-P and P-S volumes. Lawton et al. (1995) introduce the Flexi-bin® approach (discussed previously) to CCP field design for the Blackfoot 3C-3D survey. This method distributes the CDP and CCP locations within the bin, providing an even fold distribution.

As mentioned previously, the P-S Fresnel Zone, derived by Eaton et al. (1994), has an 80% smaller radius than the P-P Fresnel zone for the same frequency content. Therefore, the P-S survey should provide a higher lateral resolution. However, the frequency content of surface P-S seismic is often reduced due to near-surface attenuation, making the two Fresnel zones comparable. P-P design for this parameter should take precedence.

A proper multicomponent 3-D design incorporates the aspects of both the P-P and P-S portions of the survey. Figure 3.12 amends the 3-D design steps of Figure 3.1 to include P-S design criteria. Cost will be slightly higher than a conventional P-P survey, yet the largest and most prohibitive cost, from the shear sources, is avoided. Additional time in the field is required to level the geophones, although a self orienting geophone is being developed (Gallant et al, 1996). Listen times will be 1.5 times longer as a single P-P survey, and the receiver template will be smaller. Both recordings should not be severely compromised if the all the criteria are for both data recordings are known and properly accounted for.

### **3.6 3C-3D design example**

Consider a clastic target at 2000m that we wish to image with a 3C-3D survey. The desired bin size for adequate spatial resolution of the target has been deemed (from previous seismic data in the area) to be 25m x 25m. The desired P-P fold is 15. The survey size will be 10 km<sup>2</sup>. The number of 3-C geophones available for the acquisition is

only 700. The minimum depth that we wish to image is 700m. From this initial information, and the design criteria contained in Figure 3.13, a 3C-3D survey is designed. Figure 3.14 summarizes the design steps for the survey. Table 3.1 tabulates the final design parameters.

The shotline increment (SL) should be an odd integer increment of the receiver spacing (RI) to prevent CCP fold gaps. The SL is reduced from 584 to 550 metres to match this criterion. There is no apparent geologic structure so the receiver template need not be extended to allow for migration aperture. Patch size is 2500m x 2500m, allowing for adequate maximum offsets to be recorded. Depending on the need for wide offset or azimuthal distribution, any of the example arrays in section 3.3.2 can be used.

Finally, the criterion which affects the type of seismic grid is the ease of access. For example, a clear field without any obstructions allows for greater line position flexibility than, say, a forest area, where lines must be cut and equipment moves are limited. 3-D seismic field design is an iterative process where the needs of the interpreter, in terms of adequately imaging the target, must be balanced with environmental, equipment, weather, and terrain considerations. 3C-3D considerations complicate the design process further. Having more 3-C geophones available decreases the number of shots/km<sup>2</sup>, which in turn, increases the shot line increment. A wider shot line increment, reduces the number of total shots, thereby reducing cost and time. The design of a survey is not unique. Other designs could also serve adequately.

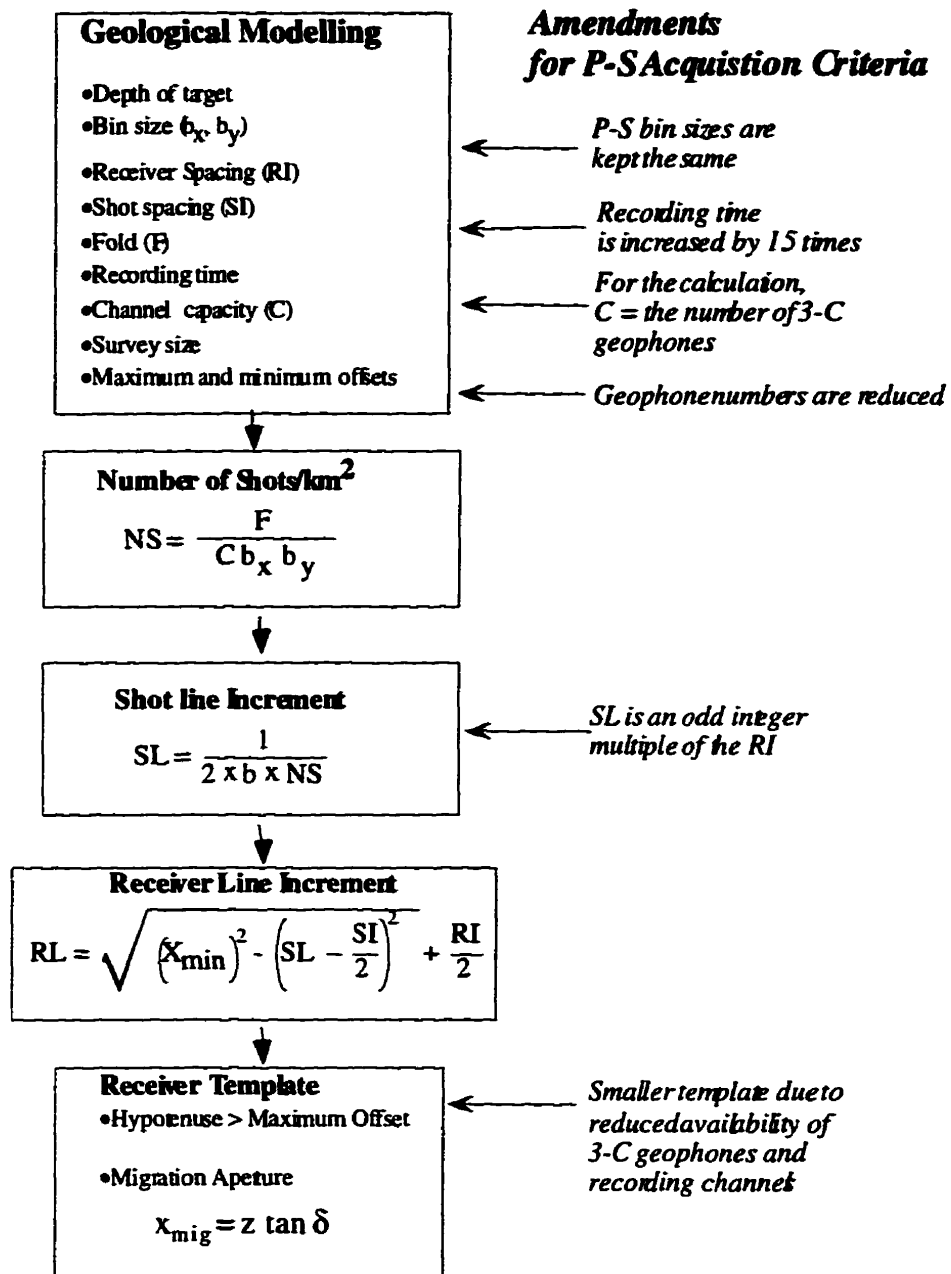


Figure 3.13: Amended 3-D design flow for the integration of CMP and CCP design parameters.

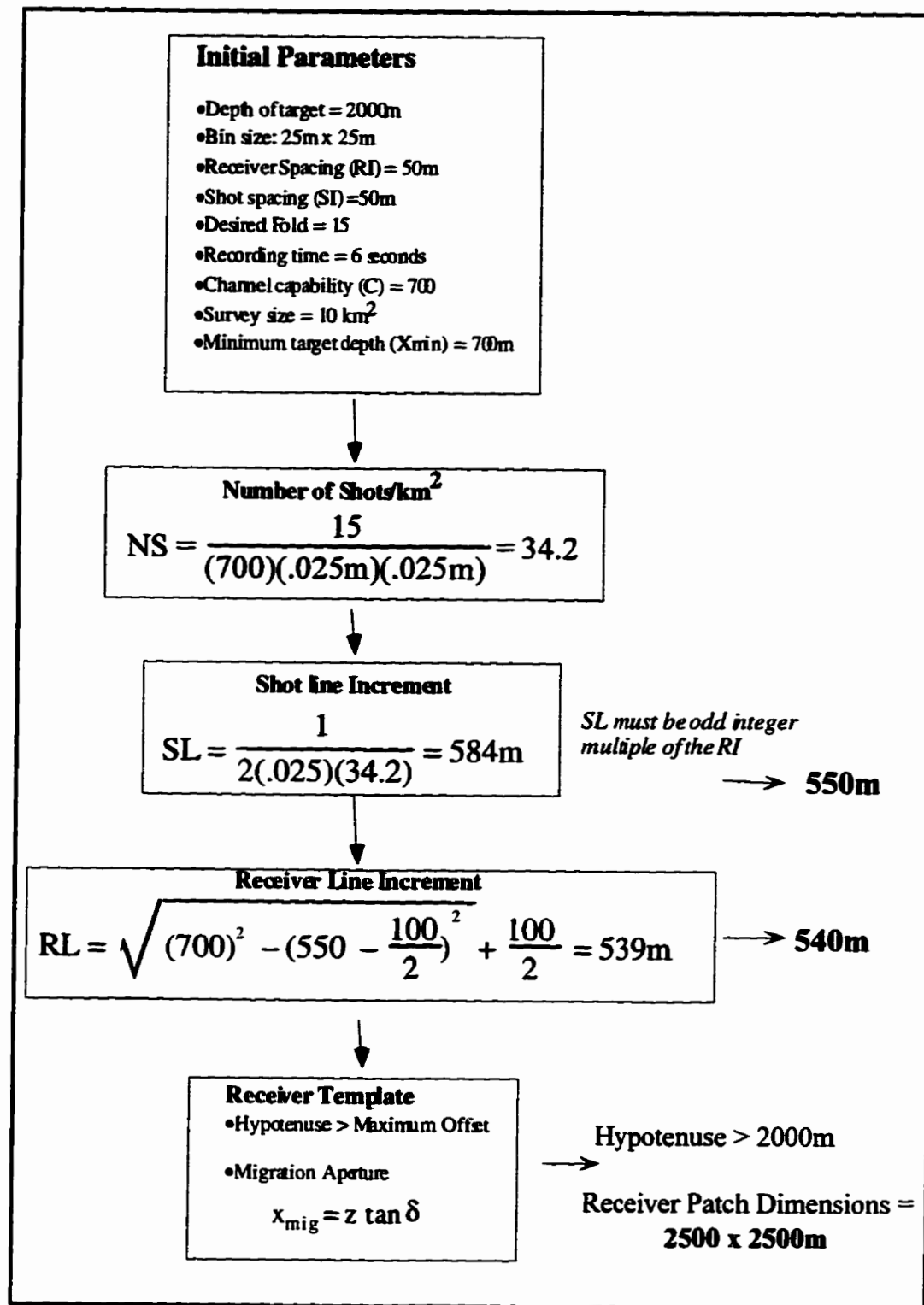


Figure 3.14: Design flow for the 3C-3D survey example.

<p>Shot spacing (SI) = 50m Receiver spacing (RI) = 50m Bin dimension = 25 x 25m</p> <p>Shot line increment (SL) = 550m Receiver line increment (RL) = 540m</p> <p>Recording template dimension = 2500 x 2500m</p>
---

**Table 3.1:** Final design parameters for example 3C-3D survey.

### 3.7 Chapter summary

3-D design is a popular topic because of its importance and concerns regarding its weakness in the acquisition-processing-interpretation flow. The advantage of simultaneously recording converted-wave and conventional seismic data can be lost if the acquisition design does not consider the design criteria of the P-S surveys.

Land P-P 3-D surveys have concentrated upon orthogonal source and receiver lines because of ease of operation. The acoustic 3-D will continue to provide the bulk of the interpretation and should not be severely compromised by the P-S survey. If the P-S data is to provide a tangible contribution to the interpretation, the P-S design criteria must be included in the design.

The simplest change to make without compromising the acoustic survey is to make the shot line an odd integer multiple of the receiver spacing, ensuring mitigation of debilitating fold gaps and allowing for P-S and P-P data to be directly compared and integrated into one encompassing interpretation.

## **Chapter 4: Interpretation of 3-D converted-wave data: Numerical model**

### **4.1 Model description**

This chapter introduces P-S interpretation techniques to 3-D geometry by analyzing a numerical model. Modelling can help the geophysicist anticipate effects in real data by making various assumptions or parameter changes in the synthetic case (Sheriff, 1991). Numerical modelling is useful in understanding and anticipating problems in field acquisition design, seismic processing, phase and amplitude analysis, and interpretation. This is especially important prior to engaging in an expensive field program. Two models are created: A clastic model with the zone of interest at 1500m depth and a carbonate model with a target at 2000m. The models are created using the Sierra MIMIC modelling system from Western Geophysical Inc. They are scaled to 10km x 10km and are based upon central Alberta Paleozoic and Mesozoic geology. Models are constructed in MIMIC and transferred to Sierra's QUIKSHT software for raytracing. The SLIPR module reformats the raytracing files, convolves the data with a wavelet, and writes the final synthetic shot records in SEG-Y format for 3-D processing.

#### **4.1.1 Clastic model**

The clastic model is based upon the Viking formation of central Alberta. Viking sand P-wave velocities ( $V_p$ ) are similar to the adjacent shales in the Western Canada Sedimentary Basin (Schaffer, 1993), making conventional seismic exploration difficult.  $V_p$  and formation thicknesses are taken from the 10-22-39-26W4 well and modelled after a Viking oil field over sections 4 to 6 in Township 39, Range 26W4. Nazar (1991) provides

shear-wave velocities ( $V_s$ ) in the Mesozoic section from the Carrot Creek field northwest of the study area. The  $V_s$  of the Viking sandstone is determined from an array sonic log at 9-5-39-3W5 over the Medicine River Field west of the study area.

Three sandstone channels are constructed in the MIMIC geologic model building package. The channels are described by two half-ellipsoids and one inverted hemisphere of thicknesses ranging from 15 to 25m, which are typical thicknesses for producing Viking fields in the area (Leckie et al., 1994). A plan view and cross section of the Viking bodies are shown in Figure 4.1 and 4.2, respectively. Table 4.1 describes the layer velocities and thicknesses.

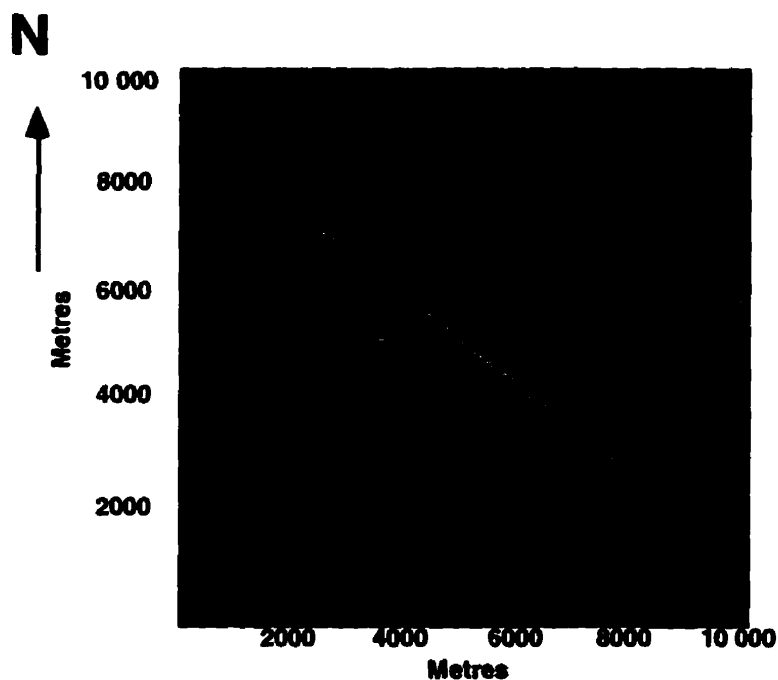


Figure 4.1: Plan view of clastic model. The thicknesses of the bodies range, from northwest to southeast: 15m, 25m, and 20m, respectively. The A-A' cross-section marker refer to Figure 4.2.

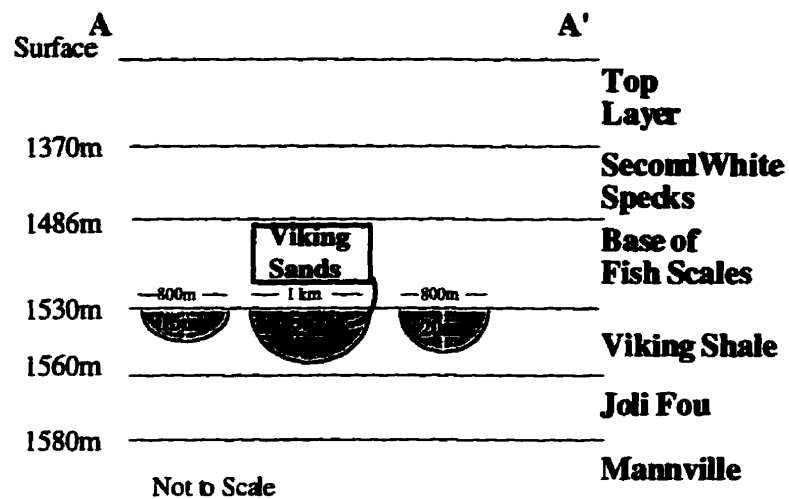


Figure 4.2: Cross-section of Clastic model.

Layer	Depth(m)	Vp(m/s)	Vs(m/s)	Vp/Vs
Top Layer	0	3500	1750	1.87
Second White Specks (2WS)	1370	3350	1876	1.79
Base of Fish Scales (BFS)	1486	3280	1574	2.08
Viking Sand	1530	4166	2541	1.64
Viking Shale	1530	4000	2000	2.0
Joli Fou	1560	2771	1330	2.08
Mannville	1580	4100	2457	1.7

Table 4.1: Clastic Model Layer Velocities and Thicknesses

### 4.1.2 Carbonate model

The carbonate model is a stratigraphic trap of a dolomitic reef to shale basin transition. The thickness and Vp values for the Wabamun, Nisku, and Ireton are taken from the 10-22-39-26W4 well. The Vs values result from estimated Vp/Vs ratios taken from the Miller et al. (1994) study of the Lousana field southeast of the 10-22-39-26W4 location.

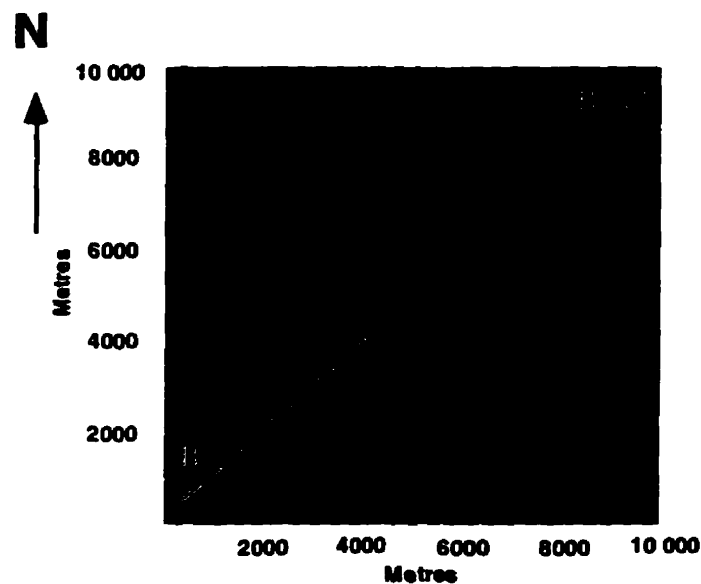


Figure 4.3: Plan view of carbonate model. The B-B' cross-section refers to Figure 4.4.

The model consists of 7 layers. Figure 4.3 and 4.4 show the model in plan view and cross-section, respectively. Encased at the top of the reef is a wedge of dolomite porosity. The porous zone increases in thickness from 8 to 32 metres from southeast to the northwest. Table 4.2 describes the layer values.

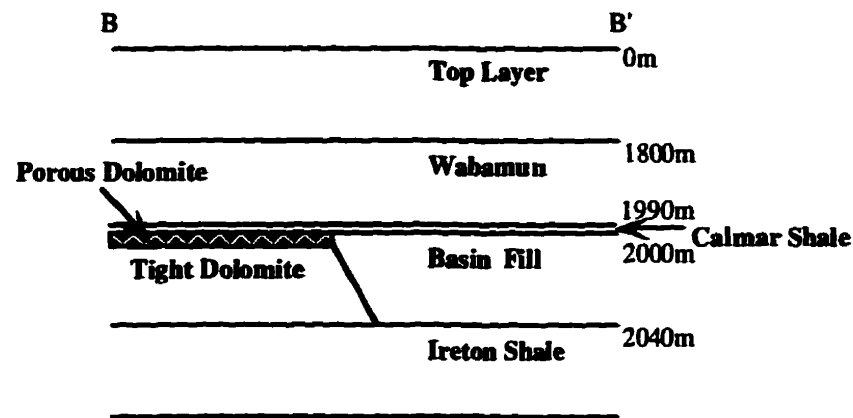


Figure 4.4: Cross-section of carbonate model

Layer	Depth(m)	Vp(m/s)	Vs(m/s)	Vp/Vs
Top Layer	0	3480	1740	2.0
Wabamun	1800	5995	3177	1.9
Calmar Shale	1990	5400	2592	2.1
Porous Dolomite	2000	5340	3043	1.75
Basin Fill	2000	6400	3200	2.0
Tight Dolomite	2008-2032	7090	3970	1.8
Ireton	2040	5500	2640	2.1

Table 4.2: Carbonate Model Velocities and Thicknesses

## 4.2 Data acquisition

Raytracing of the two models are completed using Sierra's 3-dimensional QUIKSHT offset raytracing package, which provides shot record simulations. The software uses a WKBJ raytracing technique for amplitude determination. Ray instructions are defined for each layer interface. The software is flexible enough to generate converted-waves. The raytracing uses a straight-line propagation between each layer and follows Snell's Law for traveltime estimates.

#### 4.2.1 Acquisition design

The same design parameters are used for both models, based upon the 3-D P-P and P-S design integration criteria described in Chapter 3. Table 4.3 summarizes the survey parameters. The bin size for the survey is set at 50m x 50m, resulting in a shot and receiver spacing of 100m. Coverage of the targets requires a 5600 x 5000m survey. Offset range, based upon the minimum and maximum depths of the two models, are 900 and 3000m, respectively.

The most important P-S design criterion is preventing empty CCP bins. CCP fold gaps can be mitigated by decreasing the shot line interval to 500m, an odd integer multiple of the receiver spacing, from its original CMP design of 600m. This prevents the imposition of empty bins and high fold periodicity that can occur if the design was based solely upon CMP considerations.

Receiver line increment (RL) defines the largest minimum offset. To image the shallowest layer at 900m, an RL of 800m is chosen. Eight receiver lines, consisting of 52 receivers each, record 616 shots. Selection of a receiver patch size of 416 receivers allows far offsets to extend to 7000m. QUIKSHT is inflexible in describing the movement of smaller receiver templates. For simplification, all receivers were left on for each shot. This array size would be unnecessary in a field setting, but the software limitations of the modelling system must be incorporated into the design criteria for the numerical model.

**Shot Spacing (SI) = 100m (56 shots/line)**  
**Receiver Spacing (RI) = 100m (52 receivers/ line)**

**Shot Line Interval (SL)= 500m\* (11 lines)**  
**Receiver Line Interval (RL) = 800m (8 lines)**

**Recording Template: 416 receivers live**  
**Bin Size = 50 x 50m**

**Offset Range: 0 - 7000m**

**Maximum P-P Fold: 44**  
**Maximum P-S Fold: 26**  
**(0 - 2600m mute)**

**Number of Traces for each mode (P-P and P-S): 240 000**

**\* Odd multiple of receiver spacing**

**Table 4.3: 3C-3D Recording Parameters**

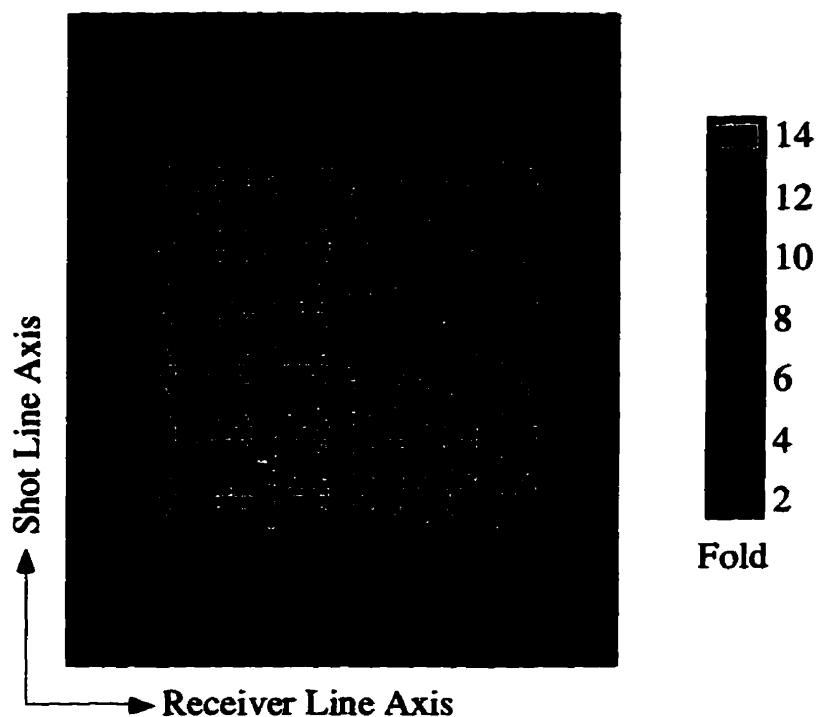


Figure 4.5: P-P model fold map. Offset range: 0-2600m.  
 Bin size = 50m x 50m.  
 Fold map dimensions = 5200m x 5600m.

Figures 4.5 and 4.6 display the CMP and CCP fold distribution for 0-2600m offsets. P-P and P-S fold maps for a shot line interval of 600m (an even multiple of RI) are shown in Figure 4.7. The fold periodicity of the P-S design (Figure 4.6) is smoother than a design with an even shotline integer spacing (Figure 4.7). An optimal bin size of 66.6m would smooth the P-S fold as well, but it is best to keep the bin sizes between the CMP and CCP data volumes the same for a consistent interpretation (Lawton, 1994).

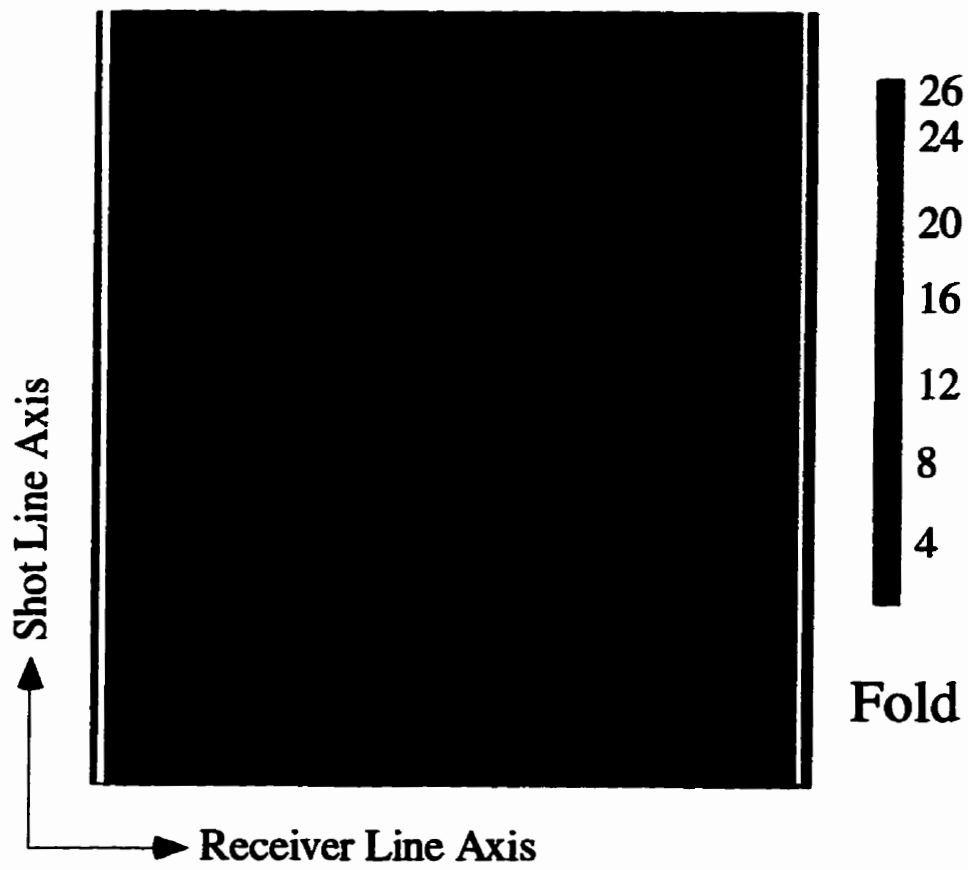


Figure 4.6: P-S numerical model fold map. Offset range: 0-2600m.  
Bin size = 50m x 50m. Fold map dimensions = 5200m x 5600m.

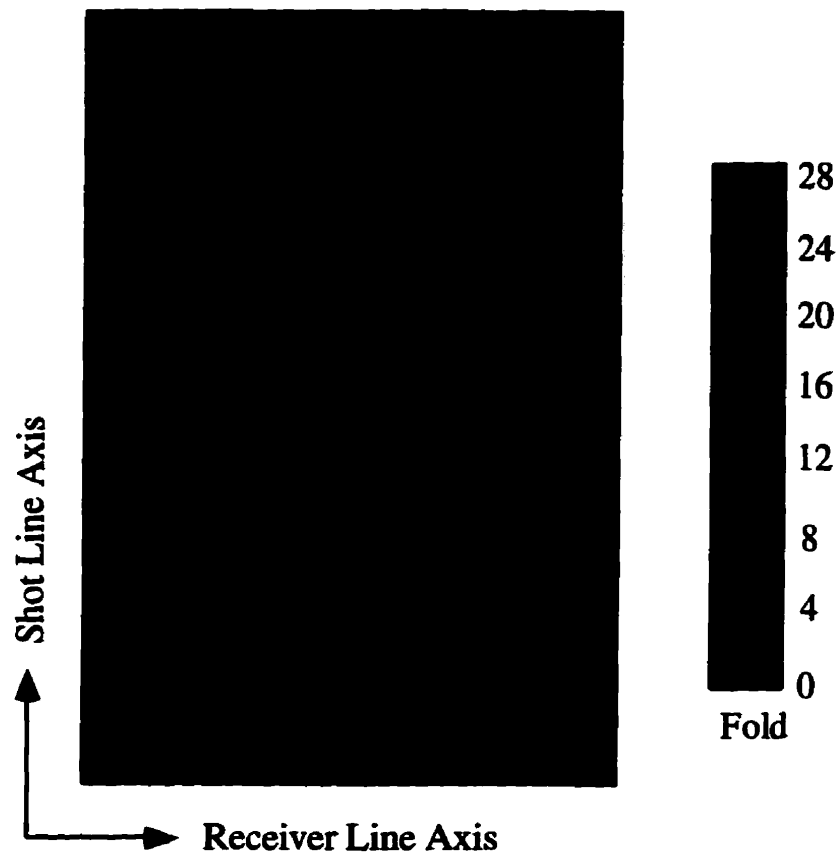


Figure 4.7: P-S Fold map for a shot line spacing of 600m (even integer of the receiver spacing). Note the fold gaps with this increment of shot line spacing. Fold map dimensions = 5200m x 5600m.

#### 4.2.2 Steps in acquisition

Figure 4.8 displays the acquisition steps required for the numerical model acquisition. The acquisition uses 3 separate Sierra modules: MIMIC (model construction), QUIKSHT (raytracing), and SLIPR (reformatting, convolution, and SEG Y output). The geologic model constructed within the MIMIC module is transferred to the QUIKSHT module. Within QUIKSHT, the source and receiver array is built. The survey is acquired twice for each model: Once for P-P ray instructions and once for the P-S ray instructions. SLIPR reformats and convolves the raytracing information into SEG Y format for processing.

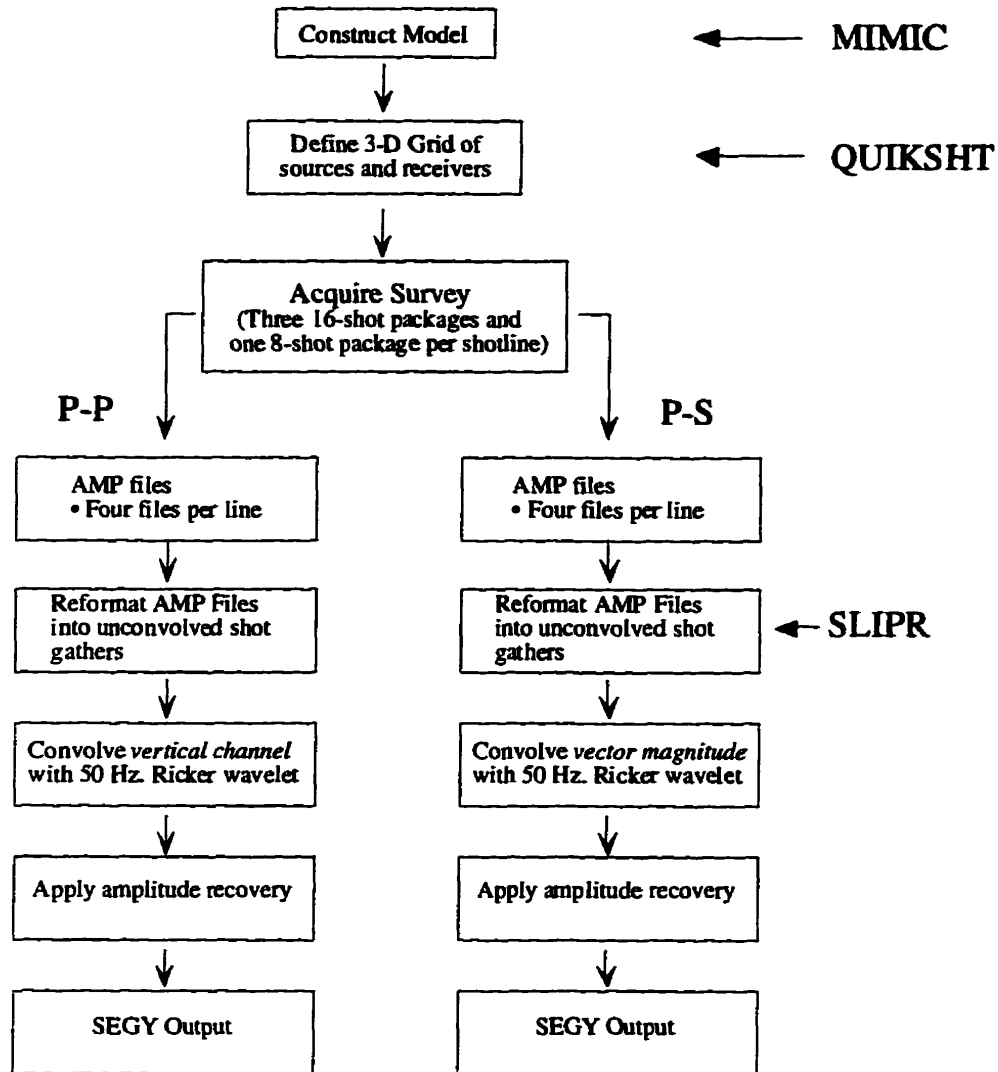


Figure 4.8: Acquisition steps of a 3-D numerical model for Sierra raytracing software.

#### 4.2.2.1 Raytracing

Amplitude (AMP) files are created during a QUIKSHT raytracing run. For each shot the rays are captured by the receiver array. Ray interaction at each layer is controlled by the ray instruction. AMP files store the captured ray's travel time, amplitude, and the ray instruction for each layer. Two separate raytracing runs are performed: One with P-P ray instructions, the other for P-S ray instructions. Internal memory constraints imposed

by the Sierra system limit the size of an AMP file to 16 Megabytes. Because of this constraint, only 16 shots can be stored per AMP file. To accommodate the large size of the survey, each shot line is separated into three 16-shot groups and one 8-shot group, yielding 44 AMP files for each full survey.

#### 4.2.2.2 Reformatting and convolution

The SLIPR module reformats each AMP file into 32 unconvolved receiver gathers (EDD files). Subsequent spike seismograms are convolved with a 50 Hertz Ricker wavelet.

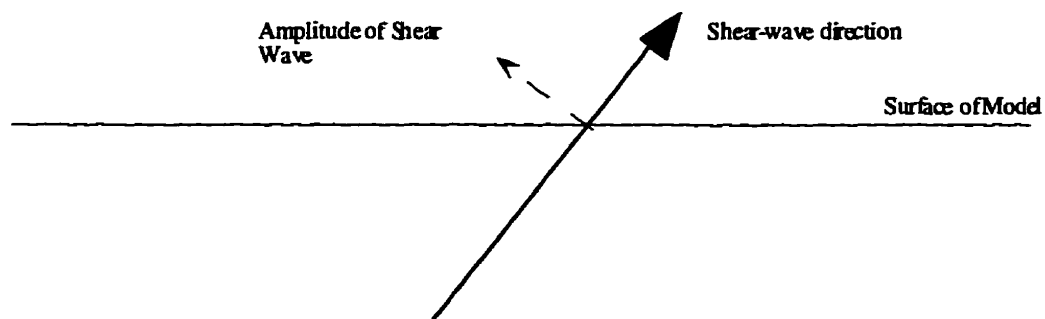


Figure 4.9: Vector magnitude of the incoming shear-wave raypath upon the Sierra system. This amplitude is recorded and convolved with the wavelet.

Convolution can take place on four different spikes: The vertical receiver component, the east-west and north-south horizontal components, or the total vector displacement (Figure 4.9). P-P survey data are convolved with the vertical channel. The shear wave amplitude component uses the convolution derived from the total displacement.

The total displacement is the amplitude of the shear wave perpendicular to the incoming ray at the measuring surface. This method is used for several reasons:

- 1) The data are recorded on only one channel, lowering disk space demand by one-half.
- 2) It effectively completes the radial-transverse rotation required if data were recorded on two orthogonal channels (Lane and Lawton, 1993). The model is isotropic, therefore energy is expected to be on the radial channel.
- 3) The model lacks a low velocity near surface layer that refracts incoming rays to near vertical. The vector magnitude removes P-P rays leaking onto the horizontal channels.

Geometric spreading amplitude recovery is applied at the convolution step. 128 SEGY files per shotline are created and imported into ProMax for processing.

## **4.3 Processing**

### **4.3.1 Pre-processing**

Prior to geometry assignment, the individual shot line SEGY files are combined to create the full 3-D survey. Final Sierra output presents 1408 separate SEGY files for each of the P-P and P-S surveys, where each file consists of 16 or 8 shot gathers sorted for each receiver line. To create one large file suitable for 3-D processing, the following steps are taken:

- 1) SEGY files are input by shot line. For each shot line, the FFID (field file identification number) header words are renumbered sequentially.

- 2) Shotlines are sorted by FFID and channel number. Each new shotline ensemble is written and merged together to form 56 shot gathers consisting of 416 receivers.
- 3) Repeat the above steps for the remaining shot lines.

### 4.3.2 3-D P-P processing

The processing flow for the P-P data is shown in Figure 4.10. Figure 4.11 displays a typical shot record for the survey. After pre-processing and geometry assignment, a velocity analysis is completed. Due to the simplicity of the model, a single velocity function is used. NMO and a 30% stretch mute is applied, followed by a stack and a 2-pass, 3-D f-k migration. The data, consisting of 102 inlines and 112 crosslines, are loaded into LandMark Seisworks® for interpretation.

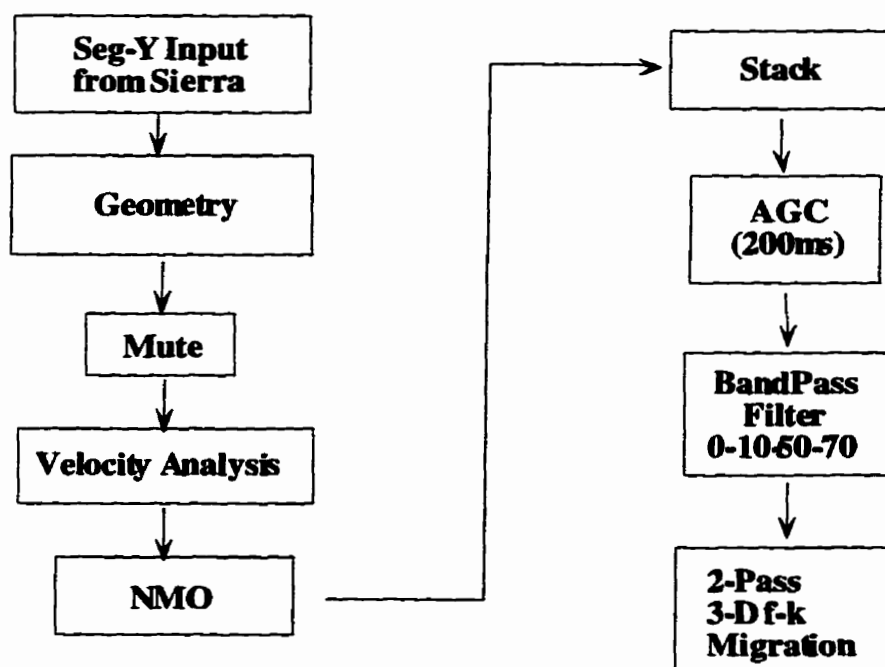


Figure 4.10: 3-D P-P processing flow.

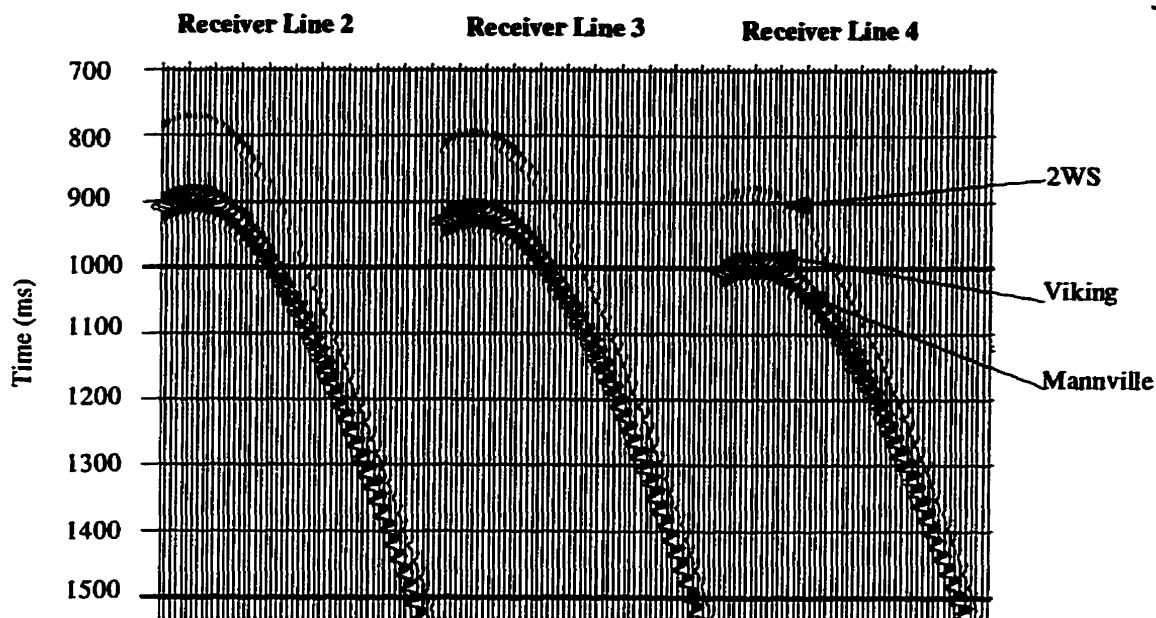


Figure 4.11: Shot record 47 of sand P-P model.

### 4.3.3 3-D P-S processing

The P-S processing flow is shown in Figure 4.12, with a typical P-S shot record shown in Figure 4.13. The flow follows the P-P flow except for the additional processes of CCP location and bin definition. As discussed in Chapter 3, data must be binned by CCP location. This is completed by manipulation of the header words in ProMax. The new CCP locations are calculated using the asymptotic approximation of equation 2.2.

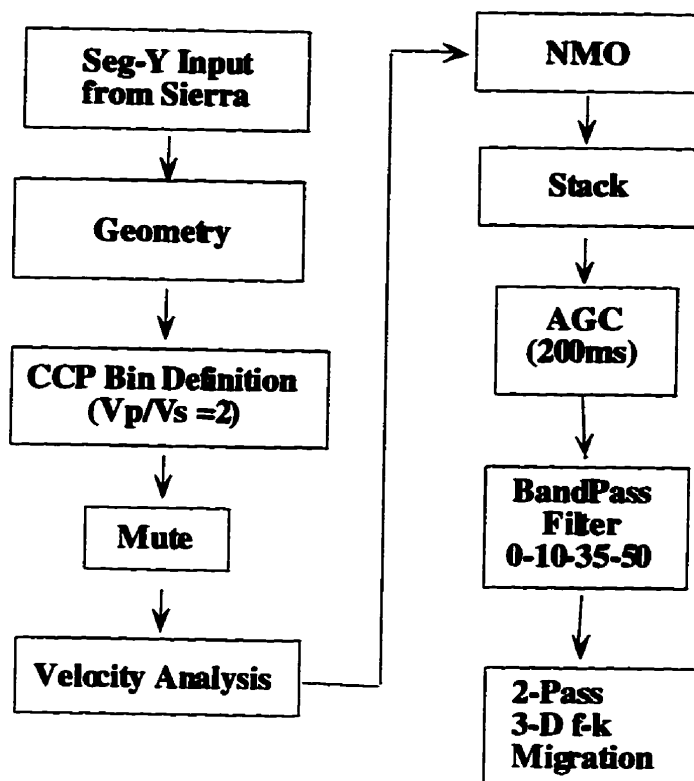


Figure 4.12: 3-D P-S processing flow.

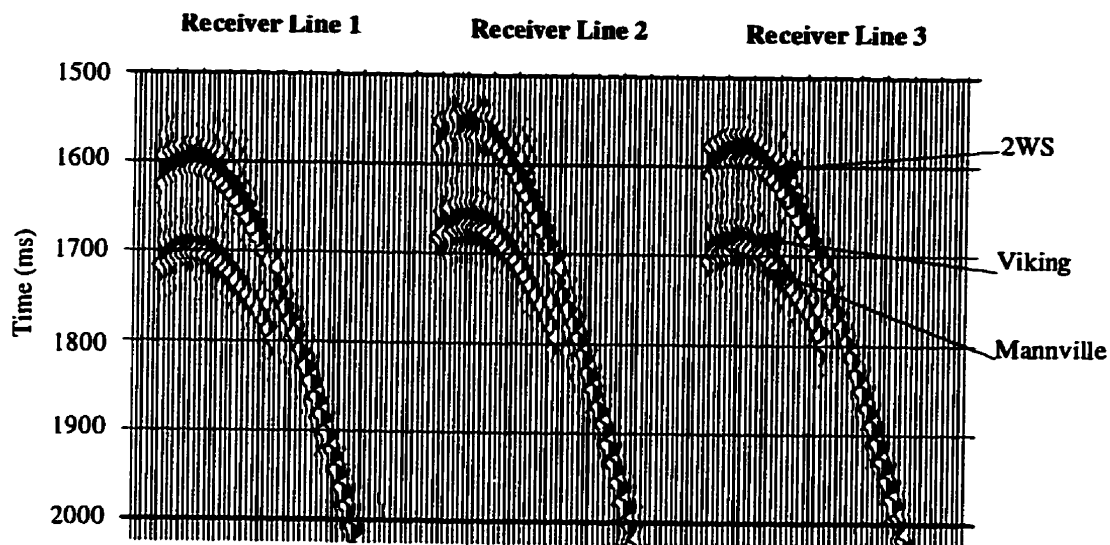


Figure 4.13: Record of shot 47 of 3-D P-S numerical model survey.

Data are re-binned at 50m bin sizes using updated CCP coordinates derived from the following equations:

$$\text{XLINE} = \left[ \frac{\text{XCCP} - \text{X}_{\text{or}} + \frac{b_x}{2}}{b_x} \right] + 1, \quad (4.1)$$

where **XLINE** = crossline number  
**XCCP** = asymptotic common conversion point X coordinate of trace  
**X<sub>or</sub>** = origin of X coordinate of survey coverage  
**b<sub>x</sub>** = bin size in x direction;

$$\text{ILINE} = \left[ \frac{\text{YCCP} - \text{Y}_{\text{or}} + \frac{b_y}{2}}{b_y} \right] + 1, \quad (4.2)$$

where **ILINE** = cross line number  
**YCCP** = asymptotic common conversion point Y coordinate of trace  
**Y<sub>or</sub>** = origin of Y coordinate of survey coverage  
**b<sub>y</sub>** = bin size in y direction;

CCP bins are given unique bin numbers by combining the ILINE and XLINE CCP flags:

$$\text{BIN} = \text{ILINE} * 1000 + \text{XLINE}, \quad (4.3)$$

where **BIN** = CCP bin number  
**ILINE** = CCP in line number  
**XLINE** = CCP cross line number.

Trace header values of CDP\_X, CDP\_Y, and CDP bin numbers are replaced with corresponding CCP values. With this replacement, converted-wave velocity analysis, stacking, and migration can be completed using standard CMP processes in ProMax.

The NMO correction does not incorporate the P-S NMO of Slotboom (1992) (see equation 2.1) because of the high offset-to-depth ratio and the correction formula has yet to

be implemented in the ProMax processing system. A 10-20-35-50 Ormsby zero phase bandpass filter is applied to the P-S data, lowering bandwidth with respect to the P-P volume (0-10-50-60 Ormsby filter) in anticipation of a lower field response for the shear data. For the deeper carbonate model, a 0-20-35-40 Ormsby bandpass filter is applied to the P-S volume because all frequencies should be lower as depth increases (Miller et al, 1994). The P-S stack is migrated by 95% of the RMS velocities derived from the velocity analysis (Harrison and Stewart, 1993). The migration is a 2-pass 3-D f-k method.

#### **4.4 Interpretation**

Interpretation techniques for converted-wave seismic data have been developed and discussed in the 2-D realm. At Carrot Creek, Harrison (1992) and Nazar (1991) have developed the techniques of S1 and S2 polarization separation, P-S and P-P AVO analysis,  $V_p/V_s$  ratios, and amplitude analysis. Miller et al. (1994) introduce a 2-D converted-wave interpretation flow at the Lousana Field: Here the concept of tying P-P and P-S synthetics to the conventional and P-S sections are shown. Also, isochron mapping of P-S and  $V_p/V_s$  ratio profiling are also introduced.

3-D interpretation of conventional P-P seismic data have been well established (e.g. Brown, 1991). Concepts such as *mapping* of attributes, time slices, structure mapping, 3-D visualization, and 3-D AVO are accepted practices. The steps that follow will enhance the converted-wave interpretation techniques developed in 2-D and carry the processes of attribute mapping in 3-D in the interpretation of 3-D converted-wave seismic data.

#### 4.4.1 Clastic model interpretation

The P-P and P-S volumes for the clastic model are loaded on the Landmark interpretation system. The event correlations along inline 54 of the P-P volume and the P-S volume are shown in Figures 4.14 and 4.15, respectively. The apparent polarity shift of the Second White Specks event is the result of a  $V_s$  increase rather than a  $V_p$  decrease. The Viking event on the P-P volume shows little lateral variation throughout the data. The P-S Viking event, however, shows distinct character changes because of the increased  $V_s$  contrast between it and the BFS shale. There is also an amplitude reduction in the Mannville reflection below the Viking sand. The position of these anomalies correspond to the location of the sand bodies in the model.

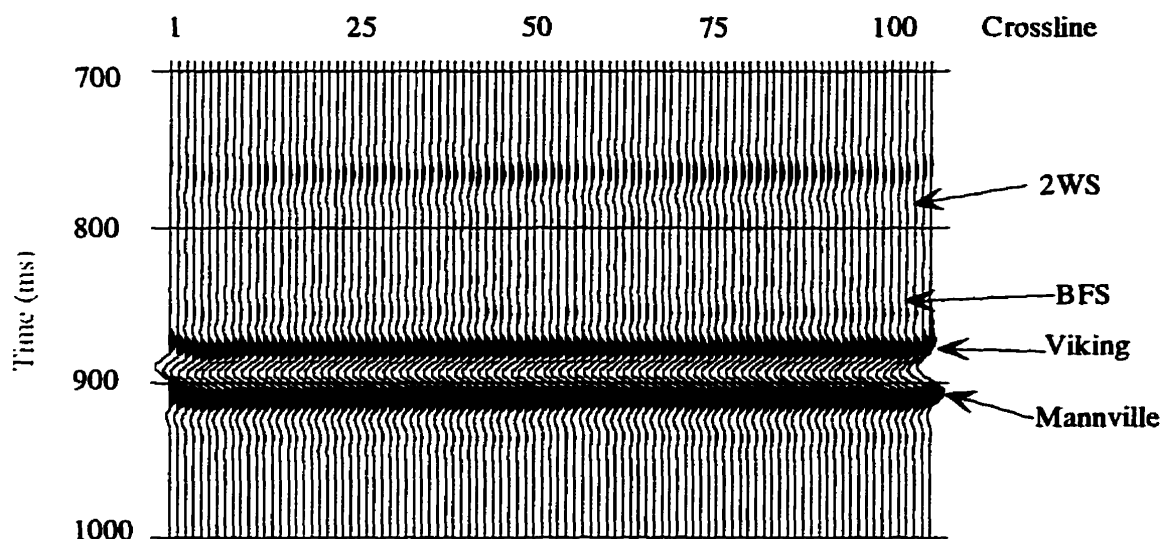


Figure 4.14: Inline 54 of the clastic model: P-S migrated volume.

The  $V_p/V_s$  ratios are calculated using equation (1.1) for the BFS-to-Mannville interval. Since the bin sizes are the same for both data volumes, the  $V_p/V_s$  can be directly calculated for every trace. As a result, the 2-D converted-wave interpretative tool of  $V_p/V_s$  ratio profiling (e.g. Nazar, 1991, Shaffer, 1993, and Miller et al., 1994) can be extended to mapping. The  $V_p/V_s$  map of the BFS to Mannville interval (Figure 4.16) clearly shows a

relative reduction in the  $V_p/V_s$  ratios relative to the surrounding volume. The position of the sand anomaly is further accentuated by the maps of the Viking shear amplitude (Figure 4.17), the Mannville shear amplitude (Figure 4.18). The acoustic Viking amplitude (Figure 4.19) is very subtle, but when backed by the P-S interpretive products, the position and identification of the sand bodies become more robust.

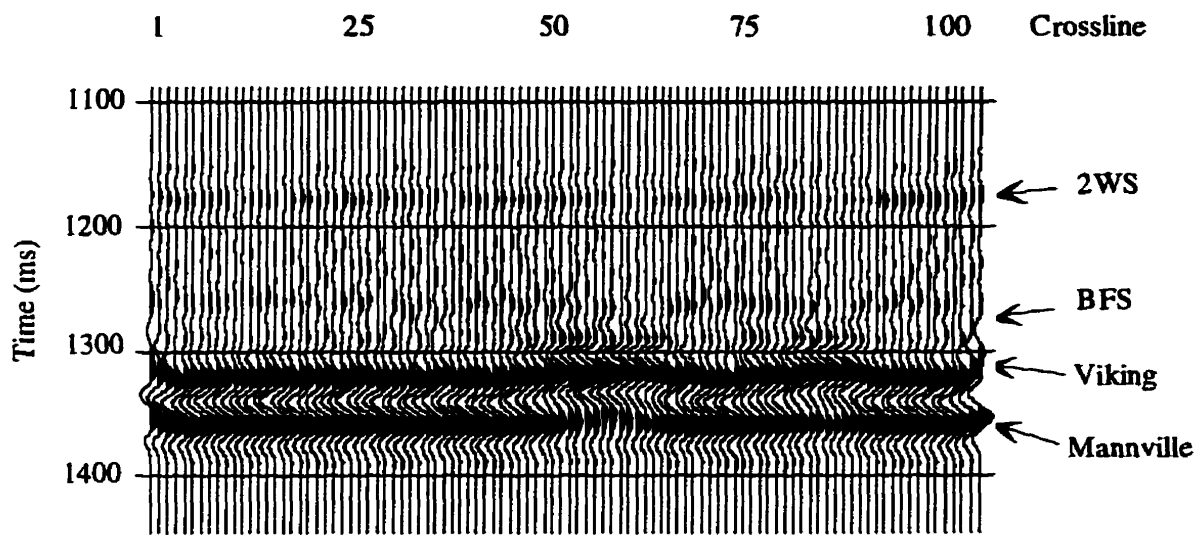


Figure 4.15: Inline 54 of the clastic model: P-S migrated volume.

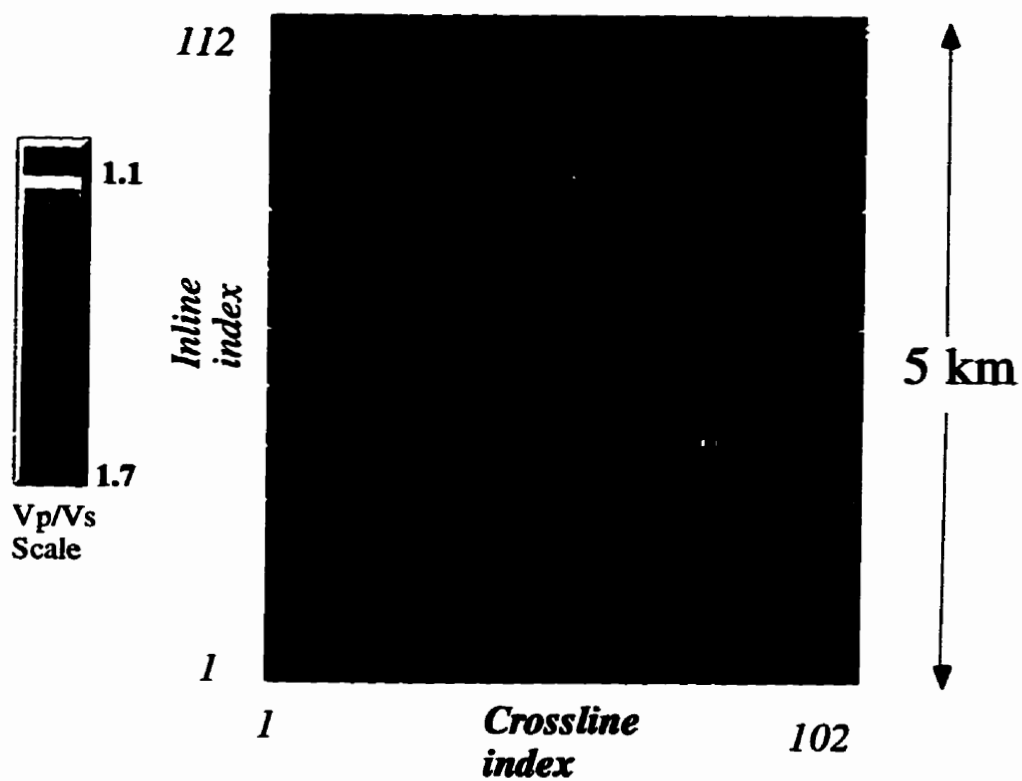


Figure 4.16: Vp/Vs map: Clastic model. Base of Fish Scales to Mannville interval.

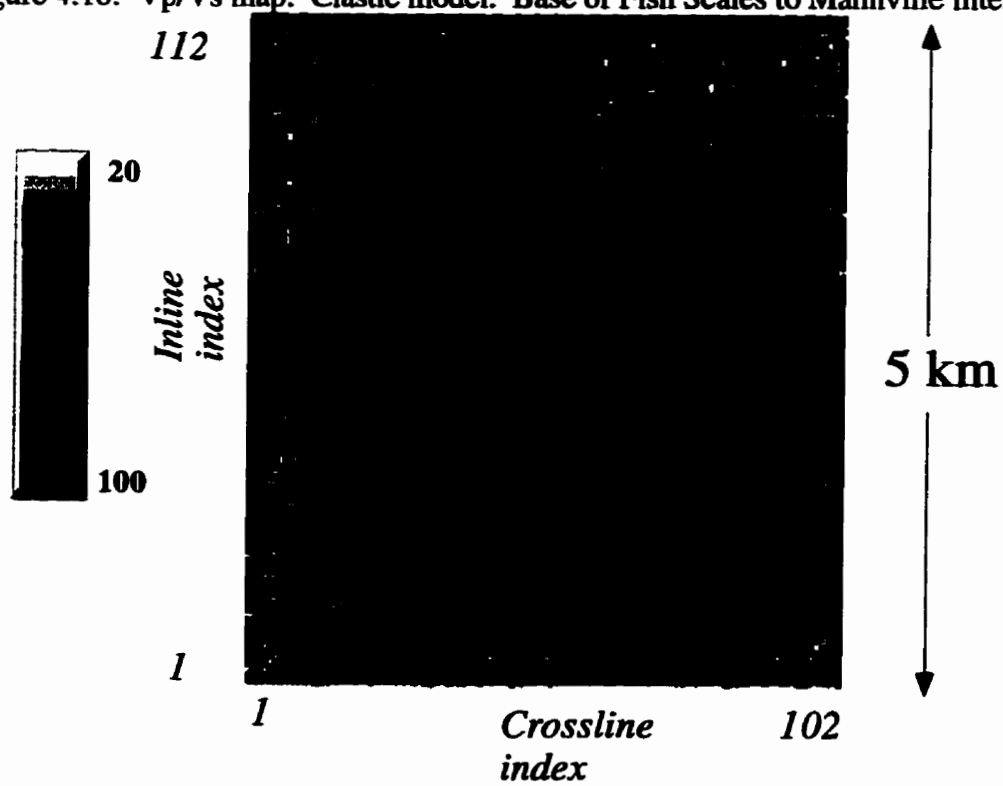


Figure 4.17: Viking shear amplitude map: Clastic model.

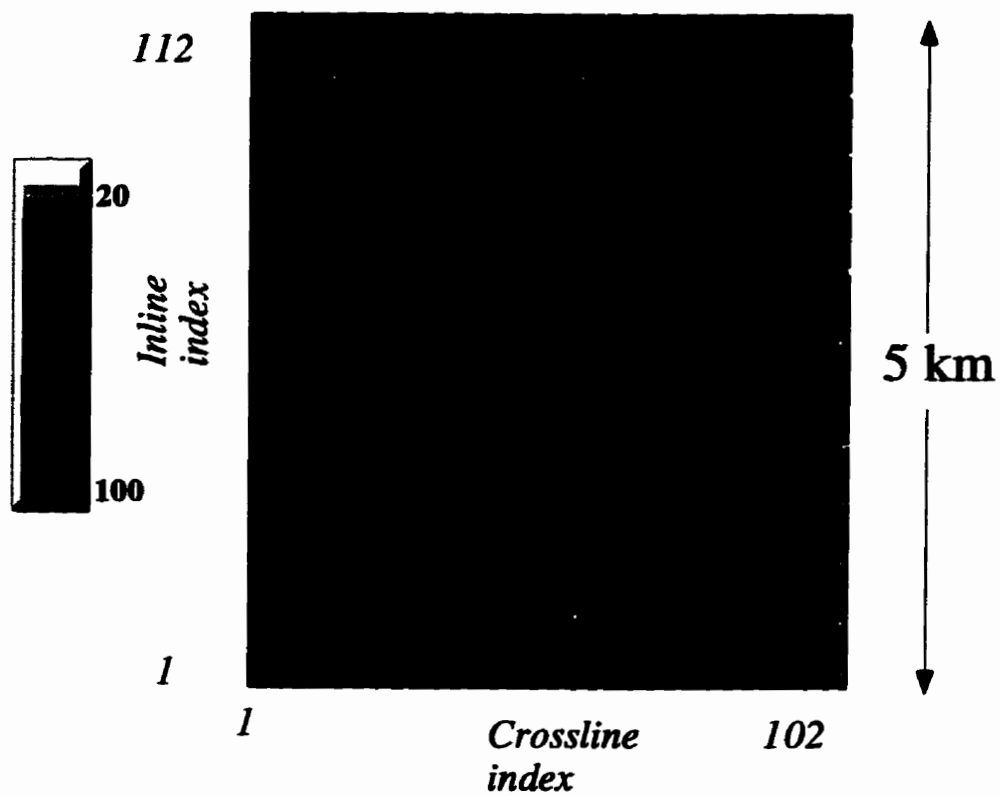


Figure 4.18: Mannville shear amplitude map: Clastic model.

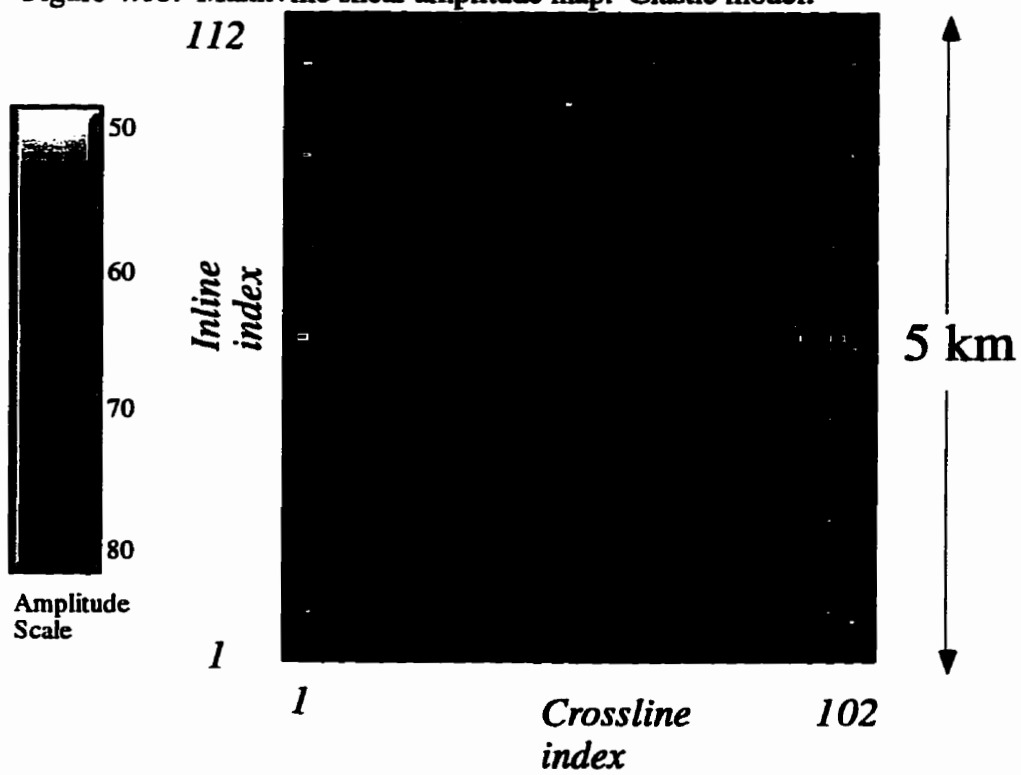


Figure 4.19: Viking P-P amplitude map: Clastic model.

In this example, the inclusion of P-S waves to image the Viking sand has proven to be very valuable. The exclusive use of P-waves is not capable of unambiguously imaging the sand bodies. Detection of small changes in  $V_p/V_s$  in a map view with the power of 3-D pattern recognition can reveal subtler changes than a 2-D profile. The inclusion of shear data volumes for this isotropic model has doubled the amount of interpretable data and has enhanced the interpretation and has made it more robust.

#### **4.4.2 Carbonate model interpretation**

The Landmark Seisworks® interpretation system is used to pick three horizons on the P-P and the P-S volumes of the carbonate model. The event correlations of Inline 44 for the P-P and P-S migrated volumes are shown in Figures 4.20 and 4.21, respectively. The higher frequency P-P data resolves the porosity base of the reef. The reef-to-basin transition is found at the disappearance of the lower porosity peak and its replacement by a weaker peak, which defines the top of the calcareous basin fill. The base of porosity and the top of the basin fill is combined into one horizon pick (the 'carbonate'). The map of the P-P amplitude of the carbonate marker (Figure 4.22) defines the reef edge at crossline 45. It is also defined by the P-S amplitudes of the carbonate (Figure 4.23) and the Ireton (Figure 4.24).

The shear section has a lower bandwidth, which is anticipated at this depth (Miller et al., 1994). Despite its lower bandwidth, the shear amplitudes of the Nisku and the Ireton also define the reef edge. The P-S interpretation, which supplements the already established P-P interpretation, infers lithology based upon  $V_p/V_s$  ratios calculated between the Wabamun and the Ireton markers (Figure 4.25). The calculated  $V_p/V_s$  values for this interval match the model. Figure 4.25 also reveals a decrease in the  $V_p/V_s$  ratio toward the northwest along the reef flank. This zone marks an increase in porosity due to the porosity wedge of the model. The P-P data clearly images the reef -to- basin transition, but the

inclusion of shear data provides additional lithologic information that otherwise could not have been determined. The P-S information provides a powerful supplement to the acoustic interpretation and further characterizes the anomaly.

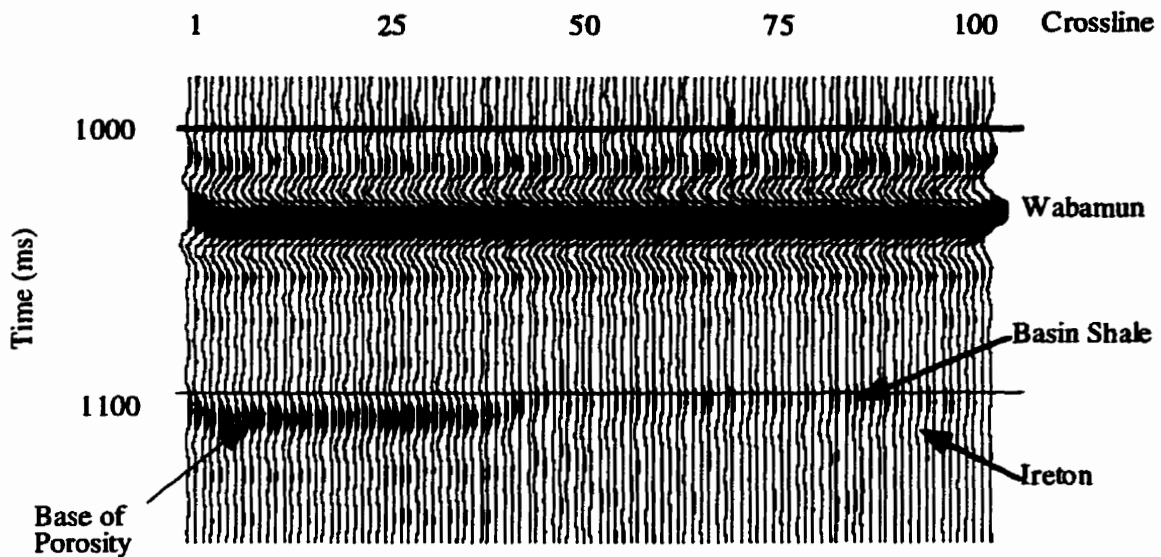


Figure 4.20: Inline 44 of the carbonate model: P-P migrated volume.

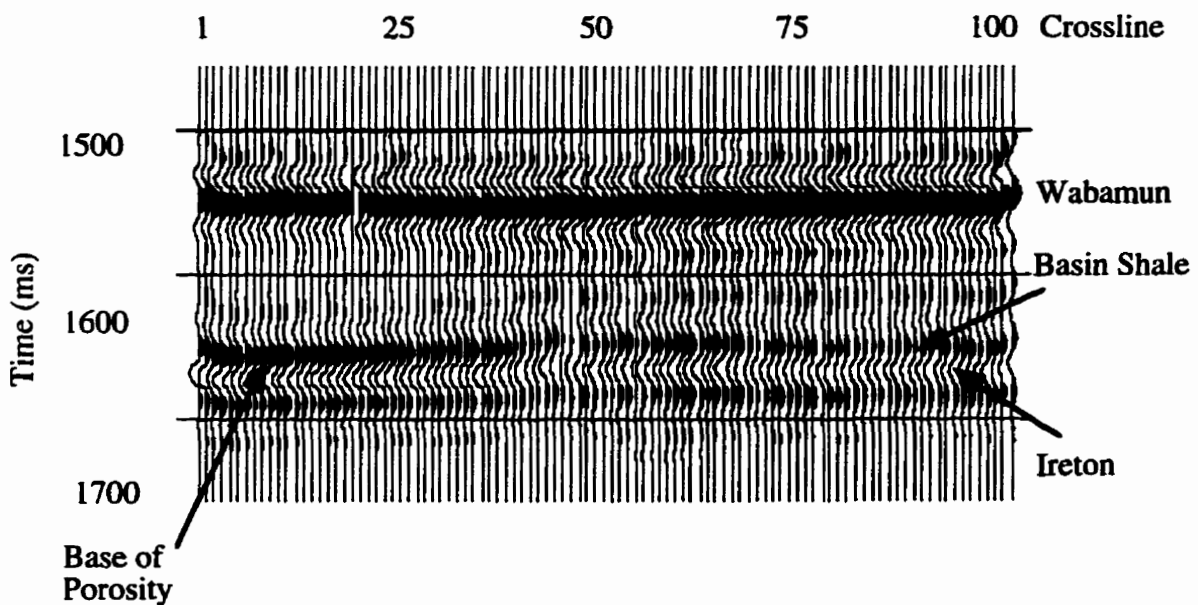


Figure 4.21: Inline 44 of the carbonate model: P-S migrated volume.

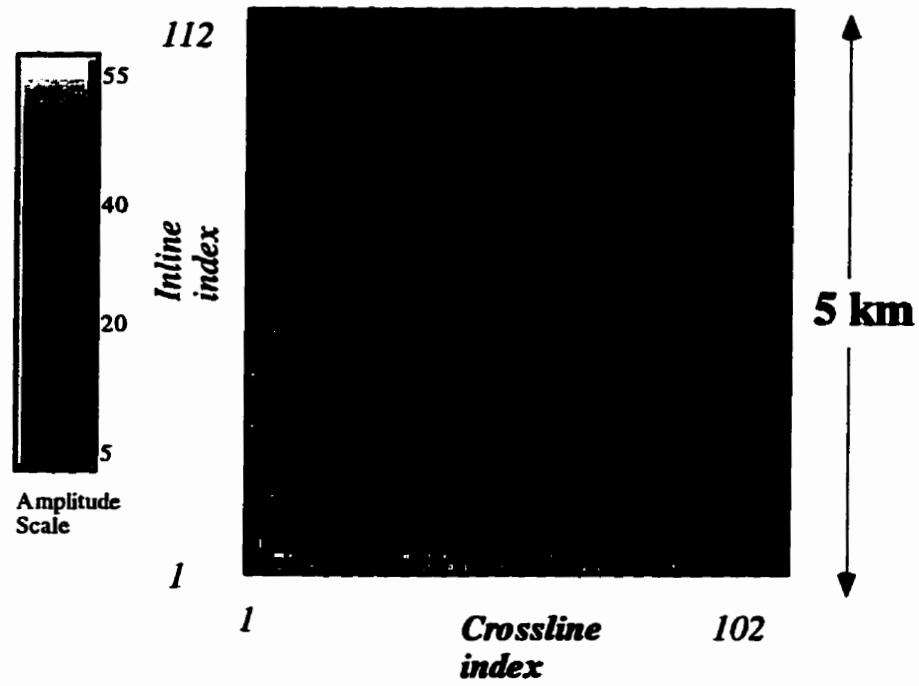


Figure 4.22: P-P carbonate amplitude map. Carbonate model.

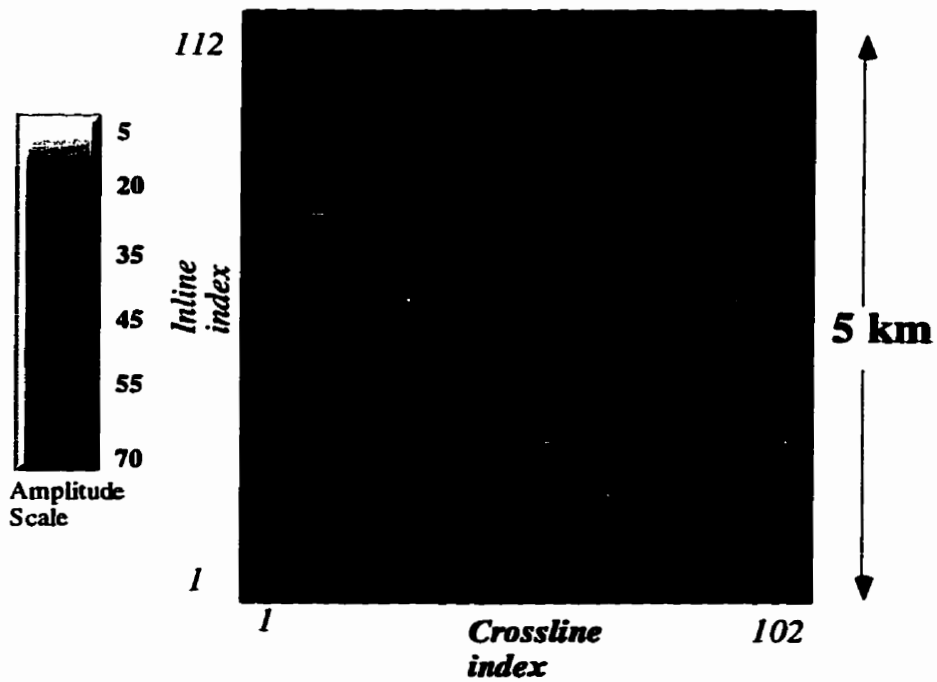


Figure 4.23: P-S carbonate amplitude map. Carbonate model.

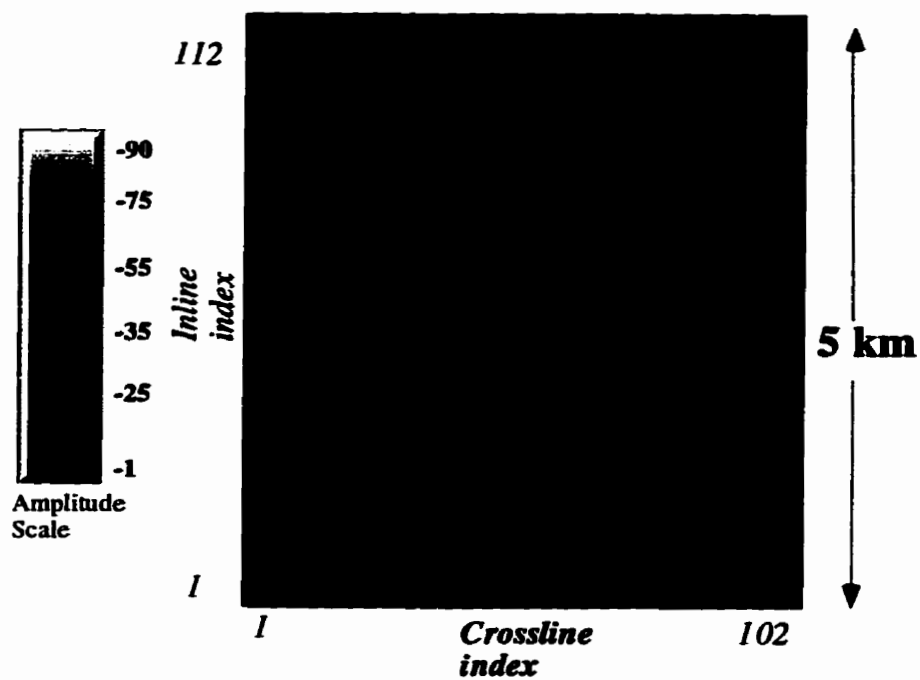


Figure 4.24: P-S Ireton amplitude map. Carbonate model.

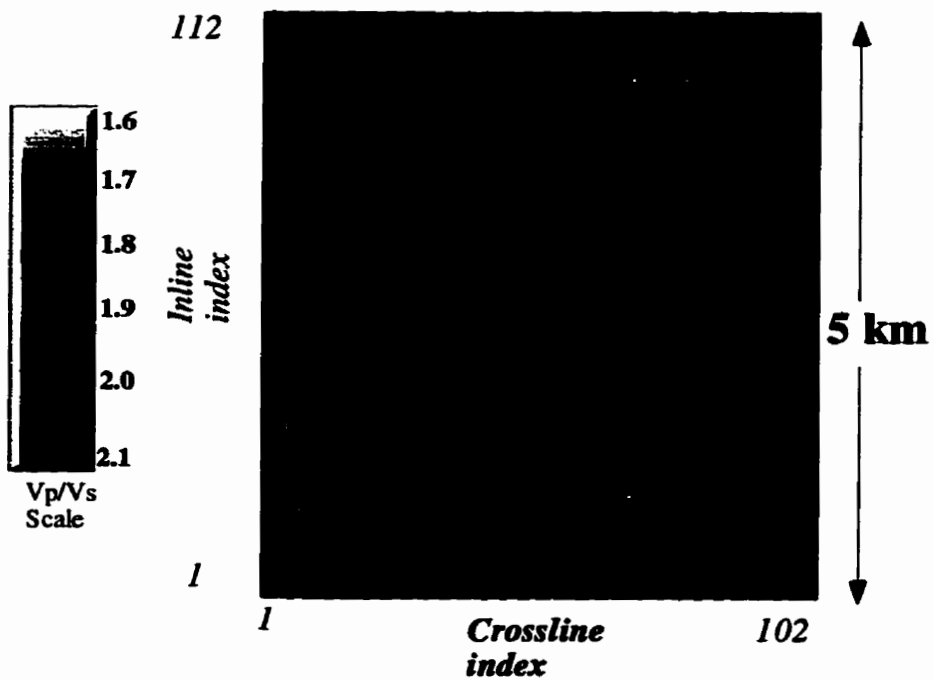


Figure 4.25: Vp/Vs (Wabamun to Ireton interval) map. Carbonate model.

## 4.5 Tuning Effects Upon Vp/Vs Ratio Calculations

The Vp/Vs ratios for the BFS-to-Mannville interval of the clastic model are lower than the expected values. Tuning effects may be the possible cause of this underestimation. The Vp/Vs calculations are based upon the interpreted time structures of the BFS and Mannville, and they may be affected by wavelet tuning within the Joli Fou shale.

A converted-wave 2-D seismic line is acquired over the clastic model in the orientation of cross-section A-A' in Figure 4.1 to test the effect of wavelet tuning upon calculated values of Vp/Vs. The line is acquired with an RI of 100m and SI of 300m. The processing procedures are a 2-D version of the 3-D processing flow described in Chapter 4.3. The P-S data are convolved with a 50 Hertz Ricker wavelet; the P-P data with a 60 Hertz Ricker. The Viking and Mannville horizons are interpreted on the P-P and P-S sections for a series of filtered versions of data. The Vp/Vs values are calculated for the Viking-to-Mannville isochrons along portions of the line where the Viking sand is not present (Figure 4.26). Within this zone is a 50m interval of Viking and Joli Fou shale with an expected Vp/Vs of 2.05.

At 50 Hertz, the P-S section (Figure 4.26) clearly resolves the 30m Viking and the 20m Joli Fou shale. At 60 Hertz, the P-P data (Figure 4.27) does not resolve the Joli Fou shale. For given frequency and velocity, the wavelength is (Sheriff and Geldhart, 1982):

$$\lambda = \frac{V}{F}, \quad (4.4)$$

where F= the dominant frequency

V = the velocity

$\lambda$  = the wavelength.

For a  $V_p/V_s$  ratio of 2:,

$$\lambda_s = \frac{\lambda_p}{2}, \quad (4.5)$$

where  $\lambda_s =$  P-S wavelength

$\lambda_p =$  P-P wavelength.

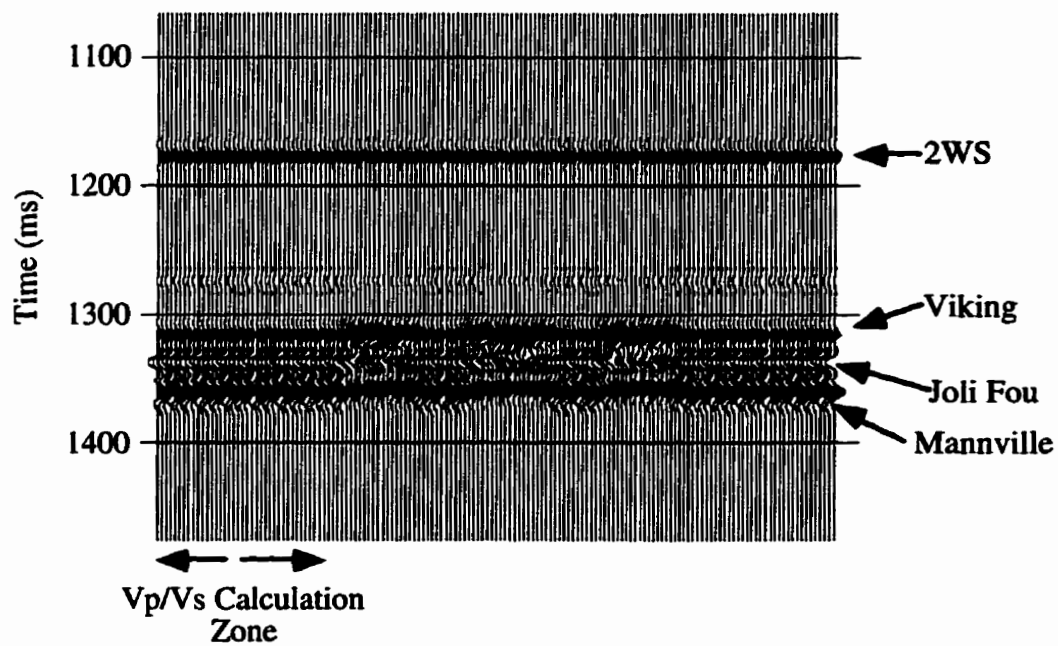


Figure 4.26: 2-D P-S migrated section of the clastic model. Dominant frequency is 50 Hz.

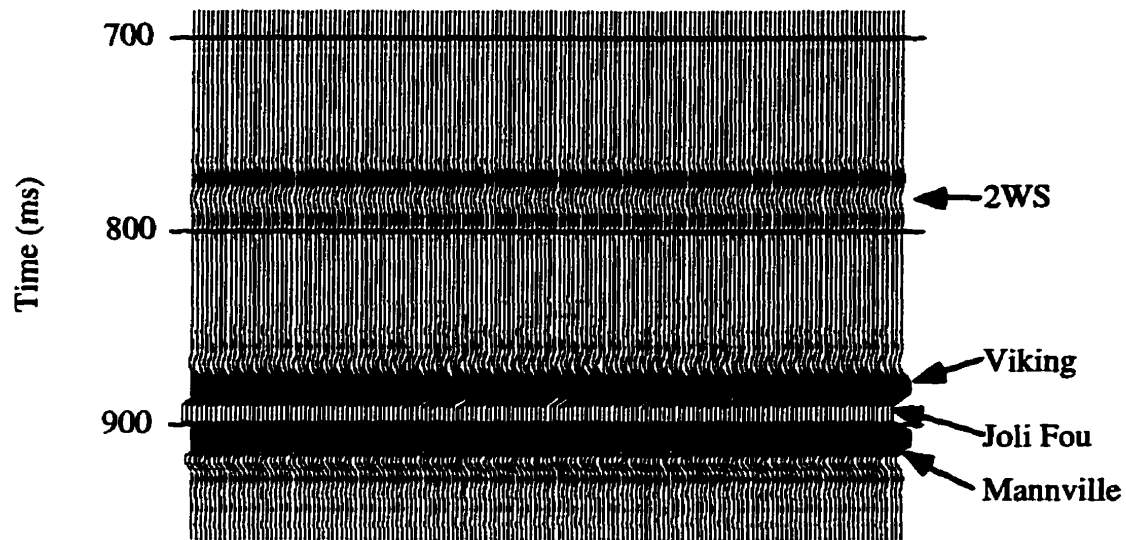


Figure 4.27: 2-D P-P migrated section of the clastic model. Dominant frequency is 60 Hz.

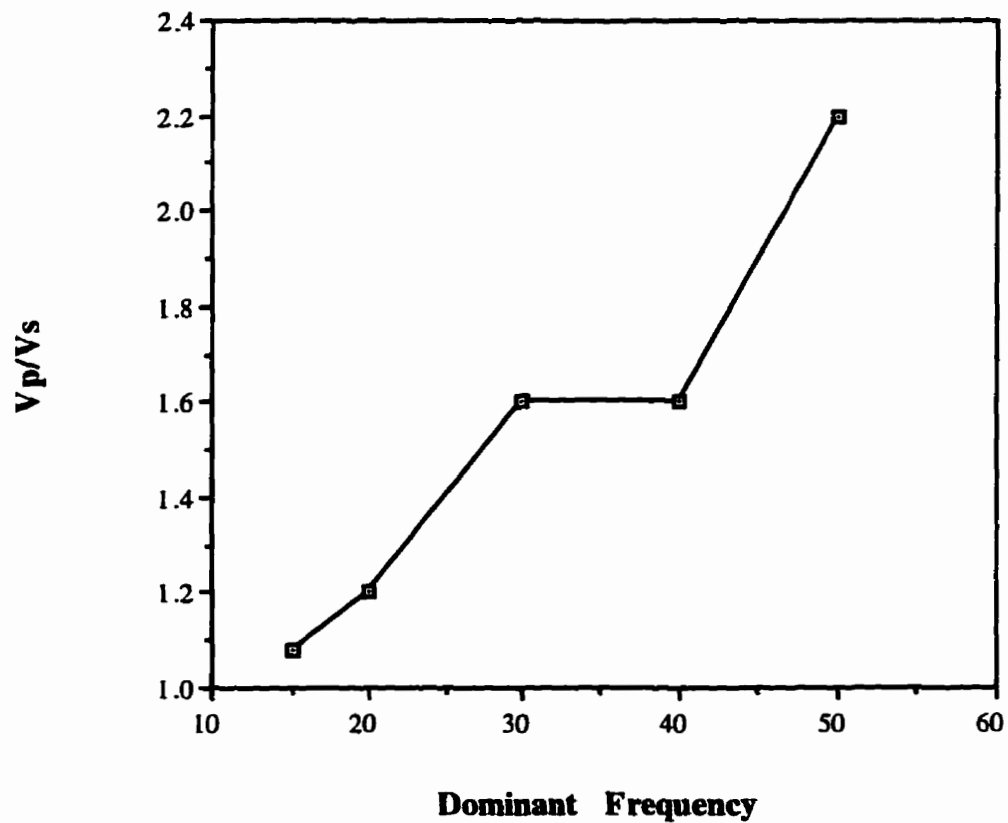
Equation 4.5 shows that the P-S and the P-P data will not have consistent tuning effects for the same dominant frequency. This discrepancy will affect the horizon interpretations from the P-P and P-S datasets and will directly affect the  $V_p/V_s$  ratio calculations.

Table 4.4 summarizes the  $I_p$ ,  $I_s$ , and the calculated  $V_p/V_s$  ratios for increasingly bandlimited data. The  $V_p/V_s$  ratio (Figure 4.28) decreases rapidly as the dominant frequency is reduced: The P-S Viking to Mannville interval ( $I_s$ ) decreases while the P-P interval ( $I_p$ ) value *increases*

. The calculated  $V_p/V_s$  ratio for the Mannville to Viking interval is underestimated for frequencies below 50 Hz. due to wavelet tuning.

<b>Dominant Frequency</b>	<b><math>I_p</math></b>	<b><math>I_s</math></b>	<b><math>V_p/V_s</math></b>
50	27	44	2.20
40	29	38	1.6
30	29	38	1.6
20	35	39	1.2
15	48	50	1.08

**Table 4.4:**  $V_p/V_s$ ,  $I_p$ , and  $I_s$  values for the Viking to Mannville interval for decreasing values of the dominant frequency



**Figure 4.28:**  $V_p/V_s$  versus P-P and P-S section dominant frequency. Clastic numerical model.

Dominant Frequency	$I_p$	$I_s$	$V_p/V_s$
50	29	44	2.03
40	29	38	1.6
30	29	38	1.6
20	29	39	1.7
15	29	50	2.4

**Table 4.5:**  $V_p/V_s$ ,  $I_p$ , and  $I_s$  values for the Viking to Mannville interval for decreasing P-S dominant frequency. P-P dominant frequency = 40 Hz.

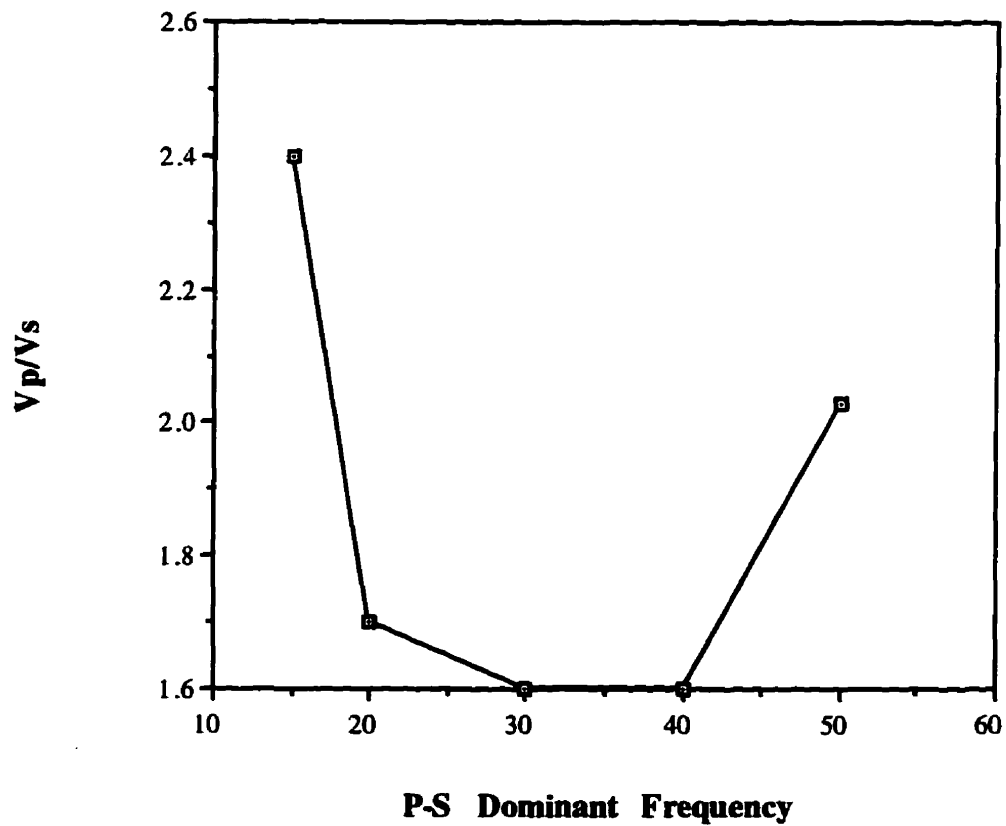


**Figure 4.29:**  $V_p/V_s$  versus P-S frequency. P-P frequency = 40 Hz. Clastic numerical model.

Figure 4.29 displays the calculated  $V_p/V_s$  versus the dominant frequency of the P-S wavelet for a constant P-P frequency of 40 Hz. As the P-S frequency decreases, the  $V_p/V_s$  ratio is underestimated by 20% in the 20 to 40 Hertz range, but is overestimated for very low frequencies. Tatham and McCormack (1991) recommend narrow intervals to calculate  $V_p/V_s$  ratios, but for low frequencies, these calculations may be compromised by tuning. Wavelet effects in  $V_p/V_s$  ratio calculations have been noted by Miller et al. (1994). Wavelet tuning has a serious effect upon the absolute value of the  $V_p/V_s$  ratio, but the relative changes of  $V_p/V_s$  should remain intact, if the wavelet is consistent throughout both datasets.

## 4.7 Chapter Summary

The two isotropic models show that the use of 3-D P-S data provides supplementary information to the acoustic 3-D survey. In the sand model, the P-S data are indispensable in delineating the Viking sands. In the reef model, the P-P data can adequately image the reef-to-basin transition. Comparative time intervals between the P-P and the P-S data result in  $V_p/V_s$  maps that can provide lithologic and thickness indicators. Combining this information in a 3-D measurement with the acoustic survey provides a more detailed interpretation; one which could not be achieved with acoustic data exclusively.

## Chapter 5: Analysis of 3C-3D field data

### 5.1 Introduction

Several 3C-3D surveys have been acquired in North America in the last several years. Lawton (1994) describes the field design for a survey acquired in Texas by Mitchell Energy Corporation. In 1994, Amoco Canada Petroleum Company Limited acquired a survey in central Alberta, while the University of Calgary led a consortium of companies in the acquisition of the Blackfoot 3C-3D survey in October 1995. Yang et al. (1996) conduct an analysis of the Blackfoot 3C-3D. Figure 5.1 displays a  $V_p/V_s$  map centred about the Glauconitic formation. The map clearly shows the position of the channel facies. Also, areas of low  $V_p/V_s$  correlate with the producing wells.

The acquisition of several other 3C-3D surveys are currently in progress in North America. In 1993, a consortium, led by the Colorado School of Mines, acquired a survey near Joffre, Alberta (Al-Bastaki et al., 1994). This field data set provided an opportunity to apply the established 2-D techniques of elastic wave interpretation to the third dimension.

In this chapter, I will extract shear-wave information from the converted (P-S) waves. The P-S information, in turn, is generated from 3-C recording of a P-wave source. From these data, we can map amplitudes, create time slices, construct isochron maps, and map various isochron ratios.

It is thought that an identifiable seismic polarization will result from a consistent stress or fracture orientation throughout the sedimentary column. The two shear polarizations can be processed separately, tripling the amount of interpretable data.

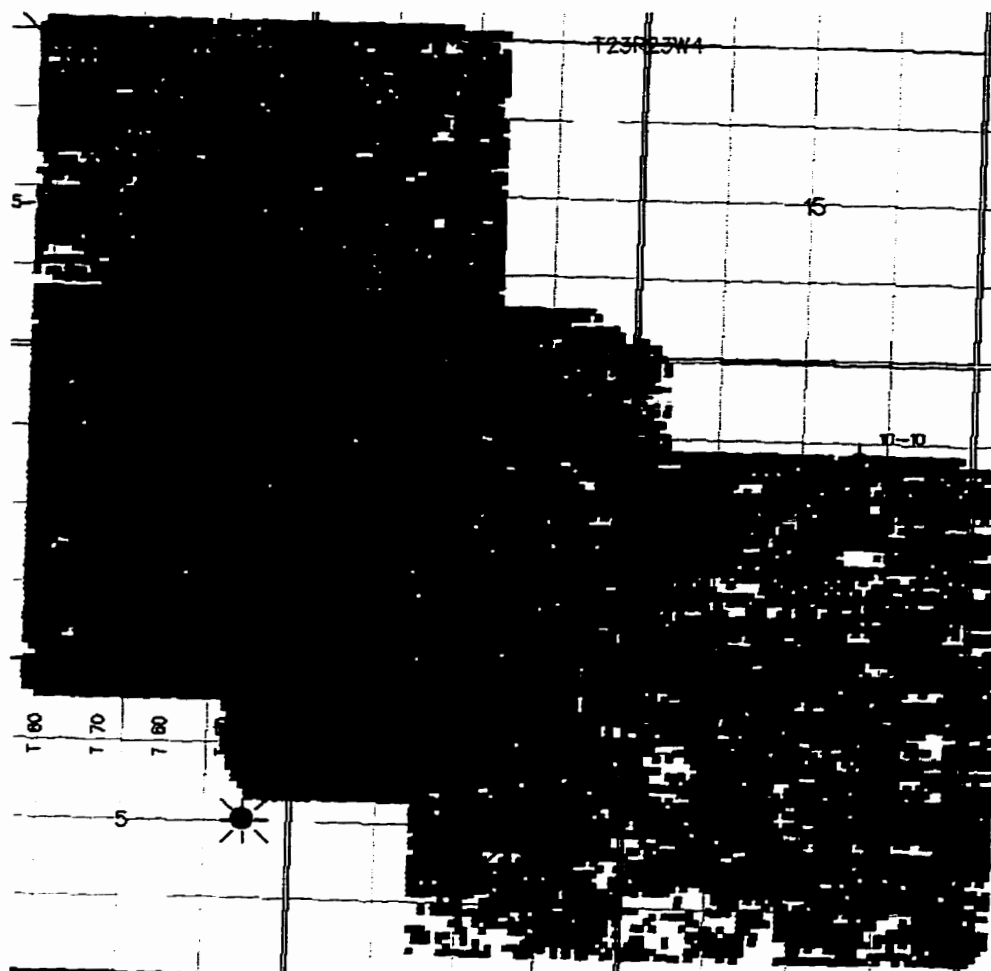


Figure 5.1:  $V_p/V_s$  map centred about the Glauconitic formation: Blackfoot 3C-3D.. The oil wells (solid dark circles) lie within the lower  $V_p/V_s$  values (red and green). From Yang et al. (1996).

The orientation of the fast shear-wave polarization ( $S_1$ ) and the slow shear-wave polarization ( $S_2$ ) can be determined in processing. The variations of the  $S_1$  and  $S_2$  isochrons between horizons can be mapped as well. Their amplitudes have been used in anisotropic studies and fracture detection (Yardley et al., 1991). For instance, Kendall and Kendall (1996) report  $S_2$  amplitude dimming on 2-D multicomponent lines covering a sandstone target in Wyoming which correspond to regions of enhanced gas production.

I will present an interpretation of the Joffre 3C-3D data set that describes two geologic scenarios: The estimation of the presence of sand in the Viking formation, and the detection of fractures within the Second White Speckled Shale.

A 3-D P-S seismic survey acquired in central Alberta has provided a cost-effective mechanism to acquire shear data volumes. Three data sets are interpreted: The conventional pure P-wave data and two anisotropic converted-wave products (the P-S1 and the P-S2). The P-S data are of good quality, although they are somewhat compromised by the survey design. They allow construction of  $V_p/V_s$  and delay-time maps for both the slow and fast shear-wave polarization.

## **5.2 Geological background**

The Viking formation consists of marine-deposited sand and shale sequences that formed a clastic wedge east of the rising Cordillera during Cretaceous time (Reinson et al., 1994). The Viking is a member of the Colorado Group and lies above the Joli Fou shale. It is a prolific producer of oil and gas with the basin.

In the Joffre region, sand thicknesses vary between 15 and 35 metres at a depth of about 1500 metres. A producing Viking oil pool which has produced  $5822 \times 10^3$  of oil, lies 2 miles southwest of the Joffre 3-D P-S survey (Figure 5.2).

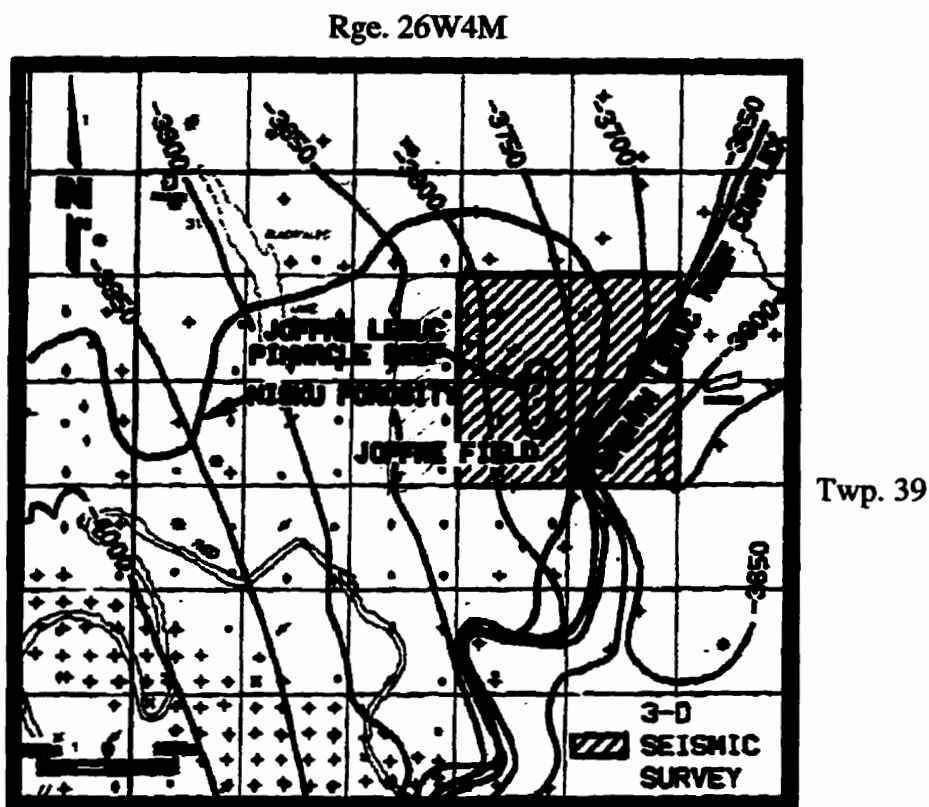


Figure 5.2: Location of the Joffre 3C-3D survey superimposed upon Leduc and Nisku formation outlines. The Joffre Viking field lies 2 miles southwest of the survey.

The Second White Speckled Shale is basin-wide marker on log and seismic data. The shale was formed at the end of a major transgression (relative sea level rise) in the Cretaceous. (Leckie et al, 1994). Because of its high organic content, it is both a source and reservoir of hydrocarbons. Oil has been produced in the shale within zones of intense vertical fracturing brought about by the in situ stress field of the Rocky Mountains.

The fracture presence is the key criterion for economic production. The detection of vertical fractures and the measurement of transverse isotropy (due to the finely layered shales) have been investigated by Goodaway and Mayo (1994), and Stewart et al. (1993).

The Second White Speckled Shale resides about 1400m below the Joffre survey. There is no production of oil within the shale in this area.

### **5.3 Acquisition and processing**

The parameters of the survey are detailed in Table 1. Solid State Geophysical Ltd. acquired the data for the Colorado School of Mines over a 13.6 km<sup>2</sup> area in April of 1993. Acquisition comprised of 4 live receiver patches consisting of 6 lines each. Each patch contained 324 3-component receivers resulting in a 972 channel live recording. The source was a single vibrator that used a 12-second linear up-sweep, repeated 7 times, between 10 and 120 Hertz. The receivers were 3-component OYO SMC-3-D geophones. No surface arrays (shot or receiver) were used to attenuate ground roll or the air blast.

The source line orientation is at a 45 degree angle to the receiver lines (Figure 5.3). The survey was designed primarily for a pure-P and pure-S survey. The design ensured a smooth fold (Figure 5.4) , azimuth, and offset distribution, but it did not mitigate any fold periodicity that occurs with P-S acquisition. The design, as we shall see, was not optimal for converted-waves.

<p><b>Survey Size:</b> 3240m (N-S) x 4200 m (E-W)  <b>Source Points:</b> 742  <b>Receiver Stations:</b> 810  <b>Receiver Lines:</b> 15  <b>Number of Patches:</b> 4  <b>Total Bins:</b> 15 650  <b>Bin Size:</b> 30m x 30m</p>
<p><b>Receiver Patch</b>  <b>Size:</b> 3240m (N-S) x 1500m (E-W)  <b>Receiver Lines (N-S)</b>  <b>Number:</b> 6  <b>Line Spacing:</b> 300m  <b>Receivers/Line:</b> 54  <b>Receiver Spacing:</b> 60m</p>
<p><b>Source</b>  1 Vibrator/Source Point  <b>Sweep Length:</b> 12 Seconds - Linear  <b>Frequency Range:</b> 10-120 Hz - Up Sweep  <b>Number of Sweeps :</b> 7  <b>Listen Time:</b> 4 Seconds  <b>Source Points/Patch:</b> 159 to 212  <b>Source Lines (E-W)</b>  <b>Line Spacing:</b> 60m  <b>Source Spacing:</b> 300m</p>
<p><b>Instrumentation</b>  I/O System 2  <b>Sample Rate:</b> 2ms  3-Component geophones:  OYO SHC-3-D 10Hz.</p>

**Table 5.1: Survey Design Parameters: Joffre Survey**

(Modified from Colorado School of Mines, 1992)

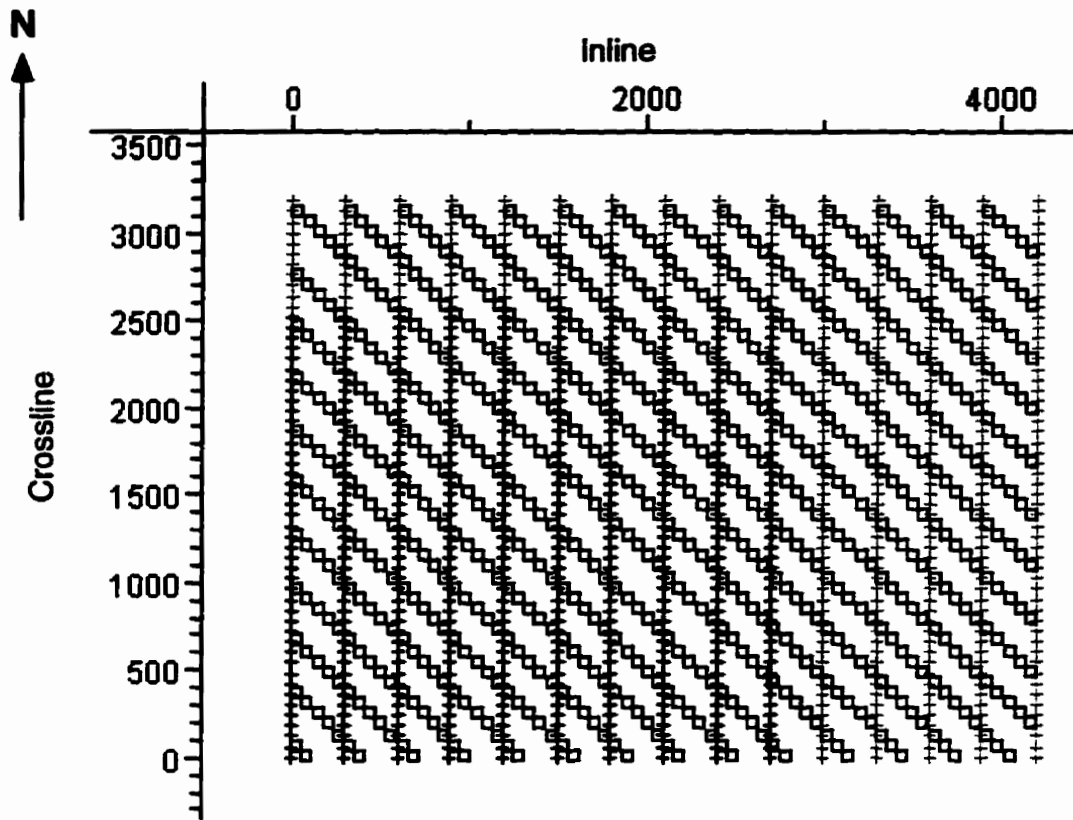


Figure 5.3.: Survey grid of the Joffre multicomponent survey. The source lines run at a 45 degree angle to the north-south receiver lines. Units are in metres.

Complications arise in the common-conversion point (CCP) domain for P-S ray paths (Eaton and Lawton, 1992). As discussed in Chapter 3, designing a converted-wave survey becomes complicated because the ray paths between source and receiver are not symmetrical. Designs that do not incorporate the positional variance of the CCP bin can have unpredictable fold patterns. Short wavelength fold variations and fold gaps are detrimental to robust post-stack and pre-stack amplitude mapping (Lawton, 1993).

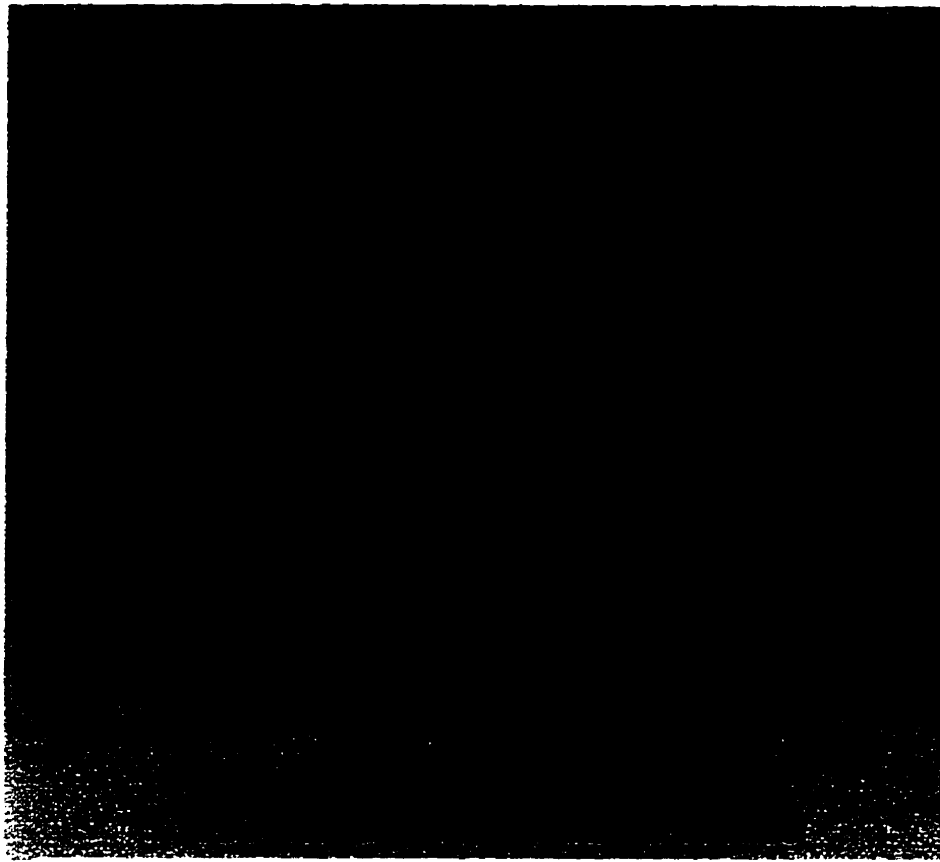


Figure 5.4: CMP fold of the Joffre 3-D multicomponent survey. From Lawton, 1993.

Gaps in CCP fold distribution will occur if CCP binning is not taken into account in the acquisition design: The Joffre survey was not designed for converted-waves. The converted-wave optimized asymptotic bin map is shown in Figure 5.5. There are two linear gaps of zero fold coupled with highly periodic fold variation in the east-west direction. These gaps complicate the processing and interpretation of the converted-wave data.

The data were processed by Pulsonic Geophysical Ltd. of Calgary. The flows for the pure-P and the converted-wave data sets are shown in Figures 5.6 and 5.7, respectively. The P-P survey was processed with standard 3-D processes (Chapter 4). The details of the converted-wave processing can be found in Chapter 2 and in Cary (1994a).

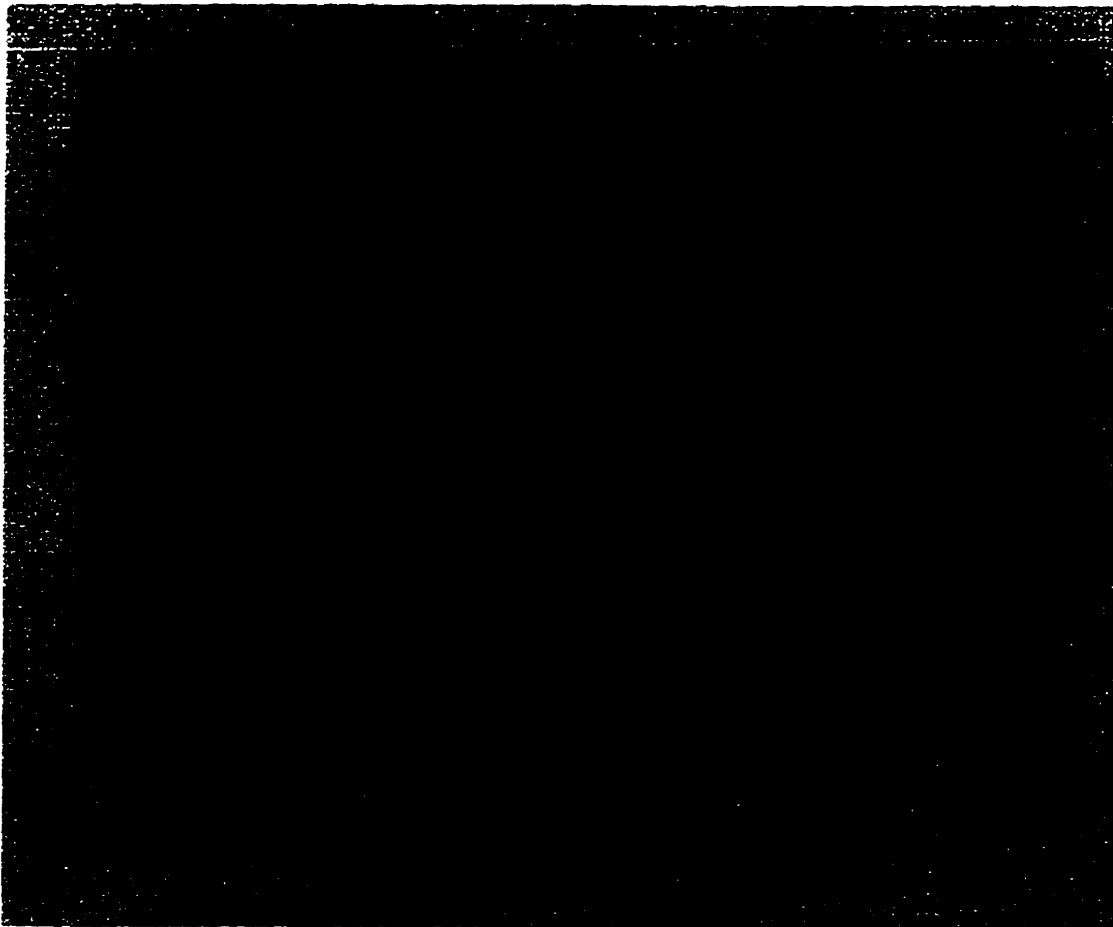


Figure 5.5: CCP optimized fold of the Joffre 3-D multicomponent survey. Note the fold gaps and the high periodicity of the fold in the east-west direction. From Lawton, 1993.

The data were recorded in the inline and crossline components in the field. The data were combined and rotated in the manner described by Lane (1994). Another rotation, based upon the cross-correlation modelling of Harrison (1992), separates the data into fast (S1) and the slow (S2) polarizations. The azimuth of the natural coordinate system (the S1 and S2 polarizations) was found to be 45 degrees east of north. Each volume was then processed separately.

The key step in the processing flow was in the smoothing of the CCP fold gaps in an attempt to even out the periodicity of the fold. Details the CCP smoothing can be found in Cary (1994b). The volumes were asymptotically binned at  $V_p/V_s$  ratio of 2.

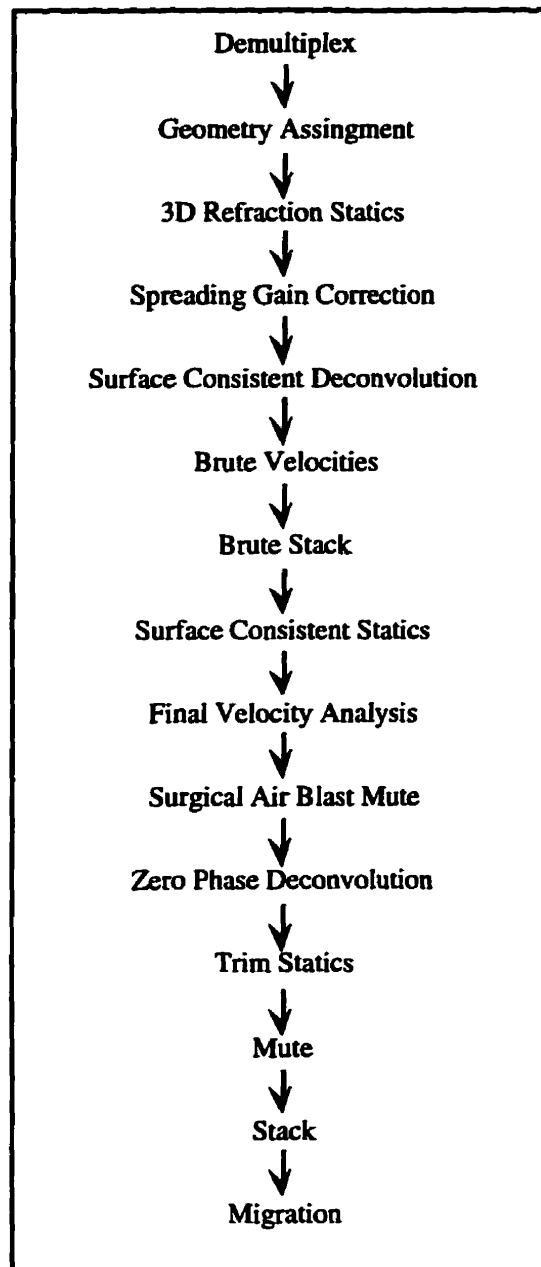


Figure 5.6: 3-D P-P processing flow (Cary, 1994a).

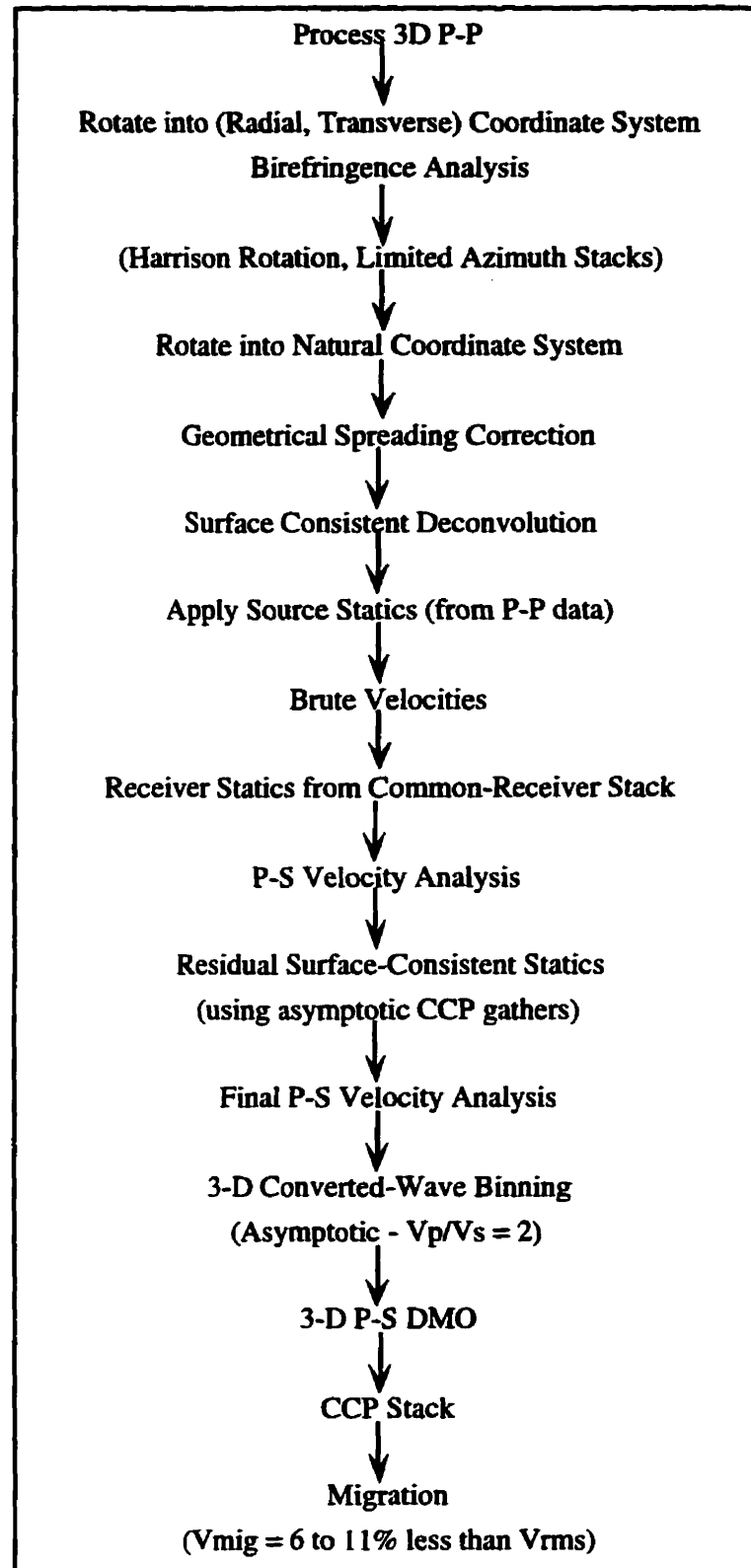


Figure 5.7: 3-D P-S processing flow. (Cary, 1994a).

## 5.4 Interpretation Techniques

Acquiring and processing a multicomponent 3-D data set results in three data volumes: The conventional P-P, the P-S1, and the P-S2 (Larson and Stewart, 1994, 1995). The conventional P-wave 3-D provides spatial delineation of events whereas the shear sections can give lithologic and bulk rock fabric information (Arestad et al., 1995).

The interpretation used the migrated products provided by Pulsonic Geophysical Ltd. of Calgary. Each data set consisted of 141 inlines and 107 crosslines at a 30m bin spacing. Two seconds (at 2ms sample rate) of the P-wave data and 3.5 seconds (at 4ms sample rate) of the S1 and S2 data were loaded onto the Landmark interpretation system. The inline and crossline geometry is shown in Figure 5.8.

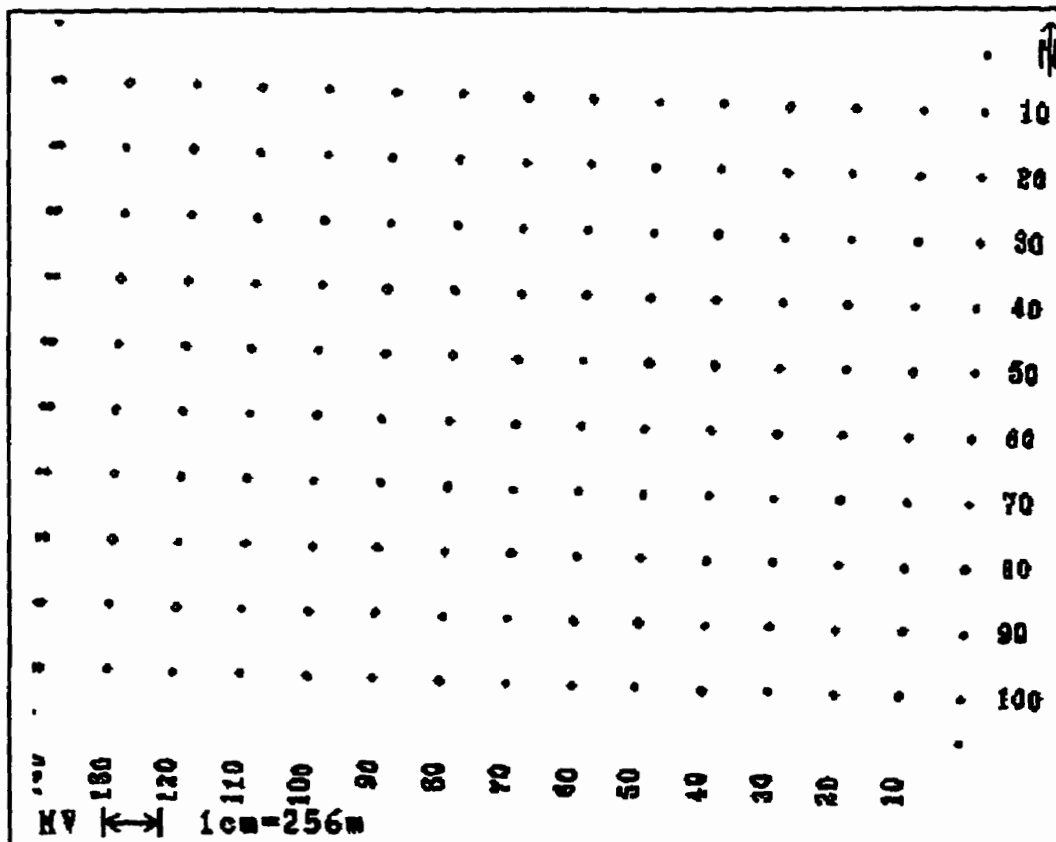


Figure 5.8: Geometry of the 3-D data. There are 107 crosslines (east-west direction) and 141 inlines (north-south direction).

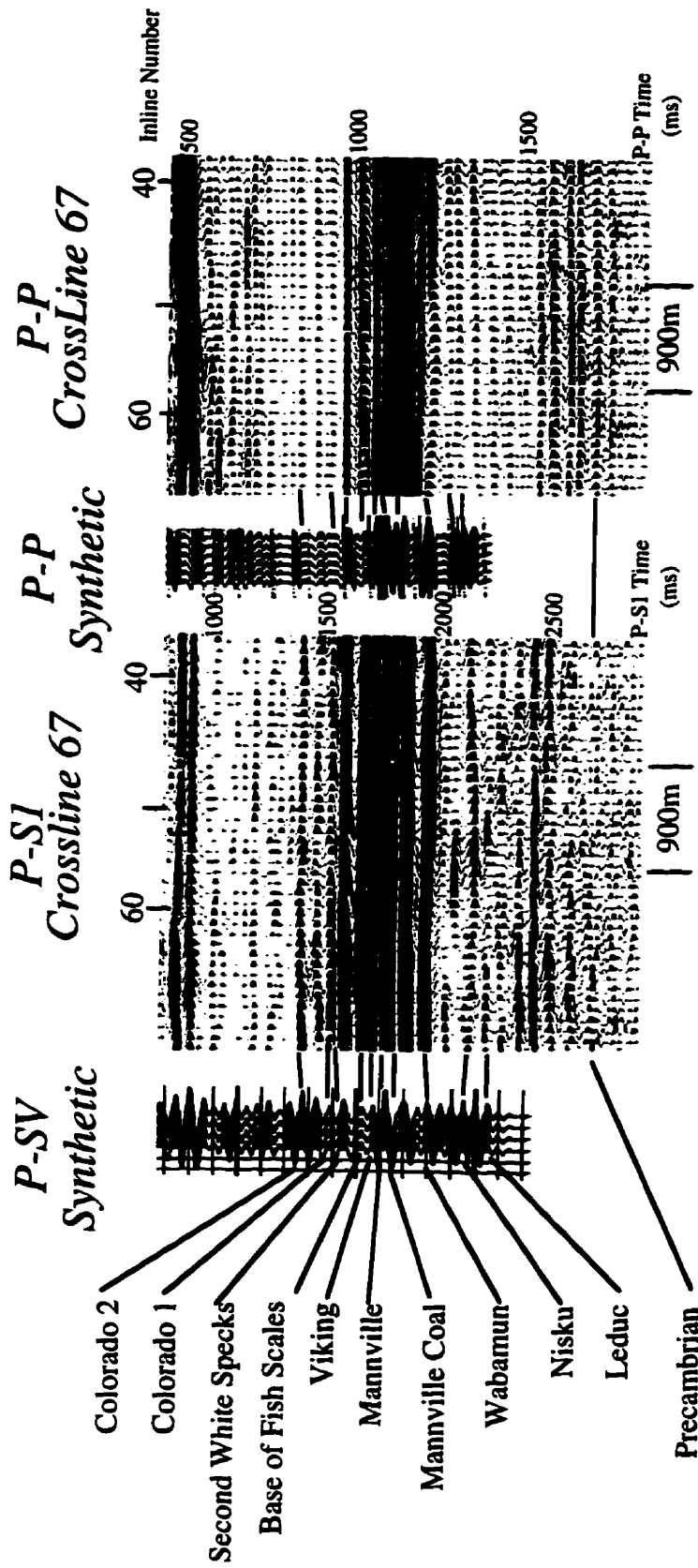


Figure 5.9: Event correlation of Crossline 67 between P-P and P-SI. The time scale of the P-P section has been expanded by 1.5 times to match the scale of the P-SV section.

Figure 5.9 displays the correlation of the P and P-S1 sections along Crossline 67 of the P-P and P-S synthetic seismograms. The scale of the P-wave section and P-P synthetic was expanded by 1.5 to facilitate the correlation to the P-S1 section. A tie between Crossline 70 and Inline 40 of the S1 and S2, respectively (Figure 5.10), shows a small mistie between S1 and S2. A mistie of this nature has been documented by Mueller (1991) in sediments above the Austin Chalk in Texas. It can be caused by shear-wave splitting due to a consistent stress field throughout the sedimentary column.

From Figure 5.10, the S1 volume is of superior quality to the S2. The S1 data provide better continuity of events with higher amplitude and allows easier interpretation. Both shear volumes, are noisier than the P-volume. They are also of narrower bandwidth. The reduced resolution in the shear sections has not resolved the top of the Mannville or the Banff, but the other reflectors above the Wabamun are adequately imaged. The units below the Wabamun are not imaged very well, in the P-P and shear volumes, probably because the Mannville coal in the Cretaceous section has attenuated the reflection energy below it. The attenuation of the reflectors below the Mannville coal is confirmed in the zero-offset VSP of 11-22-39-26W4 (Sun and Stewar, 1994). Despite this attenuation, the converted wave sections have imaged to the Precambrian.

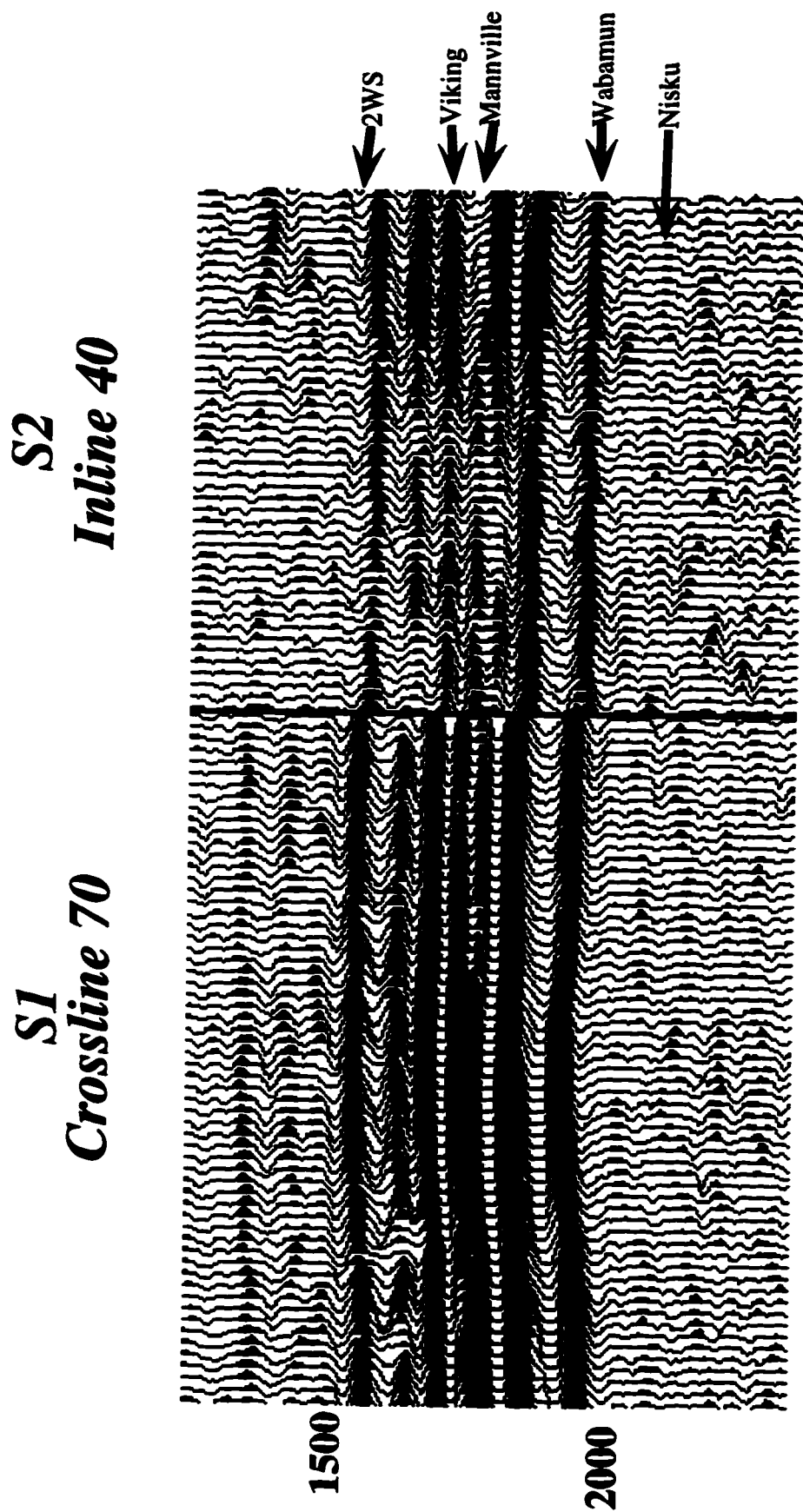


Figure 5.10: Tie between Crossline 70 (S1) and Inline 40 (S2).

The amplitudes of the S1 amplitudes in the Crossline display of Figure 5.10 vary periodically along it, giving the section a mottled appearance. Figure 5.11 displays in map view the amplitude of an S1 event one cycle below the Second White Speckled Shale. The amplitudes are periodic in the crossline direction and mimic the fold periodicity of the acquisition (Figure 5.5), clearly showing that the amplitudes of the converted shear volumes have been compromised by the survey design. This severe acquisition "footprint" has prevented any detailed shear amplitude analysis in this study.

One of the key interpretive tools is the calculation of the ratio between the velocity of the P-wave versus the velocity of the S-wave (the  $V_p/V_s$  ratio). By picking time events, we can find low-resolution but robust lithology indicators. Both the conventional and converted-wave sections equally respond to structural changes in the subsurface.

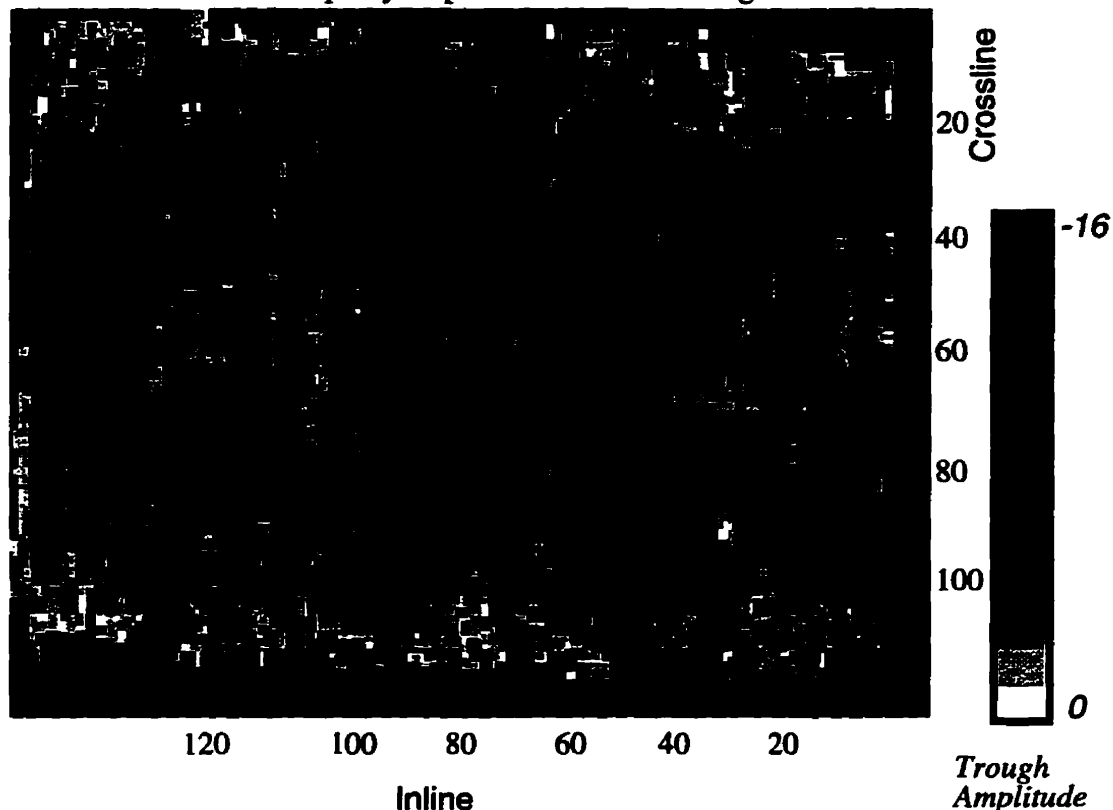


Figure 5.11: S1 amplitude map of the Second White Speckled Shale. The striped pattern reveals a distinct acquisition footprint.

Apparent time interval differences between the P, S1 and S2 can be related to changes in the bulk properties of the rocks within the interval. If the variables of the bulk properties can be constrained, then we can make lithologic, porosity, or fracture density inferences. Sensitivities of  $V_p/V_s$  ratios to gas saturation, lithology, porosity, and fracturing within a time interval are exploited in this technique (Tatham and McCormack, 1991). By using other sources of information, changes in the  $V_p/V_s$  ratio may be related to one variable, and interpretations based on it can be made. For converted waves, the  $V_p/V_s$  ratio can be calculated from stacked data sets of P-P and P-S in the following equation:

$$\frac{V_p}{V_s} = \frac{2 I_s}{I_p} - 1, \quad (5.1)$$

where  $V_p$  = p-wave velocity

$V_s$  = s-wave velocity

$I_s$  = time interval between two P-S reflections

$I_p$  = time interval between two P-P reflections

(Harrison, 1992).

For 3-D data, we can calculate two ratios:  $V_p/V_{s1}$  and  $V_p/V_{s2}$ . Time slices of the S2 volume and the P-wave volume (Figure 5.12) indicate that the converted-shear and the acoustic data are responding to the same structures. In this case, the drape of the Banff and Mannville coal over the Leduc pinnacle in the centre of the survey and the Leduc shelf complex in the south east are illustrated. The ratios calculated between key events can be mapped in plan view and can be related to changes within the intervals of rock fabric, lithology, porosity, clay content, and /or fluid content.

Patterns of  $V_p/V_s$  ratios can now be mapped. The calculation of the  $V_p/V_s$  ratio is a simple by-product of interpreting the P-P and the converted-wave volumes together.

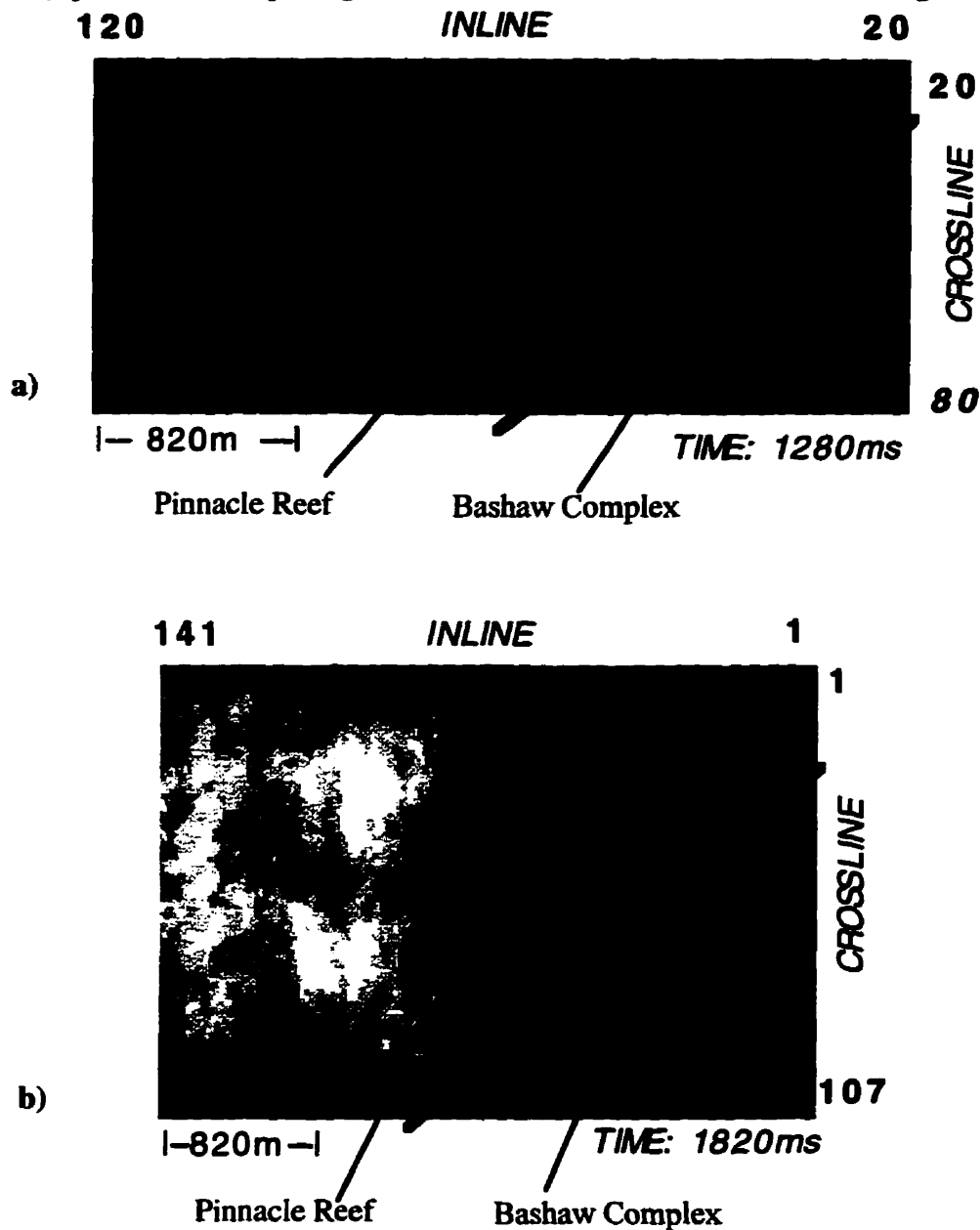


Figure 5.12: Time slices of P-P (a) and P-S (b) at times 1280 and 1820ms, respectively. The Leduc pinnacle is located in the centre of both slices. The Bashaw complex is seen in the lower right corner.

The  $V_p/V_s$  ratio also identifies miscorrelations between data volumes while interpreting.  $V_p/V_s$  ratios can be easily calculated on the Landmark workstation during the

interpretation, and incorrect picks can be found quickly by keeping the ratio within a geologically reasonable value. The time difference or delay between the S1 and S2 volumes for individual horizons are calculated and mapped to infer stress field patterns within the strata.

The differences are calculated between each correlative horizon from their respective volume (Figure 5.13). For instance, the time delay map for the Mannville Coal (Figure 5.17a) is the mistie between the Mannville S1 horizon and the Mannville S2 horizon. Mueller (1991) noted an increasing mistie with depth between S1 and S2 versions of a 2-D line. In 3-D, this phenomenon can be *mapped* for each horizon, and the mistie pattern can be observed for deeper events throughout the 3-D volume.

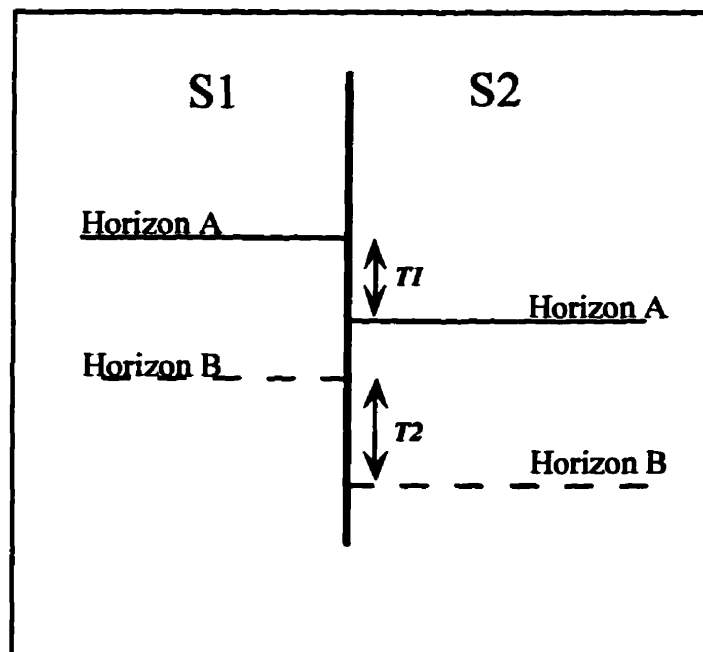


Figure 5.13: Delay time mistie calculation for horizons A and B between the S1 and S2 volumes. In a 3-D volume, the misties for each horizon ( $T1$  and  $T2$ ) are mapped throughout the entire survey.

## 5.5 Results

Figures 5.14 to 5.18 display time-delay maps of selected time structure horizons between S1 and S2 from the Cretaceous to the Devonian. The time delay increases with time until the Wabamun level, where there is a slight decrease. At the Nisku level, the delay-time pattern has changed. This may indicate a continuous stress regime from the surface to the base of the Mesozoic. Also, a consistent pattern of time delay overprints each map, possibly implying a local stress pattern within the Mesozoic. In processing, the S1 and S2 rotation analysis revealed a natural coordinate axes at 45 degrees east of north. The rotation analysis was completed in a zone over the Mannville section (the dominant reflections at about 1.7 seconds - see Figure 5.10) averaged throughout the entire dataset. The average 45 degree natural coordinate system agrees with the results of maximum horizontal stress measured in the wellbores of Alberta by Babcock (1978). Figures 5.14 to 5.18 could possibly be explained by a stress regime that has a local overprint over the 45 degree average.

Figure 5.19 and 5.20 display  $V_p/V_{s1}$  and  $V_p/V_{s2}$  ratio maps for the Viking formation calculated from two different intervals. The narrower interval, between the Base of Fish Scales and Mannville, reveal two distinct regions of lower  $V_p/V_s$  ratios for both S1 and S2. This could be indicative of higher sand content within the Viking interval. The pattern of a lower  $V_p/V_s$  anomaly is seen again for the wider interval within Figures 5.19 and 5.20 (between the Base of Fish Scales and a marker in the Colorado Group). The anomaly is now more diffuse and the  $V_p/V_s$  values are weighted toward sand values because more sand section is included in the calculation. The redundancy of measurement confirms the robustness of the anomaly.

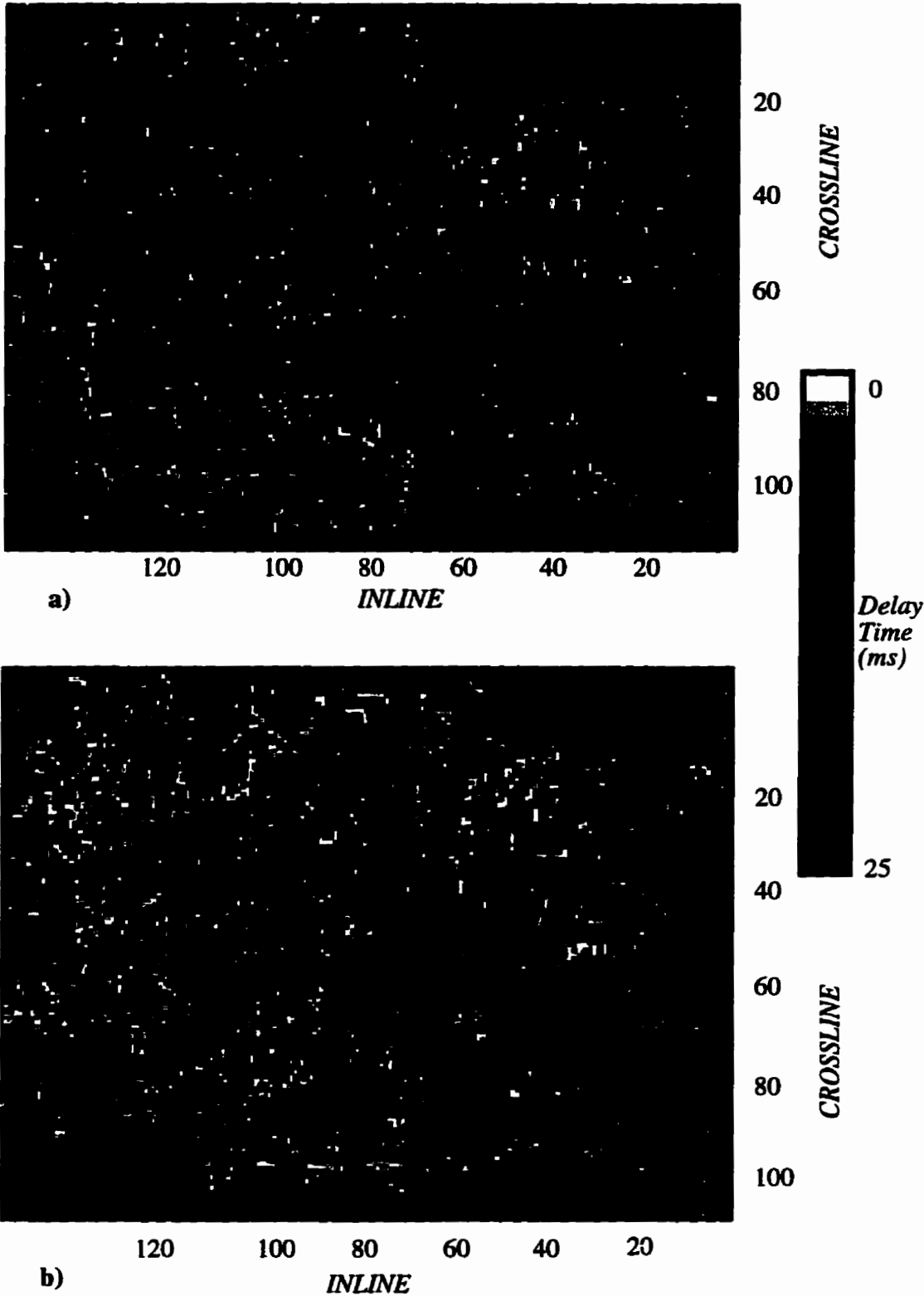


Figure 5.14: Time delay maps between the S1 and S2 data volumes for the Colorado event 2 (a) and the Colorado event 1 (b).

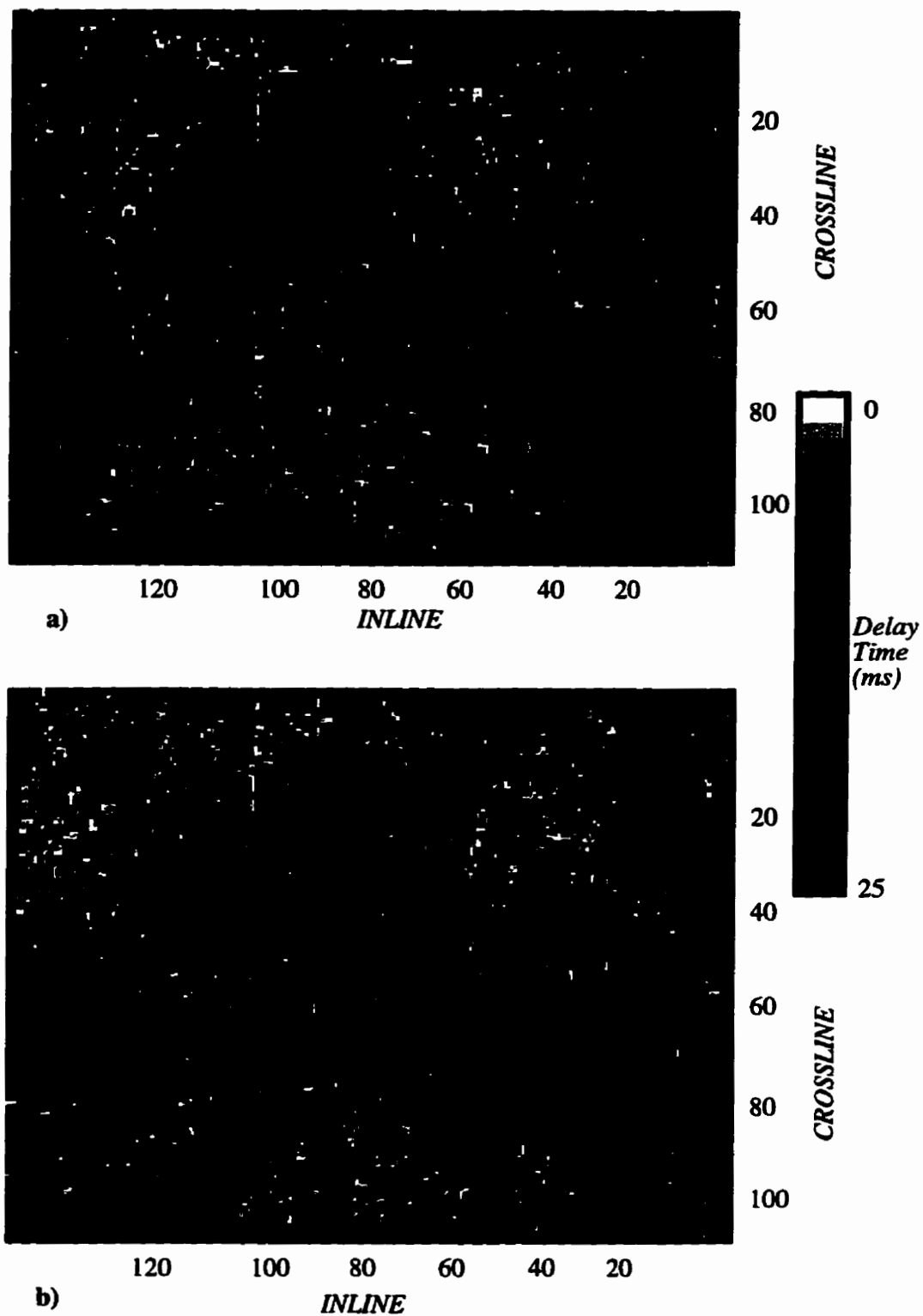


Figure 5.15: Time delay map between the S1 and S2 data volumes for the Second White Speckled Shale (a) and a peak one cycle below it (b).

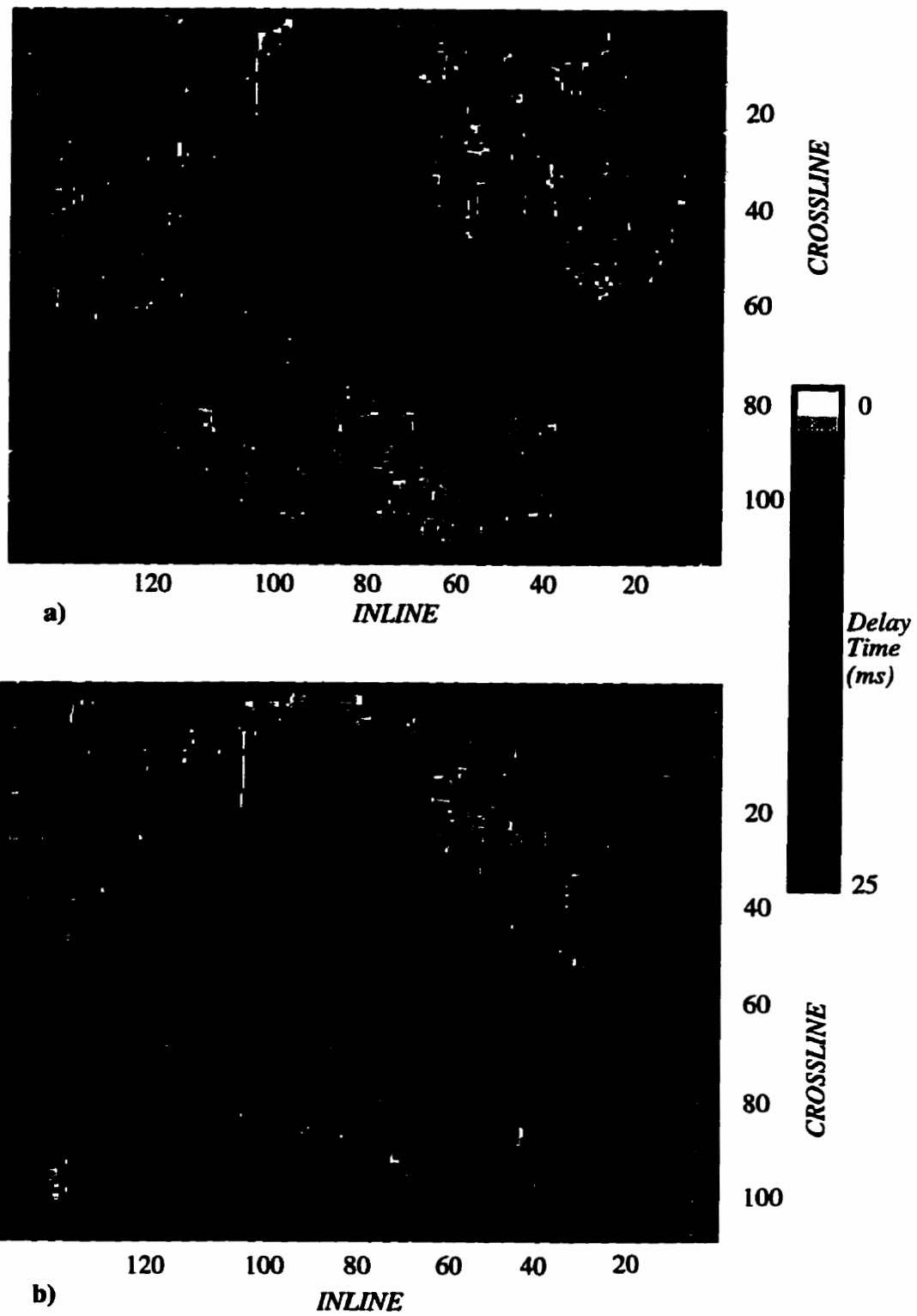
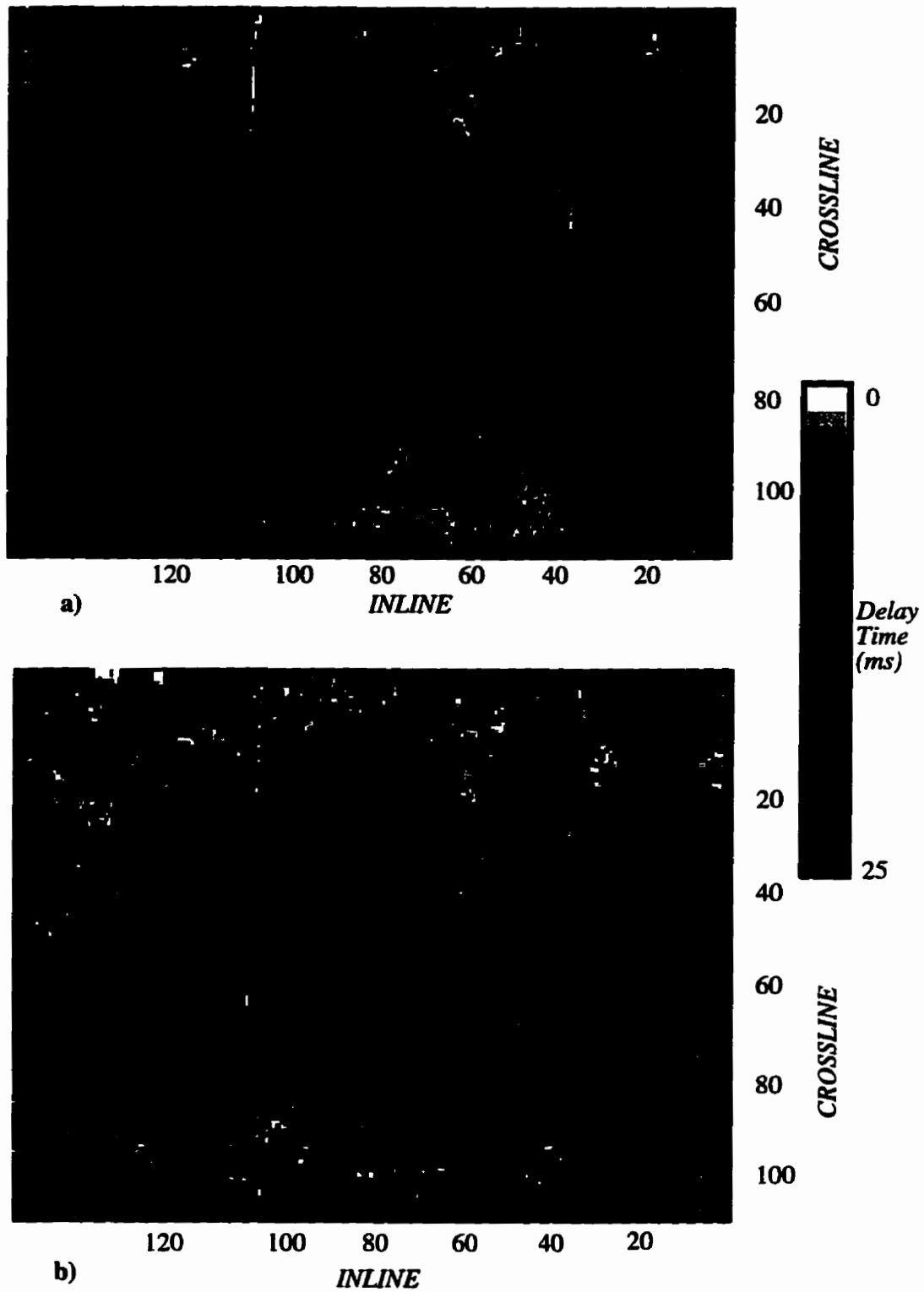
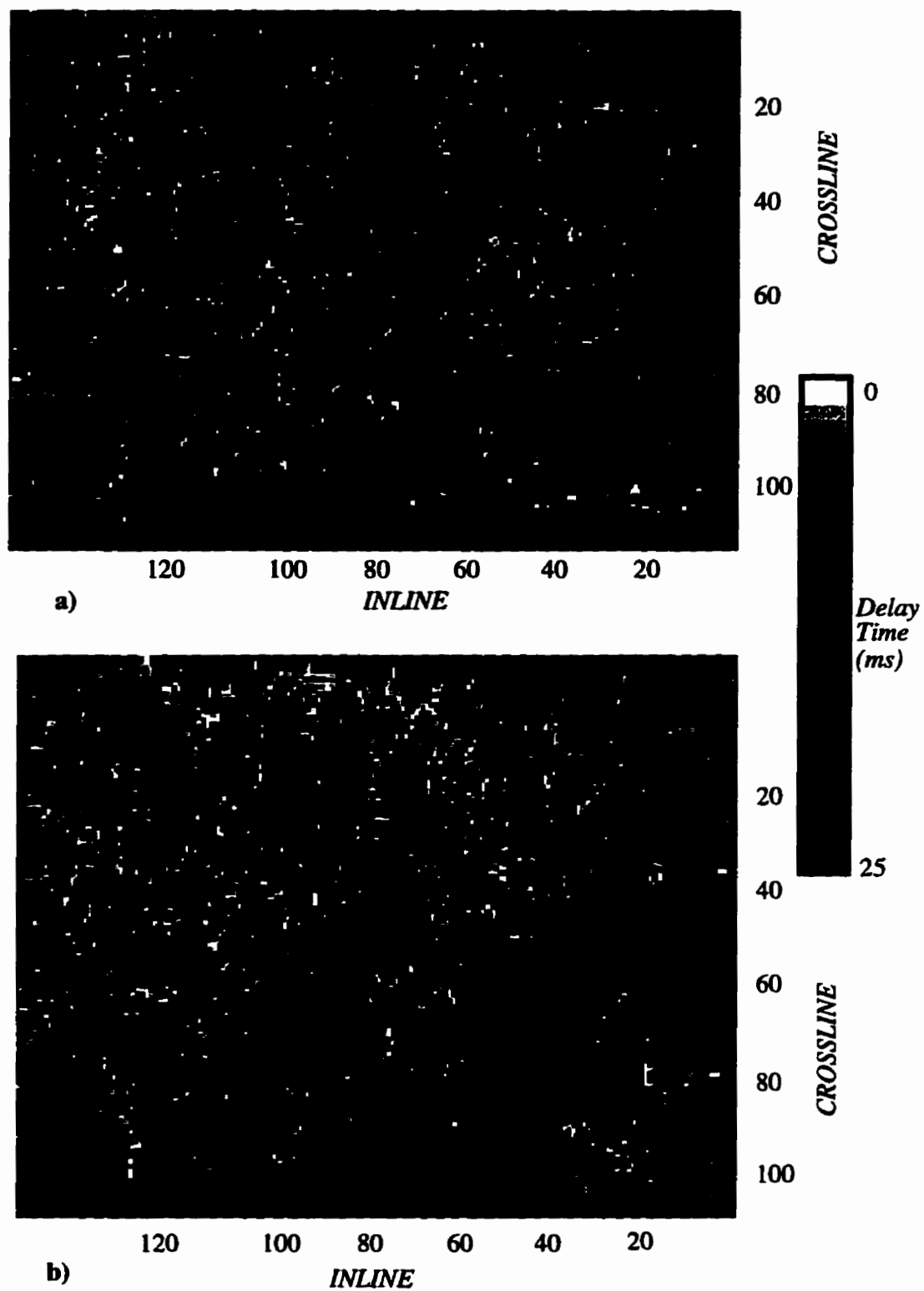


Figure 5.16: Time delay map between the S1 and S2 data volumes for the Base of Fish Scales (a) and the Viking (b).



**a)**  
**b)**

**Figure 5.17:** Time delay map between the S1 and S2 data volumes for the Mannville Coal (a) and the Wabamun (b).



**a)**  
**b)**  
Figure 5.18 : Time delay maps between the S1 and S2 data volumes for the Nisku (a) and the Leduc (b).

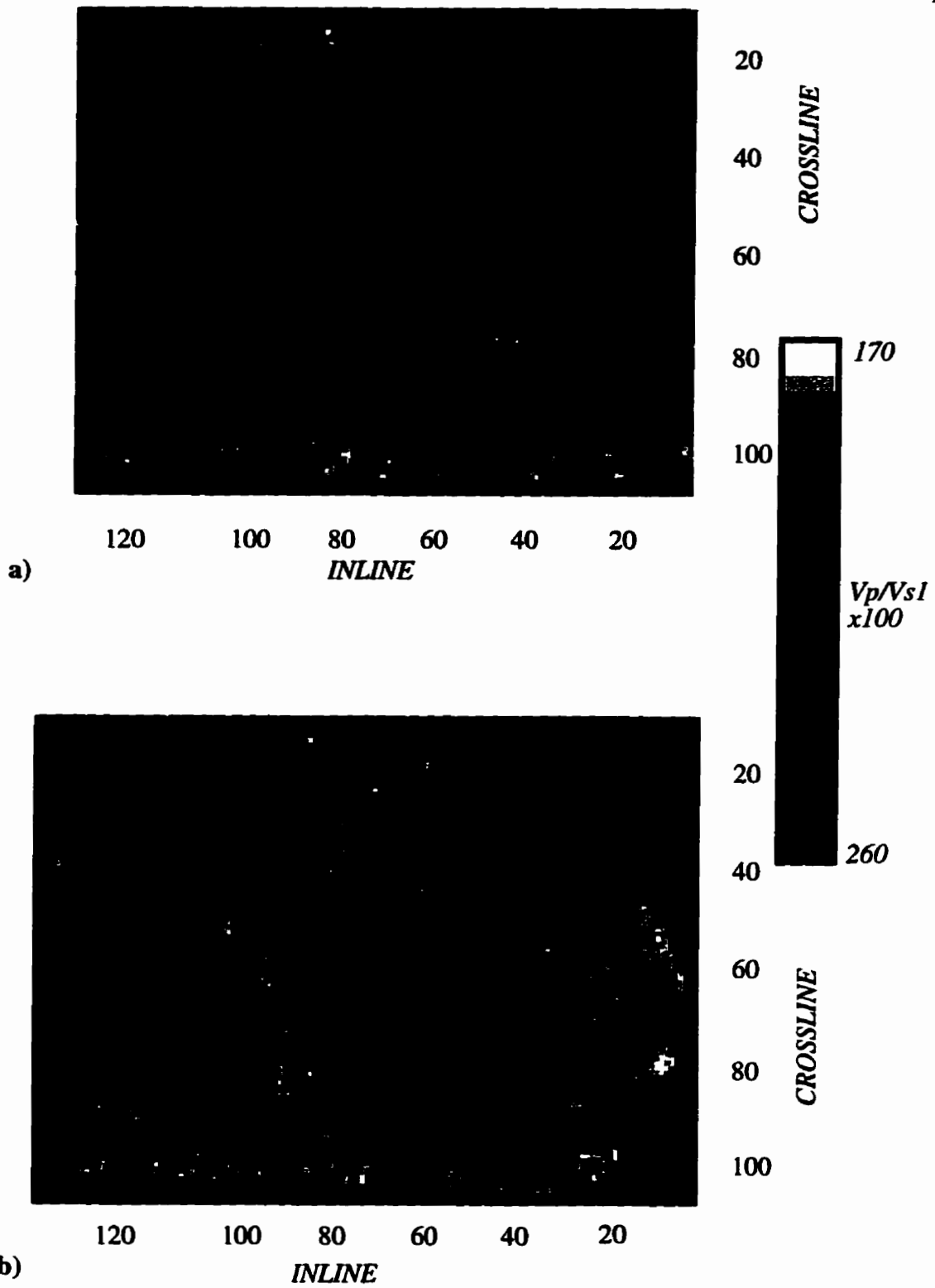


Figure 5.19:  $V_p/V_s1$  ratio ( $\times 100$ ) maps of the Viking calculated between two intervals: a) The Base of Fish Scales to the Mannville and b) Colorado event 1 and the Mannville.

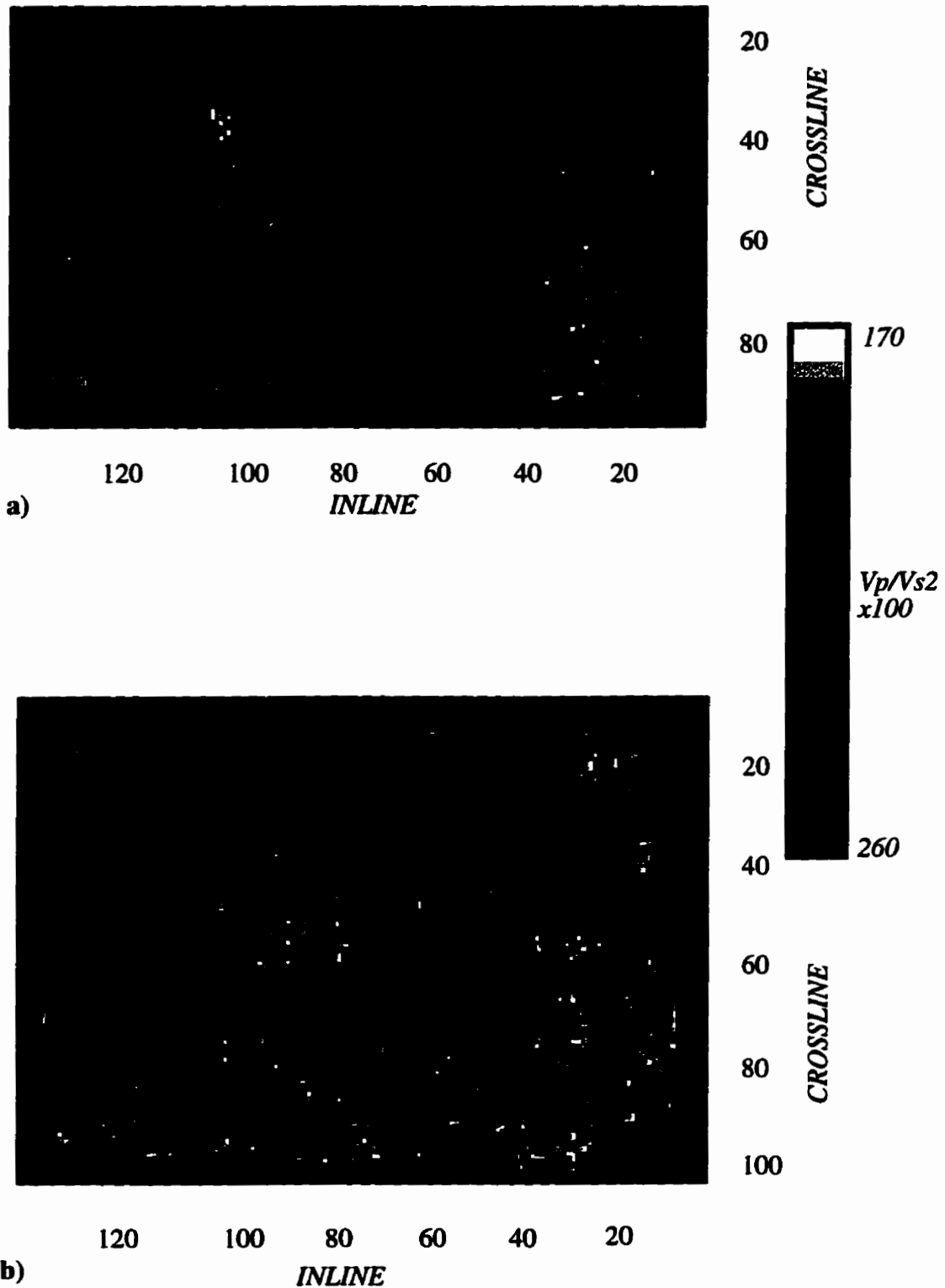


Figure 5.20:  $Vp/Vs2$  ratio ( $\times 100$ ) maps of the Viking calculated between two intervals: a) The Base of Fish Scales to the Mannville and b) Colorado event 1 and the Mannville.

## **5.6 3C-3D Interpretation flow**

Including “3-C” attributes in the 3-D realm adds a new complexity to the acquisition, processing, and interpretation of these data. Figure 5.21 summarizes the interpretation steps. The interpreter will be faced with up to 3 times the amount of data that he/she is accustomed to. Each volume of data will be correlated separately, using VSP or synthetic seismogram information. The analysis will also be done independently of each other. At this stage, a single P-P, or “conventional”, 3-D interpretation ends. With the additional elastic volumes, a third step is included. The data are integrated together to generate additional interpretive products that otherwise could not be created. This additional information will provide a more detailed and compelling interpretation of the subsurface.

The key to a successful interpretation is the proper field design that allows the interpreter uncompromised data to work with. This flow should be combined with the processing and acquisition flows of Figures 3.13 and 2.10, respectively to highlight that the interpretive processes begin in the acquisition. These flows should form a continuum: All three should be combined to ensure a detailed interpretation of the subsurface is successfully completed and done in a cost-effective manner.

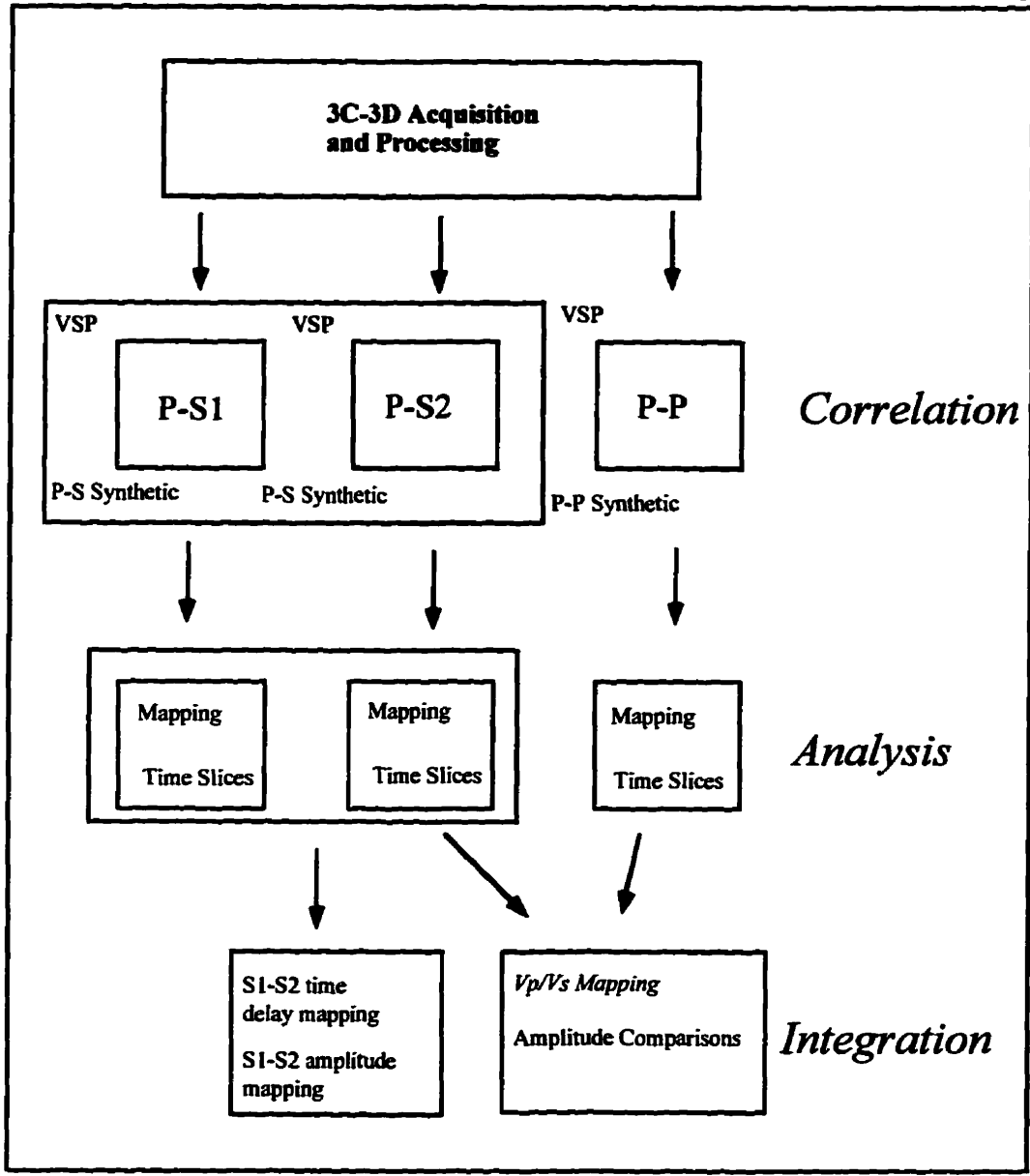


Figure 5.21: 3C-3D Interpretation flow.

## **5.7 Chapter Summary**

**Multicomponent converted-wave 3-D data provide additional elastic wave information to conventional P-wave data. This allows the construction of a more integrated interpretation that includes acoustic and elastic information in three dimensions.**

**Common conversion point (CCP) fold maps must be included as a criteria in future multicomponent 3-D acquisition designs. The CCP fold in the Joffre survey compromised the converted-shear amplitudes.**

**The P-S1 and P-S2 data volumes nonetheless are still of good data quality and have imaged all reflectors to the Precambrian basement. This has allowed the correlation of key horizons between the acoustic and the converted-wave data volumes in the construction of Vp/Vs maps.**

**Lateral variations in Vp/Vs have been mapped in the Viking formation which can be attributed to lateral sand presence. Possible lateral variations in the stress field have been mapped using delay-time measurements between S1 and S2.**

**Lateral Vp/Vs estimates from correlations of P, S1, and S2 volumes provide a powerful lithologic information not otherwise found in a conventional P-wave section.**

## **Chapter 6: Discussion and Conclusions**

The key advantage of P-S acquisition - the simultaneous recording of P-P and P-S data with one compressional source - can become a detriment if proper design schemes are not implemented. It is crucial, for future 3C-3D surveys, that CCP fold patterns be included in 3-D design. Otherwise, a severe acquisition "footprint" can mitigate the usefulness of the P-S data and remove the reason for acquiring the shear data in the first place. Lawton (1993) provides guidelines to optimize the CCP fold distribution within the framework of 3C-3D survey without compromising the P-P or the P-S data. These guidelines were further modified in Lawton et al. (1995) for the successful acquisition of the Blackfoot 3C-3D survey. Including CCP fold considerations in a 3D-3C survey design will ease the processing of the data and will provide a more detailed and compelling interpretation of the subsurface.

The amplitudes of the shear volumes in Chapter 5 could be made more consistent and usable via improvements in the survey design. The acquisition footprint has seriously compromised the S1 and S2 amplitudes and prevented them from being included in the interpretation. Mueller (1991) has shown amplitude changes in the S2 (the polarization perpendicular to the cracks) are more sensitive to fracture-induced anisotropy than are time intervals. The 3C-3D at Joffre would have had more impact if the S1 and S2 amplitudes were not compromised. Despite this limitation, the data provided useable and additional interpretation information.

In the field, a high channel demand will be imposed by the 3-component geophones. Logistically, the geophones will have to be laid-out and balanced with additional care. This will result in longer field time, and subsequently, higher costs.

Currently, the CREWES Project is involved in designing a geophone that is self-uprighting. This development should reduce geophone lay-out time in the field. The increased acquisition costs for 3C-3D are mitigated, however, by the added return of acquiring 3 independent datasets with a conventional compressional source. Survey design is currently somewhat compromised by a limited availability of 3-component geophones, which results in smaller live receiver templates and narrower azimuths. As interest in 3C-3D continues, the market will respond to this demand, a more 3-C geophones will become available to allow more flexibility in acquisition design.

Tuning effects, as seen in Chapter 4, can affect the absolute value of the  $V_p/V_s$  calculation, however, the relative ratio should remain consistent if the wavelet is stationary throughout the data. More detailed processing of the numerical data, such as applying the Slotboom NMO correction could have been attempted and should be done in the future. The depth of target allowed the use of the less robust, but adequate, lower-term NMO correction.

The wealth of data a 3C-3D surveys presents allow the interpretation of patterns of elastic and acoustic properties in plan view. The survey acquired over the numerical isotropic model in Chapter 4 clearly displays the clastic pods and the carbonate reef edge. It supplies additional information could not otherwise be determined exclusively from P-P data. It provided a second, independent assessment of the subsurface. The P-S data complemented the P-P data.

In Chapter 5, zones of high time delay may indicate areas of greater horizontal stress in the subsurface within the natural coordinate frame. Other effects, such as near-surface anisotropy variations may also be the cause for the time delay variations. The 45-degree S1 polarization angle, as determined in processing, compares favourably with the results of Babcock (1978) who measured well bore ellipticity in the Alberta basin. For brittle formations, such as the Second White Speckled Shale, it is possible that vertical

fractures, induced by lateral stress from the deformation front to the west, may preferentially occur in this formation. Detection for vertical fractures have been documented by Kendall and Kendall (1996), for example, in Wyoming.

The S1-S2 polarization axis was determined in processing by analyzing a data window centered about the dominant Mesozoic reflections (Peter Cary, personal communication). This average was then applied to the rest of the data. A more detailed layer-stripping approach may be acquired to detect any depth variation in the natural polarization axis. The delay time maps possibly introduce a new complexity in the characterization of stress within the sedimentary column. Reservoir modeling and development may benefit from this application. Patterns, such as delay time, can be biased by the survey acquisition. It is the responsibility of the interpreter in dealing with these sophisticated datasets to be aware of the possible acquisition and processing artifacts that can bias the interpreter.

In Chapter 5, the  $V_p/V_s$  values (between 1.7 and 2.6) mapped in the Viking for the S1 and S2 are within the agrees for sand and shale found in core data (Miller, 1992) and from seismic data (Tatham and Krug, 1985). The  $V_p/V_s$  anomaly could become more obvious if the sands were charged with gas (Tatham and McCormack, 1991).

In a historical context, 3D-3C is developing much like conventional 3-D was only a decade ago. As the economic aspects of the oil and gas industry become more dominant, we must provide more quantifiable criteria to our economic models. Converted-wave data can help mitigate the risk in a cost-effective manner. 3D-3C seismic techniques show promise in becoming an essential tool in risk reduction and investment optimization.

## References

- Al-Bastaki, A.R., Arestad, J.F., Bard, K., Mattocks, B., Rolla, M.R., Sarmiento, V., Windells, R., 1994, Progress report on the characterization of Nisku carbonate reservoirs: Joffre field, south-central Alberta, Canada, *in*: Reservoir characterization project - phase 5 report, Colorado School of Mines.
- Arestad, J.F., Mattocks, B.W., Davis, T.L., and Benson, R.D., 1995, 3-D, 3-C seismic characterization of the Nisku carbonate reservoir, Joffre field, south-central Alberta, CSEG Recorder.
- Alford, R.M., 1986, Shear data in the presence of azimuthal anisotropy: Dilley, Texas: 56th Ann. Internat. Mtg. Soc. Expl. Geophys., Expanded Abstracts, 476-479.
- Ata, E., Michelena, R.J., Gonzales, M., Cerquone, H., and Carry, M., 1994, Exploiting P-S converted-waves: Part 2, application to a fractured reservoir: 64th Ann. Internat. Mtg. Soc. Expl. Geophys., Expanded Abstracts, 240-243.
- Babcock, E.A., 1978, Measurement of subsurface fractures from dipmeters: AAPG Bulletin, 62, 7, 1111-1126.
- Berg, E., Svenning, B., Martin, J., 1994, SUMIC: Multicomponent sea-bottom seismic surveying in the North Sea - data interpretation and applications: 64th Ann. Internat. Mtg. Soc. Expl. Geophys., Expanded Abstracts, 477-480.
- Brown, A.R., 1991, Interpretation of three-dimensional seismic data: AAPG Memoir 42, American Association of Petroleum Geologists.
- Buchanan R., 1992, Three-dimensional seismic: The application of new technology to oil field development: Bull. Amer. Assoc. Petrol. Geol., 76, 1855-56.
- Cary, P.W. and Eaton, D.W.S., 1993, A simple method for resolving large converted-wave (P-SV) statics: Geophysics, 58, 429-433.
- Cary, P.W., 1994a, 3D converted-wave processing, Joffre survey, *in*: 3D-3C seismic exploration, CREWES Project tutorial notes.
- Cary, P.W., 1994b, 3-D converted-wave seismic processing: CREWES Research Report, 6, 31-1 - 31-10.
- Castle, R.J., 1988, Shifted hyperbolas and normal moveout: 58th Ann. Internat. Mtg., Soc. Expl. Geophys., Expanded Abstracts, 894-896.
- Colorado School of Mines, 1992, Reservoir characterization project phase 4 report, Colorado School of Mines.
- Cooper, N.M., 1993, 3D seismic acquisition, design, and quality control: Course

Notes, Mustagh Resources.

- Crews, G.A., Henderson, G.J., Musser, J.A., Bremner, D.L., 1989, Applications of new recording systems to 3-D survey designs: 59th Ann. Internat. Mtg. Soc. Expl. Geophys., Expanded Abstracts, 160-161.
- Deregowski, S.M., 1982, Dip moveout and reflector point dispersal, *Geoph. Prospecting*, 30, 318-322.
- Dickenson, J.A., Fagin, S.W., Weisser, G.H., 1990, Comparison of 3-D acquisition techniques on land: 60th Ann. Internat. Mtg. Soc. Expl. Geophys., Expanded Abstracts, 913-916.
- DiSiena, J.P., Gaiser, J.E., and Corrigan, D., 1984, Horizontal component and shear wave analysis of three component VSP data, in: Toksoz, N.M., and Stewart, R.R., eds., Vertical seismic profiling, Part B: Advanced concepts, Geophysical Press.
- Eaton, D.W.S. and Stewart, R.R., 1989, Aspects of seismic imaging using P-SV converted-waves: CREWES Research Report, 1, 68-92.
- Eaton, D.W.S., Slotboom, R.T., Stewart, R.R., and Lawton, D.C., 1990, Depth variant converted wave stacking: 60th Ann. Internat. Mtg., Soc. Expl. Geophys., Expanded Abstracts, 1107-1110.
- Eaton, D.W.S., Stewart, R.R., and Harrison, M.P., 1991, The Fresnel zone for P-SV waves, *Geophysics*, 56, 360-364.
- Eaton, D.W.S. and Lawton, D.C., 1992, P-SV stacking charts and binning periodicity: *Geophysics*, 57, 745-748.
- Ensley, R.A., 1985, Evaluation of direct hydrocarbon indicators through comparison of P- and S-wave data: A case study of the Myrnam Gas Field, Alberta: *Geophysics*, 50, 37-48.
- French, W.S., 1974, Two-dimensional and three-dimensional migration of model experiment reflection profiles: *Geophysics*, 39, 265-277.
- Fromm, G., Krey, T., and Wiest, B., 1985, Static and dynamic corrections, *in* Seismic shear waves: Handbook of geophysical exploration, 15a, 191-225, Geophysical Press.
- Galbraith, M., 1994, 3-D survey design by computer: Course Notes, Seismic Image Software Ltd.
- Gallant, E.V., Stewart, R.R., and Bertram, M.B., 1996, Development of an auto-orienting geophone: CREWES Project Report, 8, 2-1, 2-2.

- Garotta, R., Marechal, P., and Magesan, M., 1985, Two component acquisition as a routine procedure for recording P-waves and converted waves: *Jour. Can. Soc. Explor. Geophys.*, 20, 440-54.
- Garrota, R. and Granger, P.Y., 1988, Acquisition and processing of 3C X 3D data using converted waves: 58th Ann. Internat. Mtg., Soc. Expl. Geophys., Expanded Abstracts, 995-997.
- Garrota, R., Vuillermoz, C., and Granger, P.Y., 1990, Comparing 3-D operations and results from converted P-S waves: 60th Ann. Internat. Mtg. Soc. Expl. Geophys., Expanded Abstracts, 1086-1088.
- Goodaway, W.N. and Mayo, L.F., 1994, Multicomponent seismic and borehole experiment to establish and identify the cause of anisotropy in the 2nd white specks at Garrington, Alberta: 64th Ann. Internat. Mtg. Soc. Expl. Geophys., Expanded Abstracts, 248-251.
- Harrison, M.P., 1992, Processing of P-SV surface-seismic data: anisotropy analysis, dip moveout, and migration: Unpublished PhD. dissertation, The University of Calgary.
- Harrison, M., and Stewart, R.R., 1993, Poststack migration of P-SV seismic data: *Geophysics*, 58, 1127-1135.
- Hale, D., 1984, Dip-moveout by Fourier transformations: *Geophysics*, 49, 741-757.
- Isaac, J.H., 1996, Seismic methods for heavy oil reservoir monitoring: Unpublished PhD. dissertation, The University of Calgary.
- Kendall, R.R. and Kendall, J.M., 1996, Shear-wave amplitude anomalies in South-central Wyoming, *The Leading Edge*, 15, 913-920.
- Lane, M.C., and Lawton, D.C., 1993, 3-D converted-wave asymptotic binning: CREWES Research Report, 5, 29-1 - 29-5.
- Lane, M.C., and Lawton, D.C., 1993, 3-D converted-wave asymptotic binning: CREWES Research Report, 5, 29-1 - 29-5.
- Lane, M.C., 1994, An implementation of 3-D seismic binning: CREWES Research Report, 6, 24-1, 24-5.
- Lansley, M., 1994, 3-D seismic design: SEG course notes. Society of Exploration Geophysicists.
- Larson, G.A. and Stewart, R.R., 1994, Analysis of 3-D P-S seismic data: Joffre, Alberta: CREWES Research Report, 6, 32-1 - 32-33.
- Larson, G.A. and Stewart, R.R., 1995 Interpretation techniques for 3C/3D seismic

- data: 65th Ann. Internat. Mtg. Soc. Expl. Geophys., Expanded Abstracts, 286-288.
- Lawton, D.C., 1993, Optimum bin size for converted-wave 3-D asymptotic mapping: CREWES Research Report, 5, 28-1 -28-14.
- Lawton, D.C., 1994, Acquisition design of 3-D converted-waves: CREWES Research Report, 6, 23-1 - 23-23.
- Lawton, D.C., Stewart, R.R., Cordsen, A., and Hrycak, S., 1995, Advances in 3C-3D design for converted waves: CREWES Research Report, 7, 43-1 - 43-41.
- Leckie, D.A., Bhattacharya, J.P., Bloch, J., Gilboy, C.F., Norris, B, 1994. Cretaceous Colorado/Alberta group. In: Geological Atlas of the Western Canada Sedimentary Basin. G.D. Mossop and I. Shetson (comps.). Calgary, Canadian Society of Petroleum Geologists and Alberta Research Council, chpt. 20.
- Lynn, H.B. and Thomsen, L.A., 1986, Reflection shear-wave data along the principal of axes of azimuthal anisotropy: 56th Ann. Internat. Mtg. Soc. Expl. Geophys., Expanded Abstracts, 473-476.
- Miller, S.L.M., 1992, Well log analysis of Vp and Vs in carbonates: CREWES Research Report, 4, 12-1 - 12-11.
- Miller, S.L.M, Harrison, M.P., Lawton, D.C., Stewart, R.R., and Szata, K.J., 1994, Analysis of P-P and P-SV seismic data from Lousana, Alberta: CREWES Research Report, 6, 7-1 - 7-24.
- Mueller, M.C., 1991, Prediction of lateral variability in fracture intensity using multicomponent shear-wave surface seismic as a precursor to horizontal drilling in the Austin Chalk: Geophys. J. Int. 107, 409-415.
- Musser, J.A., Bremner, D.L., Crews, G.A., and Henderson, G.J., 1989, Application of new seismic technology to land 3-D surveys: implementation: 59th Ann. Internat. Mtg. Soc. Expl. Geophys., Expanded Abstracts, 628-631.
- Nazar, B.D., 1991, An interpretive study of multicomponent seismic data from the Carrot Creek area of west-central Alberta: M.Sc. thesis, The University of Calgary.
- O'Connell, , J.K., Kohli, M., and Amos, S. 1993, Bullwinkle: A unique 3D experiment: Geophysics, 49, 493-508.
- Oosterbaan, J.M., 1990, 3-D seismic as an exploration tool: 60th Ann. Mtg. Soc. Expl. Geophys., Expanded Abstracts, 160-161.

- Reinson, G.E., Warters, W.J., Cox, J., Price, P.R., 1994. Cretaceous Viking formation, *in*: Geological Atlas of the Western Canada Sedimentary Basin. G.D. Mossop and I. Shetson (comps.). Calgary, Canadian Society of Petroleum Geologists and Alberta Research Council, chpt. 21.
- Robertson, J.D., 1987, Carbonate porosity from S/P traveltimes ratios: *Geophysics*, 52, 1346-1354.
- Robertson, J.D., 1992, Reservoir management using 3-D data, *in*: Reservoir Geophysics: Sheriff, R.E., ed., Society of Exploration Geophysicists.
- Schaffer, A., 1993, Binning, static correction, and interpretation of P-SV surface-seismic data: M.Sc. thesis, The University of Calgary.
- Sheriff, R.E., and Geldart, L.P., 1982, Exploration Seismology, vol.1. Cambridge University Press.
- Sherrif, R.E., 1991, Dictionary of geophysical terms, SEG.
- Slotboom, R.T., Eaton, D.W.S., and Lawton, D.C., 1990 Improving converted-wave (P-S) moveout estimation, CREWES Research Report, 2, 80-88.
- Slotboom, R.T., 1990, Converted-wave (P-SV) moveout estimation: 60th Ann. Internat. Mtg. Soc. Expl. Geophys., Expanded Abstracts, 1104-1106.
- Stewart, R.R. and Lawton, D.C., 1994, 3C-3D seismic polarity definitions, CREWES Project 3C-3D seismic exploration, Course notes.
- Stewart, R.R., Pye, G., Cary, P.W., and Miller, S.L.M., 1993, Interpretation of P-S seismic data: Willesden Green, Alberta: CREWES Research Report, 5, 15-1 - 15-19.
- Stone, D., 1994, Designing seismic surveys in two and three dimensions: SEG investigations in geophysics, 5. Society of Exploration Geophysicists.
- Sun, Z., and Stewart, R.R., 1994, 3-D reverse VSP: CREWES Research Report, 6, 12-1 - 12-21.
- Taner, M.T. and Koehler, F., 1969, Velocity spectra - digital computer derivation and applications of velocity functions: *Geophysics*, 34, 859-881.
- Tatham, R.H. and Goolsbee, D.V., 1984, Separation of S-wave and P-wave reflections offshore western Florida: *geophysics*, 49, 493-508.
- Tatham, R.H. and Krug, E.H., 1985, Vp/Vs interpretation, *in*: A.A. Fitch, Ed., Developments in geophysics-6: Elsevier Appl. Sci. Publ, 139-188.
- Tatham, R.H. and McCormack, M.D., 1991, Multicomponent seismology in petroleum exploration: Investigations in geophysics - 6, Society of Exploration

**Geophysicists.**

- Tatham, R.H., and Stewart, R.R., 1993, Present status and future directions of shear-wave seismology in exploration: CREWES Research Report, 5, 1-1 - 1-21.
- Tessmer, G. and Behle, A., 1988, Common reflection point data-stacking technique for converted-waves: *Geophys. Prosp.*, 36, 671-688.
- Wang, S., Lane, M.C., and Lawton, D.C., 1994, Fast 3-D converted-wave depth-variant common conversion point stacking: CREWES Research Report, 6, 25-1,- 25-11.
- Wang, S., Bancroft, J.C., and Lawton, D.C., 1994, DMO processing for mode-converted waves in a medium with a linear increase in velocity with depth: CREWES Research Report, 6, 26-1 - 26-15.
- Wiggins, R.A., Lerner, K.L., and Wisecup, R.D., 1976, Residual statics analysis as a general linear inverse problem: *Geophysics*, 41, 922-938.
- Winterstein, D.F., and Meadows, M.A., 1991, Changes in shear-wave polarization azimuth with depth in Cymric and Railroad Gap oil fields: *Geophysics*, 56, 1349-1364.
- Yardley, G.S., Graham, G., and Crampin, S., 1991, Viability of shear-wave amplitude versus offset studies in anisotropic media: *Geophys. J. Int.*, 105, 493-503.
- Yang, G.Y.C., Lawton, D.C., Stewart, R.R., Miller, S.L.M., Potter C.C., and Simin, V., 1996, Interpretation and analysis of the Blackfoot 3C-3D seismic survey, CREWES Research Report, 8, 46-1 - 46-41.
- Yilmaz, O., 1989, Seismic data processing, SEG Investigations in geophysics, vol.2., SEG publications.
- Zheng, Y. and Stewart, R.R., 1993, Directional filtering and side-swipe imaging: CREWES Research Report, 5, 12-1 - 12-21.